THEORETICAL SIMULATIONS OF NANOCONFINED WATER

Jon Zubeltzu Sesé

PhD Thesis

Supervisor: Emilio Artacho Cortés

2017

Laburpena

Ezagutza ezberdinetako pertsona askori galdetuko balitzaie zein iruditzen zaien gizadiarentzat dagoen sustantziarik garrantzitsuena, ziurrenik, ura dela esango lukete gehienek. Ura, bizitza sortzeko oinarri eta hainbat giza jardueretan izugarrizko garrantzia izateaz gainera, zientziaren historiako protagonistetako bat izan da. Gaur egun, badakigu uraren oinarrizko unitatea bi hidrogeno-atomoz eta oxigeno-atomo batez osatutako molekula dela. *A priori* sinplea dirudien arren, urari ohikoak ez diren 70 propietate baino gehiago aurkitu zaizkio, anomaliak deiturikoak, eta horien jatorria ezezaguna da zientzialarientzat. Nahiz eta historian zehar hainbat eredu proposatu diren uraren anomaliak azaldu ahal izateko, eredu horien baliotasuna oraindik ere frogatu beharreko zeregina da.

Azken urteotan, espazio txikitan konfinatuta dagoen urak arreta berezia hartu du komunitate zientifikoan bi arrazoi nagusigatik. Alde batetik, espazio txikitan harrapatutako ura diziplina zientifiko ugaritako sistema garrantzitsuetan azaltzen da. Biologian adibidez, gaur egun dagoen zeregin nagusienetako bat zelula bizi baten barnean dagoen uraren egitura ezagutzea da. Zelularen ingurunea zitoplasmak osatzen du eta bertan dauden molekula biologiko askoren arteko distantziak nanometrokoak dira. Jakina da, espazio txiki hauetan dagoen uraren egiturak molekula hauen funtzionamendua determinatzen duela, nahiz eta egitura hau ezezaguna den oraindik. Geologian, mineral askoren poroetan dagoen uraren egiturak eta dinamikak bortizki determinatzen dituzte mineral horren ezaugarriak. Nanoteknologian ere, espazio txikitan topatutako uraren presentzia kontutan hartu beharreko faktorea da sarritan. Bestetik, jakina da uraren jokaera izugarri aldatzen dela espazio txikitan konfinatuta dagoenean. Eta beraz, egoera honetan dagoen uraren ikerketak, anomalien jatorriaren bilaketan perspektiba alternatiboa ematen du.

Gaur egun ere, zaila da esperimentalki ur konfinatua ikertzea: ura espazio txik-

itan sartzea eta bertatik datorren informazio kopuru txikia aztertzea oztopo handiak dira. Hala eta guztiz ere, badira ikerketa esperimental batzuk, ura grafeno geruzen artean edota karbonozko nano-hoditan sartuta, emaitza interesgarriak lortu dituztenak. Azken urteotako ur konfinatuari buruzko ikerketa gehienak simulazio konputazionalen bidez egin dira, aurretik aipatutako bi oztopo nagusiak errez gainditzen baitira. Simulazioetan, partikulen posizio eta abiadurak modu zehatzean ezartzen dira, eta beraz, ura espazio txikitan sartzea erraza da. Horrez gain, urak soilik emandako informazioa hautatzea lan samurra da. Modu honetan ikerketa-lan ugaritan ezohikoak diren ezaugarriak topatu dira: egitura kristalografiko ezberdin ugari, fase trantsizio arraroak, substratu konfinantearen izaeraren araberako urtze tenperaturaren eta erantzun-funtzioen aldaketa, etab.

Jokaera ezohiko hauen jatorrietako bat konfinamendu soila da: material baten tamaina, dimentsioren batean, nanometro ingurukoa denean, bere izaera intrintsekoa aldatzen da. Uraren simulazioetan aldaketa mota hauek aztertzeko, parametro gutxi dituzten potentzial konfinante sinpleak erabili ohi dira, hautatutako substratu konfinantearen berezitasunek sor ditzaketen efektuak ekiditeko. Hala ere, konfinamenduaren efektuak beraien osotasunean ulertu nahi badira, substratu konfinantearen influentzia kontutan edukitzea garrantzitsua da. Azken urteotako emaitzek gainazalen geometriak, topografiak eta heterogeneotasun kimikoak garrantzizko faktore direla erakutsi dute. Horrexegatik, konfinamenduak urean dituen efektu intrintseko eta estrintsekoen ikerketa eginkizun garrantzitsu bilakatu da.

Duela gutxi publikatutako ikerketa esperimental batean ikusi da ura grafeno artean sartzen denean, forma karratuko izotz geruzatan egituratzen dela. Simulazio konputazionalak ados daude ura dimentsio batean konfinatzen denean ur-geruzak sortzen direla, baina ikerketa gehienek ez dute egitura karratuko izotza aurreikusten. Dinamika molekularrez baliatutako simulazio berri batean, dentsitate altuetan bi geruzatan egituratutako ura, ezohiko fase trantsizio jarraitu baten bitartez izotz erronbiko bilakatzen dela ikusi da. Beste zientzialari batzuek aldiz, pareko baldintzetan bi-geruzatako izotz amorfo baten eraketa deskribatzen dute. Corsetti *et al.*-k publikatutako ikerlan batean berriz, entropia handiko izotz triangeluarra aurreikusten dute, non oxigeno atomoak sare triangeluar batean egituratuta baitauden, hidrogeno atomoak guztiz deslokalizatuta dauden bitartean. Aipatutako ikerketa lan hauek, ur konfinatuari buruzko interesaren eta gaur egungo eztabaidaren isla argiak dira.

Tesi honen helburu nagusia simulazio konputazionalen bitartez deskribatutako

ur bidimentsionalaren propietate ezohikoen ikerketa da. Ezaugarri ezohiko hauen bi jatorrien azterketan jartzen dugu arreta nagusia: konfinamendu soiletik datorren jatorri intrintsekoetan eta hautatutako substratu konfinanteak eragindako efektu estrinsekoetan. Simulazioak burutzeko, bi metodo erabiliko ditugu: Batetik, fisika klasikoan oinarritutako dinamika molekularraz baliatzen gara, non molekulen arteko interakzioa deskribatzeko TIP4P/2005 ur-eredu enpirikoa erabiltzen baitugun. Bestetik, fisika kuantikoko lehen-printzipioetan oinarritutako dentsitate funtzionalaren teoria erabiltzen dugu. Azken honetan, korrelazio-truke energia deskribatzeko vdW-DF$^{\mathrm{PBE}}$ funtzionalaz baliatzen gara. Hasiera batean, simulazioko partikula kopurua, tenperatura eta bolumena konstante mantentzen dira urak oreka termodinamikoa lortu arte. Behin oreka termodinamikoa lortzen denean, partikula kopuru, bolumen eta energia konstanteko simulazioak burutzen dira, honela partikulen ibilbide egokia lortzen baita.

Ur konfinatuaren joera intrintsekoak aztertzeko bi Lennard-Jones 9-3 potentzialen artean sartzen dugu, beraien arteko distantzia 8 Å-koa izanik, eta honela, ura bi geruzetan egituratzen dela bermatuz. Simulazioak hainbat dentsitate eta tenperaturatan burutzen dira, eta behin bukatzen direnean, lortutako datuen azterketa egiten dugu. Tenperatura-dentsitate fase diagraman ur likidoa eta hiru fase kristalino ikusten ditugu: ezti-orraze izotza, hodi-karratu izotza eta izotz triangeluarra. Ezti-orraze izotza tenperatura eta dentsitate baxutan da egonkorra. Oxigeno atomoak ezti-orrazean egituratzen dira, hidrogeno atomoek hidrogeno-lotura finkoak ezartzen dituzten bitartean. Izotz hau ohizko lehen mailako fase trantsizio batez urtzen da. Hodi-karratuko izotza tenperatura baxutan eta dentsitate altutan azaltzen da. Bertan, oxigeno atomoak hodi karratuetan egituratzen dira eta hidrogeno atomokoek hidrogeno-lotura finkoak ezartzen dituzte hodi bereko oxigenoen artean. Kasu honetan ere, lehen mailako fase trantsizioa gertatzen da izotza eta likidoaren artean.

Izotz triangeluarra fase diagramako tenperatura eta dentsitate altutan azaltzen da. Fase honek ezohikoak diren ezaugarriak erakusten ditu: oxigeno atomoak egitura triangeluarrean ezartzen diren arren, hidrogeno atomoak guztiz deslokalizatuta daude, likido batean bezala. Izotz honen eta hodi-karratuko izotzaren arteko fase trantsizioa lehen mailakoa da, eta bertan emandako energia truketik izotz triangeluarraren entropia konfigurazionala balioztatzen dugu. Aurreko ikerketa-lan baten estimazioarekin bat eginda, izotz arruntak duen entropia konfigurazional bikoitza duela kalkulatzen dugu.

Ur likidoaren eta izotz triangeluarraren arteko fase trantsizioa aztertzerakoan, modu jarraituan ematen dela ikusten dugu. Fase trantsizioa ematen den bitartean, ox-

igeno atomoak izoztuz doaz, hidrogeno atomoak likido modura jokatzen duten bitartean. Bestalde, izotz kristalinoaren eta likidoaren artean fase hexatiko bat topatzen dugu, bi dimentsiotako Kosterlitz-Thouless-Halperin-Nelson-Young fase trantsizio jarraituko teoria betez. Fase trantsizio honetatik hurbil dagoen likidoak izotz triangeluarraren ezaugarriak erakusten ditu: bi geruza nabarmeneko egitura, geruzen arteko korrelazio handia, egitura triangeluar lokala eta oxigeno atomoen eta hidrogeno atomoen dinamiken arteko banaketa. Beraz, fase diagramako zonalde batean ura fluido monoatomiko baten gisa jokatzen duela ikusten dugu.

Egiazko esperimentu batean ura konfinatzen duen substratuaren gainazalak izan ditzakeen efektu estrintsekoak aztertzeko potentzial ezberdin bat proposatzen dugu. Potentzial hau aurretik aipatutako Lennard-Jones 9-3 potentzialean oinarrituta dago baina ezberdintasun bat eransten diogu: gainazalean Lennard-Jones 12-6 partikulak modu periodikoan itsasten dizkiogu. Honela, topologia periodikoa duen potentzial biren artean konfinatzen dugu, modulazio honen distribuzioa eta anplitudea kontrolatzen ditugularik. Lennard-Jones 12-6 partikulak egitura triangeluarrean ezartzen ditugu, sare parametro ezberdinak erabiliz: lehenik, ezti-orraze izotzaren egonkortasunarentzat mesedegarria den batekin, eta azkenik, zenbait substratu errealek duten sare-parametrotik hurbil dauden hiru balio.

Lehen kasuan, ezti-orraze izotzaren urtze-tenperaturak gorakada nabarmena erakusten du modulazioaren anplitudea handitzen doan heinean. Hala eta guztiz ere, izoztu aurretiko likidoak egitura triangeluarra mantentzen du, nahiz eta kanpo-modulazioak egitura mota hau zapuzten duen. Kanpo-modulazioak lehen printzipioetatik lortutako likidoa eragiten du bereziki: modulazio anplitude txikitan ere, geruza nabarmenen eta AA metaketaren galera ikusten da. Modulazioaren anplitude kritiko batetik aurrera konfinamendu homogeneoan ikusitako fase hexatikoa galtzen da, eta beraz, likidoaren eta izotz triangeluarraren arteko fase trantsizio jarraitua ez-egonkor bilakatzen da. Fase hexatikoaren ordez, hiru geruzaz osaturiko fase kristalino berria azaltzen da. Sare-parametro errealisten kasuan, nahiz eta likidoak izozteko erraztasun handiagorik ez duen erakusten, jokaera ez-homogeneo garbia du modulazioaren anplitudea handitzen doan heinean.

Ura ikertzeko erabili diren bi metodo independenteen arteko adostasun garbia tesi honetako ondorio garrantzitsuetako bat da. Nahiz eta lehen printzipioetan oinarritutako likidoak egitura triangeluarragoa izateko joera duen, emaitza oso antzekoak ematen dituzte bi metodoek. Ondorio honek bi metodoen baliotasuna nabarmentzen du.

Tesiko azkeneko atalean transmisiozko mikroskopio elektronikoak grafenoko bi geruzatan duen efektua aztertzen dugu. Ura nanometro tamainara konfinatzeko hautagai nagusienetakoa denez grafenoa, lehenik lehorra dagoenean aztertzen dugu aurretiko pauso modura. Esperimentuan, mikroskopiotik datozen elektroien energia baxua denean, bi grafeno geruzetan defektu egonkor bat eratzen dela ikusten dugu: tximeleta defektua. Harrigarria dena da geruza bakarreko grafenoan esperimentua errepikatuz, ez dela inongo defekturik eratzen. Dentsitate funtzionalaren teorian oinarritutako lehen printzipioko kalkuluak eginez efektu honen bi kausa posible ikertzen ditugu: grafenoko bigarren geruzak defektuaren egonkortasunaren handitzea eta defektuaren eraketa prozesuan efektu katalitikoa eragitea. Lehen kasuan, defektuaren eraketa-energiaren kalkuluak geruza bakarreko eta biko grafenoaren egonkortasunean aldaketarik ez dagoela erakusten du. Bigarren kausa aztertzerakoan, lehen printzipioetako dinamika molekularrek bi geruzako grafenoan karbono atomo bat kanporatzeko behar den energia, geruza bakarreko grafenoan kanporatzeko behar denaren berdina dela frogatzen dute. Hala eta guztiz ere, tximeleta defektua sortzeko lagungarri diren bitarteko egoera katalitikoen existentzia ikusten dugu, eta beraz, energia baxutan bitarteko egoera katalitikoen bitartez sorturiko defektuak sor daitezkeela frogatzen dugu.

Abstract

Liquid water is not only of obvious importance but also extremely intriguing, displaying many anomalies that still challenge our understanding of such an a priori simple system. The same is true when looking at nanoconfined water: The liquid between constituents in a cell is confined to such dimensions, and there is already evidence that such water can behave very differently from its bulk counterpart. The aim of this thesis is to study the properties of two-dimensionally confined water by computer simulations. We do it by means of molecular dynamics simulations using both empirical potentials and first-principles calculations at different temperatures and densities.

In the first part of the work, we study the intrinsic properties exhibited by nanoconfined bilayer water under a planar confinement. The obtained phase diagram shows a stable bilayer liquid region and three other regions where different bilayer crystalline ices are found: the honeycomb, the square-tubes and triangular ices. At high densities and temperatures, a continuous phase transition, similar to a previously reported one, is observed between the triangular ice and the liquid. We observe the continuous melting to be related to the phase change of the oxygens only, with the hydrogens remaining liquid-like throughout. Moreover, we find an intermediate hexatic phase for the oxygens between the liquid and a triangular solid ice phase, following the Kosterlitz-Thouless- Halperin-Nelson-Young theory for two-dimensional melting. The liquid itself tends to maintain the local structure of the triangular ice, with its two layers being strongly correlated, yet with very slow exchange of matter. The decoupling in the behavior of the oxygens and hydrogens gives rise to a regime in which the complexity of water seems to disappear, resulting in what resembles a simple monoatomic liquid.

In the second part of the work, we study the response of water to the imposition of a periodicity in the confinement. For that we propose a periodic confining potential emulating the atomistic oscillation of the confining walls, that allows varying the lattice

parameter and amplitude of the oscillation. We do it for a triangular lattice, with several values of the lattice parameter: one which is ideal for commensuration with layers of Ih ice, and other values that would correspond to more realistic substrates. For the former, the phase diagram shows an overall rise of the melting temperature. However, the liquid maintains a bi-layer triangular structure despite the fact that it is not favoured by the external periodicity. The first-principles liquid is significantly affected by the modulation in its layering and AA stacking even at relatively small amplitudes. Beyond some critical modulation amplitude the hexatic phase present in flat confinement is replaced by a trilayer crystalline phase unlike any of the phases encountered for flat confinement. For more realistic lattice parameters, the liquid does not display higher tendency to freeze, but it clearly shows inhomogeneous behaviour as the strength of the rugosity increases.

The comparison between the results obtained from *ab inito* molecular dynamics with the vdW-DF$^{\mathrm{PBE}}$ functional and classical molecular dynamics with the TIP4P/2005 empirical force-field gives a good agreement. Given the large difference between both calculations methods, this conclusion supports the validity of both calculations methods for describing water.

Aita ta Amari

Contents

1 Introduction **1**

1.1 Water, a current mystery 1

1.2 Confined water 3

1.2.1 Thermodynamics 4

1.2.2 State-of-the-art 6

1.3 This thesis 11

2 Methods **17**

2.1 Dynamics 17

2.1.1 Ensembles and thermostats 17

2.1.2 Time-integrators 20

2.1.3 Atomic interaction 21

2.2 Confining potential 24

2.2.1 Planar potential 24

2.2.2 Rugous potential 25

2.3 Data analysis 27

2.3.1 RDF 27

2.3.2 Density Profile 28

2.3.3 Mean Square Displacement 28
2.3.4 Dipole-dipole autocorrelation function 29
2.3.5 First-neighbor correlation function 30

3 Planar confinement: ices **35**

3.1 Ices 37
3.2 Phase transition 40

4 Planar confinement: liquid **45**

4.1 Phase transitions 45
4.2 Characterization of liquid 51

5 Rugous confinement **59**

5.1 Ideal commensuration 60
5.1.1 Phase diagram 61
5.1.2 Hexatic phase 62
5.1.3 Intercalated honeycomb ice 65
5.1.4 Liquid 65
5.2 Realistic lattice parameters 70
5.2.1 Structure 70
5.2.2 Diffusivity 73

6 Graphene **77**

6.1 Introduction 77
6.2 Methods 79
6.2.1 Experimental methods 79
6.2.2 Theoretical methods 80

6.3 Results 86

6.3.1 Experimental results 86

6.3.2 Theoretical results 88

6.4 Conclusions 96

7 Conclusions and further work **103**

List of publications **107**

Acknowledgements **109**

Chapter 1

Introduction

1.1 Water, a current mystery

> *Empty your mind, be formless. Shapeless, like water. If you put water into a cup, it becomes the cup. You put water into a bottle and it becomes the bottle. You put it in a teapot, it becomes the teapot. Now, water can flow or it can crash. Be water, my friend.*
>
> Bruce Lee, 1971.

If one asked several people with different backgrounds which substance they believe is the most important to the human being, water would probably be one of the most frequent answers. Water, essential substance for the creation of life, and object of extreme importance in various human activities (religion, art, economy...), it has also been one of the main characters in the history of science. Due to its abundance and presence in our everyday life, there are few scientific disciplines in which water does not appear, and in many of them it plays the central role. Considered as an element of nature in the ancient Greek times, nowadays, we know that the basic unit composing water is a molecule made of one oxygen and two hydrogen atoms . For a fluid made of such a simple molecule one could also expect water to show a simple and predictable behaviour. In fact, the opposite happens: it shows a very complex phenomenology and behaves very differently from the majority of other fluids [1]. The cause behind this unusual behaviour is still unclear, and the truth, although might seem embarrassing, is that we are still far from understanding water.

Many properties of water differ largely from the ones expected in a common fluid, and that is the reason why it is commonly called anomalous. For instance, the usual tendency of any liquid under cooling is to shrink and become denser, and once it solidifies, the solid sinks due to its higher density. At atmospheric pressure, water shows a density maximum at $T = 4$ °C, and at lower temperatures, it becomes lighter; even after solidification, ice still floats in water. These two subtle anomalies combined have enormous consequences on nature: rivers, lakes, and oceans freeze from the top down insulating the majority of water from the external conditions. Thereby, the ecology of the bottom is protected, sunlight is reflected back into space, ice rapidly thaws back, and the denser and warmer water at the bottom can easily transport heat. The latter, for instance, is a key point for maintaining the flow of Thermohaline circulation [1], which is crucial for the temperature distribution in the Earth. Another anomalous feature is the wider variety of crystal and amorphous structures that water has at different temperatures and pressures. Other materials typically show two or three different crystalline structures at different pressures and temperatures, while in the case of water, eighteen different crystalline ices and three different amorphous ices are known to exist.

The anomalies mentioned above belong to a large list consisting of more than 70 anomalous properties known to this date, and they are specially pronounced in the supercooled region of the phase diagram, below 0 °C. Which is the origin of these anomalies? This is the key question that remains unanswered, and has motivated scientists to propose various models to describe water. The majority of the models proposed during the last century can be classified into two categories: mixture and continuum models. In the former, it is assumed that water is a mixture of an ordered ice-like and lighter component, and a less ordered high density one. The concentration of the two components changes with temperature and pressure, and thereby, explains the complex behaviour of water. Within this category are the simple two state model [2], hydrone theory of water [3], interstitial model [4] and clathrate model [5]. In the continuous models, instead of being surrounded by two clearly distinguishable structures, the local environment of the molecules changes of density smoothly, caused by the continuous bend of the hydrogen bonds. Within this category are the Bernal-Fowler model [6], and the more recent percolation hypothesis [7].

The discovery of a high-density and a low density amorphous ice connected by a first-order phase transition [8] resulted in the proposal that nowadays seems to be the best candidate to explain the complex behavior of water: the liquid-liquid critical

point (LLCP) hypothesis [9]. This hypothesis predicts that at low temperatures of the phase diagram, water has two liquid metastable states, a low-density liquid at low pressures and a high density liquid at high pressures, both connected by a first-order phase transition line that ends into a second critical point predicted to be at $T_c \approx 220$ K, $P_c \approx 100$ MPa, and $\rho_c \approx 1$ g cm^{-3}. How can a critical point explain the anomalous behavior of water in another location of the phase diagram? Because critical points are not local phenomena, i.e., their existence affects certain area of the phase diagram. In the case of water, its effects would be more intense in the region where the supercooled liquid is found. The validity of this hypothesis is still unclear, and the main reason is that the hypothetical second critical point would be located within the so called "no man's land" [10]: a region in the phase diagram where the nucleation of liquid is impossible to avoid, and experiments with the liquid can not be carried out. Although in the last years, there have been various indirect experimental [11, 12] and computational [9, 13–19] evidences supporting the LLCP hypothesis, still the proof of its validity is a current scientific task.

1.2 Confined water

Thanks to the great technological advances that occurred during the last few decades, scientists have been able to carry out experiments and computational simulations with water under strong confinement. One of the general conclusions that has emerged from these studies is that confined water shows a very different behavior with respect to its bulk counterpart, but still a very reach and complex phenomenology [20–22]. Why should scientists study the properties of water under these extreme conditions, far from the usual ones in which we are used to experience water? There are two main reasons to explain the scientific importance and the great implications that the study of confined water has.

The first reason is its key presence in various important systems within different scientific disciplines. In biology, for instance, one of the most important current tasks is to know the structure of water within a living cell [23]. The medium within living cells is called cytoplasm, and it is mainly composed by water containing different types of biomolecules, such as, proteins, DNA, sugar and salts. In many regions of the cytoplasm, the space between biomolecules is of the size of few water molecular diameters, and the structure of the water that fills these spaces is unknown. In the case of the proteins,

their shape is known to be determinant for carrying out the function that they have been designed for. A shape that, many times, is achieved when the proteins are immersed only in water, having the precisely right distribution of hydrophobic and hydrophilic parts within it. The importance and active role of water in molecular biology is very well highlighted in the next cite written by the biologists Mark Gerstein and Michael Levitt (Nobel Price of Chemistry in 2013) [24]:

> When scientists publish models of biological molecules in journals, they usually draw their models in bright colors and place them against a plain, black background. We now know that the background in which these molecules exist - water - is just as important as they are.

In geology, the structure and dynamics of water inside the pores of different minerals, such as, clay and calcium silicate, strongly determine their structural and rheological properties. The presence of confined water is a factor that frequently has to be taken into account also in nanotechnology.

The second reason for the importance of studying confined water is that it can shed light on understanding the nature of water itself. The structural and dynamical properties of confined water have been observed to be very different from the bulk and complex. Studies have shown that the melting temperature of water can be increased or decreased depending on the type of confinement [22, 25, 26], allowing to shift bulk's phase diagram and hoping to reach regions that are usually hard to experiment with. Thereby, a different way of facing the mystery of water anomalies previously mentioned can be adopted. In fact, many studies have tried to prove the LLCP hypothesis by analyzing confined water, where singular critical phenomena that happen in the bulk are known to behave as maxima in the sufficiently confined conditions [20].

1.2.1 Thermodynamics

Depending on the hydrophilic/hydrophobic nature of the confining substrate, and its dimensions, water would like to fill it in the liquid or the vapor phase. At which dimensions does one phase become more stable than the other?

Lets consider two plates of dimensions $L \times L$ and separated by a distance D immersed in a water bath with a chemical potential μ at temperature T (see Figure 1.1). For this ensemble, the grand potential defined as $\Omega = U - TS - \mu N$ has a minimum

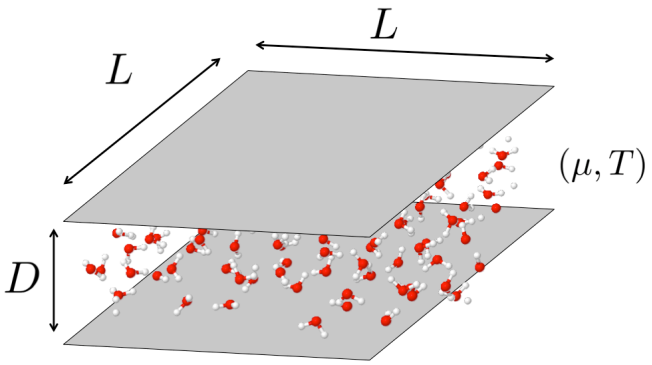

Figure 1.1: Illustration of two parallel plates of dimensions $L \times L$ separated by a distance D immersed in water with a given chemical potential μ and temperature T. The water molecules outside the confined space have been removed for clarity. Depending on the distance D, the confined space is filled by the liquid or the vapor phase.

at equilibrium. From the definition of the Gibbs free energy $G = U - TS + PV$, the grand potential can be rewritten as $\Omega = G - \mu N - PV$. Assuming that the two plates are well separated, the Gibbs free energy can be expressed as $G = \gamma A + \mu N$, where γ is the interfacial free energy density, and A is the interfacial area. Therefore, the grand potential of the liquid Ω_l and vapor Ω_v filling the space between the plates can be expressed respectively:

$$\Omega_l = 2\gamma_{sl}L^2 - P_l L^2 D, \tag{1.1}$$

$$\Omega_v = 2\gamma_{sv}L^2 + 4\gamma_{lv}LD - P_v L^2 D, \tag{1.2}$$

where γ_{sl}, γ_{sv}, and γ_{lv} are the solid-liquid, solid-vapor, and liquid-vapor free energy densities, and P_l and P_l are the pressures of the vapor and the liquid phases at the fixed μ and T respectively. By equating the Eqs. (1.1) and (1.2), we can extract the critical plates separation D_c below which the vapor is stable and the liquid becomes a metastable phase:

$$D_c = \frac{2(\gamma_{sl} - \gamma_{sv})}{(P_l - P_v) + \dfrac{4\gamma_{lv}}{L}}. \tag{1.3}$$

Using Young's equation, $\gamma_{sl} - \gamma_{sv} = -\gamma_{lv}\cos\theta$, we can rewrite Eq. (1.3) in terms of the contact angle θ of the liquid in the solid surface:

$$D_c = \frac{-2\gamma_{lv}\cos\theta}{(P_l - P_v) + \dfrac{4\gamma_{lv}}{L}}. \tag{1.4}$$

For fully impermeable plates ($\theta = \pi$) Eq. (1.4) transforms into:

$$D_c = \frac{2\gamma_{lv}}{(P_l - P_v) + \dfrac{4\gamma_{lv}}{L}}. \tag{1.5}$$

For sufficiently subcritical conditions, and taking into account that P_v is of the same order of magnitude to the vapor pressure, $P_l \gg P_v$ can be assumed [21]. We can analyze two limiting cases of Eq. (1.5): when the dimensions of the plates are small and large. For the former, assuming that the liquid in which the plates are immersed is at ambient pressure $P_l = 1$ bar, and the typical value of γ_{lv} of many liquids is of the order of $10^{-3} - 10^{-2}$ Nm^{-1}, the term $\dfrac{4\gamma_{lv}}{L}$ starts to be predominant with respect to $(P_l - P_v)$ in Eq. (1.5) when the dimensions of the plates are on the nanoscale. At these conditions, the Eq. (1.5) is simply:

$$D_c = \frac{L}{2}. \tag{1.6}$$

Note that Eq. (1.6) only depends on the dimensions of the plates, independently from the type of liquid, temperature, and pressure.

The second limiting case is when the dimensions of the plates are large enough, so that, $\dfrac{4\gamma_{lv}}{L(P_l - P_v)} \ll 1$. In this case, Eq. (1.5) can rewritten as:

$$D_c = \frac{2\gamma_{lv}}{(P_l - P_v)}. \tag{1.7}$$

For water at ambient pressure, this expression works when the dimensions of the plates are in the order of the microscale [21].

1.2.2 State-of-the-art

Confined water starts to behave differently from the bulk when the confining space is around 20 - 30 Å in some of the dimensions [27, 28]. One can imagine that both, introducing the liquid inside such a narrow space, and obtaining information of such small quantity of water, are experimental tasks hard to achieve even nowadays. Although the quantity of experimental works done about confined water is limited, all agree that under strong confinement the properties change dramatically with respect to the bulk.

Previous experimental studies of water confined one-dimensionally in nafion, xerogels [27], carbon nanotubes [27, 28], and mesoporous silica materials [29] have shown unusual properties, such as, different proton momentum distribution with respect to

the one in the bulk [27], extreme phase transition temperatures [28], anomalous ground state of valence electrons [30], and a hydrophobic-hydrophilic transition induced by the temperature [31]. Mallamace *et al.* observed indirect evidences of the existence of the LLCP by confining water in mesoporous silica materials [29]. There are even less studies of two-dimensionally confined water due to the difficulty of the experiments. A study of water confined between a cantilever and different types of substrate has shown that the viscous shear forces in nanoconfined water can be orders of magnitude larger than in the bulk [32]. The so called 2D materials (graphene, MoS_2, silicene,...) are promising candidates in order to study two-dimensionally confined water, because they are by nature two-dimensional, and the little amount of confining material involved in the system increases the relative signal coming from the confined water in an experiment. Algara *et al.* have recently analyzed water confined between two graphene sheets under electronic radiation with the high resolution transmission electron microscope. They observed that water freezes into a highly-packed square-ice at ambient temperature [33].

Until now, the great majority of studies on confined water have been carried out by computational simulations mainly because they avoid many difficulties that appear on the experimental side. The initial positions and velocities of the particles involved in the system are easily fixed, and thereby, the confining space can be easily filled with water and be designed in a precise way. Moreover, information that comes only from the aqueous component is more straightforward to obtain. The main problem coming from computer simulations is that the interaction among water molecules is not sufficiently well described.

As previously mentioned water is known to strongly determine the behavior of the biological molecules, and therefore for a proper simulation it is usually mandatory to immerse them in water. When the amount of particles in the simulation box is large, the classical force-fields are usually employed due to their low computational cost compared to *ab initio* calculations. The atoms within the molecules are considered as point particles and a classical force-field is assigned to each of them. The parameters that define these water models are derived empirically to reproduce some experimental properties of water in the simulations or by *ab inito* accurate calculations. A previous review counts 46 classical water models [34], which are usually classified based on three characteristics: the number of interaction points within the molecule (sites), rigidity or flexibility, and polarizability. In a recent study, Vega *et al.* [35] calculate 17 properties of water with five rigid non-polarizable water models (TIP3P, TIP5P, TIP4P, SCP/E and

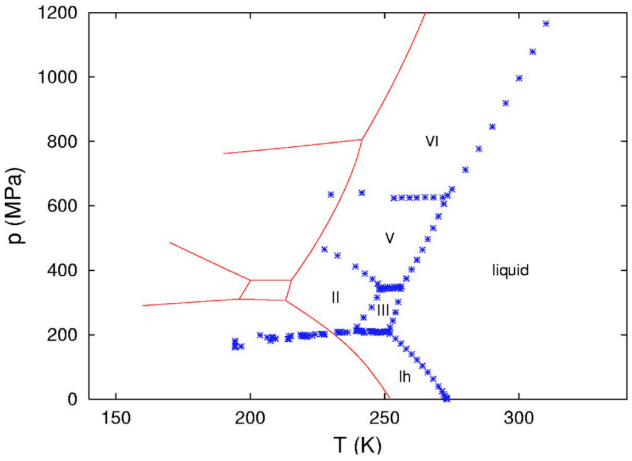

Figure 1.2: Figure from *http://dx.doi.org/10.1063/1.2121687* [36] by J. L. Abascal and C. Vega. Temperature-density phase diagram of water obtained experimentally (red line) and by simulations with the TIP4P/2005 force-field (blue points).

TIP4P/2005) that are commonly used in the scientific community. The comparison between the obtained results with the experimental properties of water shows that the TIP4P/2005 model gives the best description among the five models. Although the introduction of flexibility and polarizability in the water molecule is expected to improve the description of the water interaction, they also increase the computational cost of the simulations, which is an important factor to take into account.

Fig 1.2 obtained from [36] shows the comparison between the phase diagram of water obtained experimentally and by computer simulations with the TIP4P/2005 force-field. Apart from the shift in pressure and temperature between both phase diagrams, the behavior of the different phases is well described.

One of the problems of empirically constructed classical force-fields is that their parameters are chosen to mimic experimental results of bulk water, and therefore, they lose their reliability once water is at extreme conditions, such as, under strong confinement. The simulations based on *ab initio* methods in theory should give a better description of the interactions in water, but still have a great limitation with the number of particles and simulation time due to the large computational cost. One of the first studies employing density functional theory (DFT) based molecular dynamics simulations with 32 water molecules [37] showed that the local-density approximation was not accurate enough to reproduce the hydrogen bonding in the liquid while the semi-local generalized gradient approximation (GGA) could. Grossman *et al.* [38] realized that

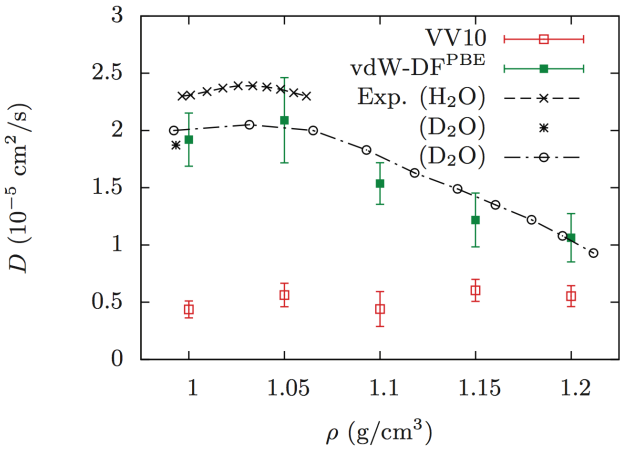

Figure 1.3: Figure from *http://aip.scitation.org/doi/abs/10.1063/1.4832141* by Corsetti *et al.* [39]. Room-temperature diffusivity with respect to the density obtained by AIMD calculations with the vdW-DF^{PBE} and VV10 functionals, and experimentally.

if the PBE and the BLYP GGA functionals were employed for the simulations, water tended to over structure decreasing its diffusivity by a factor of 10. Recent simulations employing non-local functionals that take into account the Van der Waals interaction reproduce better the experimental behavior of liquid water. Corsetti *et al.* [39] have recently compared the results obtained by two vdW density functional: the vdW-DF^{PBE} and VV10. Both give a smooth equation of state, but more importantly, the calculations with the vdW-DF^{PBE} accurately reproduced the maximum of diffusivity as a function of density. To our knowledge, this is the first time that this maximum has been reproduced by *ab initio* calculations. Fig 1.3 obtained from [39] shows the comparison of the room-temperature diffusion obtained by AIMD calculations with both vdW density functionals and the experimental results.

Extensive work has been done studying the structural, and dynamical properties of water under one-dimensional [42–44] and two-dimensional [22, 25, 26, 45–65] confinement by computational simulations. Many unusual and interesting results have been observed, such as, large variety of crystallographic structures [25, 45–50], unusual phase transitions [25], indirect evidences of the LLCP hypothesis [63], increase/decrease of the melting temperature and the response functions within the phase diagram depending on the nature of the confinement [22, 26, 51–54], and even the need to reformulate the so-called ice rules for monolayer ices [55].

One of the causes that produces such changes comes from the intrinsic tendency

of any fluid to behave differently when it is strongly confined in some of the dimensions. A common way to study these intrinsic properties by computational simulations has been the use of simple confining potentials that depend on few parameters, avoiding possible effects that may be produced by particularities of the chosen confining substrate. However, in order to obtain a general understanding of the aqueous system, it is necessary to take into account the influence produced by the confining substrate. Computer simulations using atomistic surfaces, and realistic protein-like surfaces have shown that the behavior of water changes drastically compared to the one observed using smooth surfaces. Factors, such as, surface geometry, topography, and chemical heterogeneity have been observed to play crucial roles [21]. These results point out the importance to quantify the influence that intrinsic and extrinsic factors have in confined water, and determine which of the two becomes more influential in which situation.

Algara *et al.* [33] have recently observed experimentally that water is structured into a high density square ice made of different numbers of layers depending on the available space between two graphene sheets at ambient temperature. Computational studies agree that under two-dimensional nanoconfinement, water is structured into layers perpendicularly oriented with respect to the confining direction (monolayer [22, 45, 48, 54–59], bilayer [25, 46, 47, 49–53, 60, 61], trilayer and so on [26, 60, 62–65]). Most of the computational studies agree with the existence of a stable monolayer square ice phase at similar densities [22, 45, 55, 56]. For the bilayer and trilayer cases, although there are recent studies getting the square ice [22, 45, 55, 56], still the majority obtain different types of structure as the most stable ones. Han *et al.* [25] observed by classical molecular dynamics simulations using the TIP5P force-field model [66] that nanoconfined bilayer water at similar densities freezes into a rhombic ice, and that this solid is connected by an unusual continuous phase transition with the liquid. Bai and Zeng [48] describe a similar solid at this density, but they define it instead as very-high-density bilayer amorphous ice. A recent work by Corsetti*et al.* [60] based on density-functional theory, distinguishes two different stable bilayer ices at high densities: a proton-ordered rhombic phase for low temperatures and a proton-disordered triangular phase for high temperatures. Still nowadays there is controversy about the structure that water adopts under these conditions. Even few months later from the publication of Algara*et al.*, the same authors commented that they were not able to reproduce the experiment, and that the observed square crystals could be due to accidental contamination.

1.3 This thesis

The main aim of this thesis is to study and understand the unusual properties of water under two-dimensional confinement by means of computational simulations. We specially focus on the study of the properties caused by the intrinsic tendencies of the liquid due to the confinement, and the extrinsic properties caused by the particular confining substrate-water interaction. The thesis is divided into seven chapters:

Chapter 1 is an introduction to the topic: the scientific state-of-the-art of bulk and confined water are described, and the thermodynamics of a confined fluid is briefly explained.

Chapter 2 establishes the theoretical basis in which the classical and *ab initio* molecular dynamics simulations are based on, and describes the mathematical functions employed for the data analysis.

Chapter 3 describes the different ices obtained under a planar confinement at different temperatures and densities of the phase diagram, and studies the phase transition between them. Among the three ices described, a proton-disordered triangular ice is observed for the first time under these confinement conditions by MD simulations.

Chapter 4 focuses on the description of the confined liquid and the phase transitions with the solids under a planar confinement. At high densities, a continuous melting is observed to be related to the phase change of the oxygens only, with the hydrogens remaining liquid-like throughout. Moreover, we find an intermediate hexatic phase for the oxygens between the liquid and a triangular solid ice phase, following the Kosterlitz-Thouless- Halperin-Nelson-Young theory for two-dimensional melting.

In **Chapter 5**, we propose a new model for the confinement that introduces a smoothly controlled roughness. We analyze how the previously studied intrinsic properties of water are altered by the introduction of the roughness.

As previously mentioned, 2D materials are promising substrates to experimentally confine water. **Chapter 6** studies the effects produced by the electronic radiation on a dry bilayer graphene sample, as the previous step of simulating confined water between graphene layers in the transmission electron microscope. As in this chapter we do not study water, and the employed methods differ from the ones used in the rest of the thesis, it has its own *introduction*, *methods* and *conclusions* sections.

Chapter 7 summaryzes the main results and conclusions achieved in this thesis. It also proposes further work to carry out in the future to follow the line of study of this thesis.

References

[1] P. Ball, (2015) H2O: A biography of water, Hachette UK, .

[2] W. C. Röntgen, (1892) *Annalen der Physik* **281(1)**, 91–97.

[3] H. E. Armstrong, (1924) *Nature* **113**, 163.

[4] O. Y. Samoilov, (1963) *Journal of Structural Chemistry* **4(4)**, 459–461.

[5] L. Pauling, (2013) *Hydrogen Bonding*, 1–6.

[6] J. L. Finney, (2007) In Journal of Physics: Conference Series volume **57**, IOP Publishing : p. 40.

[7] H. E. Stanley and J. Teixeira, (1980) *J. Chem. Phys.* **73(7)**, 3404–3422.

[8] O. Mishima, L. Calvert, and E Whalley, (1985) *Nature* **314(6006)**, 76–78.

[9] P. Poole, F. Sciortino, U. Essman, and H. Stanley, (1992) *Nature* **360**, 324–328.

[10] O. Mishima and H. E. Stanley, (1998) *Nature* **396(6709)**, 329–335.

[11] M. C. Bellissent-Funel and L. Bosio, (1995) *J. Chem. Phys.* **102(9)**, 3727–3735.

[12] G. Schirò, M. Fomina, and A. Cupane, (2013) *J. Chem. Phys.***139**, 121102

[13] P. H. Poole, F. Sciortino, U. Essmann, and H. E. Stanley, (1993) *Phys. Rev. E* **48(5)**, 3799.

[14] H. Tanaka, (1996) *J. Chem. Phys.* **105(12)**, 5099–5111.

[15] S. Harrington, R. Zhang, P. H. Poole, F. Sciortino, and H. E. Stanley, (1997) *Phys. Rev. Lett.* **78(12)**, 2409.

[16] F. Sciortino, P. H. Poole, U. Essmann, and H. Stanley, (1997) *Phys. Rev. E* **55(1)**, 727.

[17] S. Harrington, P. H. Poole, F. Sciortino, and H. E. Stanley, (1997) *J. Chem. Phys.* **107(18)**, 7443–7450.

[18] I. Brovchenko, A. Geiger, and A. Oleinikova, (2005) *J. Chem. Phys.* **123(4)**, 044515.

[19] T. A. Kesselring, E. Lascaris, G. Franzese, S. V. Buldyrev, H. J. Herrmann, and Stanley, H. E. (2013) *J. Chem. Phys.* **138(24)**, 244506.

[20] C. E. Bertrand, Y. Zhang, and S.-H. Chen, (2013) *Phys. Chem. Chem. Phys.* **15(3)**, 721–745.

[21] N.Giovambattista, P. Rossky, and P. Debenedetti, (2012) *Annu. Rev. Phys. Chem.* **63**, 179–200.

[22] R. Zangi, (2004) *J. Phys. Condens. Matter* **16(45)**, S5371.

[23] P. Ball, (2008) *Chem. Rev.* **108(1)**, 74–108.

[24] M. Gerstein and M. Levitt, (1998) *Sci. Am.* **Nov.**, 100–105.

[25] S. Han, M. Choi, P. Kumar, and H. E. Stanley, (2010) *Nat. Phys.* **6(9)**, 685–689.

[26] P. Kumar, S. V. Buldyrev, F. W. Starr, N. Giovambattista, and H. E. Stanley, (2005) *Phys. Rev. E* **72(5)**, 051503.

[27] G. F. Reiter, A. I. Kolesnikov, S. J. Paddison, P. Platzman, A. P. Moravsky, M. A. Adams, and J. Mayers, (2012) *Phys. Rev. B* **85(4)**, 045403.

[28] K. V. Agrawal, S. Shimizu, L. W. Drahushuk, D. Kilcoyne, and M. S. Strano, (2016) *Nat. Nanotech.*

[29] F. Mallamace, M. Broccio, C. Corsaro, A. Faraone, D. Majolino, V. Venuti, L. Liu, C.-Y. Mou, and S.-H. Chen, (2007) *P. Natl. A. Sci.* **104(2)**, 424–428.

[30] G. Reiter, A. Deb, Y. Sakurai, M. Itou, V. Krishnan, and S. Paddison, (2013) *Phys. Rev. Lett.* **111(3)**, 036803.

[31] H.-J. Wang, X.-K. Xi, A. Kleinhammes, and Y. Wu, (2008) *Science* **322(5898)**, 80–83.

[32] D. Ortiz-Young, H.-C. Chiu, S. Kim, K. Voïtchovsky, and E. Riedo, (2013) *Nat. Commun.* **4**

[33] G. Algara-Siller, O. Lehtinen, F. Wang, R. Nair, U. Kaiser, H. Wu, A. Geim, and I. Grigorieva, (2015) *Nature* **519(7544)**, 443–445.

[34] B. Guillot, (2002) *J. Mol. Liq.* **101(1-3)**, 219–260.

[35] C. Vega and J. L. Abascal, (2011) *Phys. Chem. Chem. Phys.* **13(44)**, 19663–19688.

[36] J. L. Abascal and C. Vega, (2005) *Phys. Chem. Chem. Phys.* **123(23)**, 234505.

[37] K. Laasonen, M. Sprik, M. Parrinello, and R. Car, (1993) *J. Chem. Phys.* **99(11)**, 9080–9089.

[38] J. C. Grossman, E. Schwegler, E. W. Draeger, F. Gygi, and G. Galli, (2004) *J. Chem. Phys.* **120(1)**, 300–311.

[39] F. Corsetti, E. Artacho, J. M. Soler, S. S. Alexandre, and M. V. Fernández-Serra, (2013) *J. Chem. Phys.* **139(19)**, 194502.

[40] J. Wang, G. Román-Pérez, J. M. Soler, E. Artacho, and M.-V. Fernández-Serra, (2011) *J. Chem. Phys.* **134(2)**, 024516.

[41] J. A. Morrone and R. Car, (2008) *Phys. Rev. Lett.* **101(1)**, 017801.

[42] L. Xu and V. Molinero, (2011) *J. Phys. Chem. B* **115(48)**, 14210–14216.

[43] S. Javadian, F. Taghavi, F. Yari, and S. M. Hashemianzadeh, (2012) *J. Mol. Graph. Model.* **38**, 40–49.

[44] F. Klameth and M. Vogel, (2013) *J. Chem. Phys.* **138(13)**, 134503.

[45] T. Kaneko, J. Bai, K. Yasuoka, A. Mitsutake, and X. C. Zeng, (2014) *J. Chem. Phys.* **140(18)**, 184507.

[46] J. Chen, G. Schusteritsch, C. J. Pickard, C. G. Salzmann, and A. Michaelides, (2016) *Phys. Rev. Lett.* **116(2)**, 025501.

[47] M. S. F. Mario, M. Neek-Amal, and F. Peeters, (2015) *Phys. Rev. B* **92(24)**, 245428.

[48] J. Bai and X. C. Zeng, (2012) *P. Natl. A. Sci.* **109(52)**, 21240–21245.

[49] J. Bai, X. Zeng, K. Koga, and H. Tanaka, (2003) *Mol. Simulat.* **29(10-11)**, 619–626.

[50] K. Koga, X. C. Zeng, and H. Tanaka, (1997) *Phys. Rev. Lett.* **79(26)**, 5262.

[51] N. Giovambattista, P. J. Rossky, and P. G. Debenedetti, (2009) *Phys. Rev. Lett.* **102(5)**, 050603.

[52] J. Slovak, K. Koga, H. Tanaka, and X. C. Zeng, (1999) *Phys. Rev. E* **60(5)**, 5833.

[53] J. C. Johnston, N. Kastelowitz, and V. Molinero, (2010) *J. Chem. Phys.* **133(15)**, 154516.

[54] M. G. Mazza, K. Stokely, H. E. Stanley, and G. Franzese, (2012) *J. Chem. Phys.* **137(20)**, 204502.

[55] F. Corsetti, P. Matthews, and E. Artacho, (2016) *Sci. Rep.* **6**

[56] R. Zangi and A. E. Mark, (2003) *Phys. Rev. Lett.* **91(2)**, 025502.

[57] F. deLos Santos and G. Franzese, (2012) *Phys. Rev. E* **85(1)**, 010602.

[58] E. G. Strekalova, M. G. Mazza, H. E. Stanley, and G. Franzese, (2011) *Phys. Rev. Lett.* **106(14)**, 145701.

[59] F. de losSantos and G. Franzese, (2011) *J. Phys. Chem. B* **115(48)**, 14311–14320.

[60] F. Corsetti, J. Zubeltzu, and E. Artacho, (2016) *Phys. Rev. Lett.* **116(8)**, 085901.

[61] L. B. Krott and M. C. Barbosa, (2013) *J. Chem. Phys.* **138(8)**, 084505.

[62] N. Giovambattista, P. J. Rossky, and P. G. Debenedetti, (2006) *Phys. Rev. E* **73(4)**, 041604.

[63] M. Meyer and H. E. Stanley, (1999) *J. Phys. Chem. B* **103(44)**, 9728–9730.

[64] P. Kumar, F. W. Starr, S. V. Buldyrev, and H. E. Stanley, (2007) *Phys. Rev. E* **75(1)**, 011202.

[65] H. Mosaddeghi, S. Alavi, M. Kowsari, and B. Najafi, (2012) *J. Chem. Phys.* **137(18)**, 184703.

[66] M. W. Mahoney and W. L. Jorgensen, (2000) *J. Chem. Phys.* **112(20)**, 8910–8922.

Chapter 2

Methods

In this chapter we describe the theoretical basis and computational methods employed to carry out the molecular dynamics simulations and the data analysis.

2.1 Dynamics

In this thesis, all the computational simulations of nanoconfined water are carried out by means of classical force-fields (MD) or *ab inito* molecular dynamics (AIMD). Initially, water is confined between two parallel walls and the initial positions and velocities of the particles are randomly set. Then, the molecules are let to interact among them for a certain period of time, long enough to reach thermodynamic equilibrium. Finally, data are collected and the desired physical magnitude is obtained. In order to build up the trajectories that the particles follow, the equations of motion have to be solved, which depend on the adopted ensemble during the simulation.

2.1.1 Ensembles and thermostats

In an isolated system, the trajectories of the particles map a **microcanonical** (NVE) ensemble of microstates. The macroscopic variable number of particles (N), volume (V), and energy (E) of the system are constants during the MD simulation. Once the system reaches thermal equilibrium, the instantaneous observable chemical potential (μ), pressure (P), and temperature (T) fluctuate around well-defined average values.

The equation of motion for a particle i within this ensemble is:

$$\ddot{\mathbf{r}}_i(t) = \frac{\mathbf{F}_i(t)}{m_i}, \tag{2.1}$$

where, $\mathbf{F}_i(t)$ is the total inter-particle force acting on the particle i of mass m_i.

However, usually in experiments, the systems exchange energy with an environment. For instance, if the system is in contact with a heat bath, it gains or loses energy until reaching thermal equilibrium. If one is interested in representing a system with a specific average value of temperature, the **canonical** (NVT) ensemble should be adopted. To set a target temperature on the MD simulation, the equations of motion of the system are modified by a thermostat algorithm that ensures a constant average value of the temperature.

Using the equipartition of energy over all degrees of freedom, the instantaneous temperature of the simulated system is obtained from the average kinetic energy:

$$T(t) = \sum_{i=1}^{N} \frac{m_i v_i^2(t)}{k_b N_{df}}, \tag{2.2}$$

where N_{df} is the number of degrees of freedom and k_B is Boltzmann's constant.

A way to set the temperature of the simulated system is by coupling it to the **Berendsen thermostat** [1]. The rate of change of temperature is forced to be proportional to the difference with the target temperature T_0 by scaling the velocity of the particles:

$$\dot{T}(t) = \frac{T_0 - T(t)}{\tau_B}, \tag{2.3}$$

where τ_B is an empirical parameter that determines the strength of the coupling between the system and the heat bath. Values of $\tau_B \sim 0.1$ ps are usually considered appropriate in MD simulations. The equation of motion of a particle i of a system coupled with the Berendsen thermostat is:

$$\ddot{\mathbf{r}}_i(t) = \frac{\mathbf{F}_i(t)}{m_i} - \frac{1}{2}\tau_B^{-1}\left(\frac{T_0}{T(t)} - 1\right)\dot{\mathbf{r}}_i(t). \tag{2.4}$$

Although the Berendsen thermostat allows a smooth and efficient transition from an initial to a target temperature, the generated ensemble is not canonical, underestimating the temperature fluctuations.

The **Nosé-Hoover thermostat** generates the equations of motion that sample a canonical ensemble. The idea behind is to extend the system with a new artificial

variable $s(t)$, velocity $\dot{s}(t)$, and mass Q>0, with which the real system can exchange energy to obtain the target temperature T_0. It can be shown [2] that the equations of motion of this extended system are:

$$\ddot{\mathbf{r}}_i(t) = \frac{\mathbf{F}_i(t)}{m_i} - \frac{\dot{s}(t)}{s(t)}\mathbf{r}_i(t), \tag{2.5}$$

$$\ddot{s}(t) = -\frac{k_B N_{df}\, s(t)}{Q}\left[T_0 - T(t)\right] + \frac{\dot{s}(t)^2}{s(t)}, \tag{2.6}$$

where N_{df} is the number of internal degrees of freedom of the real system. The Nosé-Hoover equations of motion generate the correct thermal fluctuations for a canonical ensemble.

In many experiments, not only the temperature is controlled, but also the pressure. In order to simulate such systems, or to reach the desired value of the pressure and the temperature by MD simulations, the **isobaric-isothermal** (NPT) ensemble is adopted. The system is allowed to exchange energy with a thermal bath to change its temperature and, at the same time, the volume of the simulation box is allowed to change until reaching the right value of the pressure. Although there are many different methods to obtain different equations of motion that set the temperature and pressure of the system [3], we describe those used in this thesis. The employed equations of motion are derived by Shinoda *et al.* [4] that combine the hydrostatic equations of Martyna *et al.* [5] with the strain energy proposed by Parrinello and Rahman [6].

In our case, as the system is strongly confined in one of the dimensions, we distinguish the perpendicular $P_\perp$ and lateral $P_\parallel$ pressures. The former is obtained by calculating the total perpendicular force acting on the confining wall divided by the area of the cell:

$$P_\perp = \sum_{i=1}^{N} \frac{F_{z,i}}{A_{\text{cell}}} \tag{2.7}$$

The lateral pressure is obtained from the components of the Virial tensor:

$$P_{xx} = \frac{\sum_{i=1}^{N} m_i v_{x,i}^2}{V_{\text{cell}}} + \frac{\sum_{i=1}^{N} r_{x,i} F_{x,i}}{V_{\text{cell}}}, \tag{2.8}$$

$$P_{yy} = \frac{\sum_{i=1}^{N} m_i v_{y,i}^2}{V_{\text{cell}}} + \frac{\sum_{i=1}^{N} r_{y,i} F_{y,i}}{V_{\text{cell}}}. \tag{2.9}$$

Then, the averaged value is calculated:

$$P_\parallel = \frac{P_{xx} + P_{yy}}{2} \tag{2.10}$$

Once the equations of motion are known, a time-integrator algorithm has to be employed to solve them and predict the new positions of the particles.

2.1.2 Time-integrators

A *good* integrator algorithm is characterized by being time-reversible, area-preserving, energy-conserving in short and long time, and accurate for large time steps [3]. Due to numerical errors inherent to any computational simulation, no integrator reproduces the correct trajectory of the particles in a system. However, this is not usually a problem, as the vast majority of the MD simulations are only interested on the statistical predictions. Depending on the equations of motion that have to be solved, different integrators are more efficient than others. Here, we describe those used in this thesis.

The simplest and usually the best [3] time-integrator is the **Verlet algorithm**, that is obtained by a Taylor expansion of the positions around time t. The next position of a particle with respect to the previous positions and acceleration is:

$$\mathbf{r}(t+\delta t) = 2\mathbf{r}(t) - \mathbf{r}(t-\delta t) + \ddot{\mathbf{r}}(t)\delta t^2 + \mathcal{O}(\delta t^4). \tag{2.11}$$

Although the velocities are not necessary to build up the trajectories of the particles, they are useful to calculate some physical quantities, like the kinetic energy and temperature. The velocities are calulated by using the mean value theorem:

$$\dot{\mathbf{r}}(t) = \frac{\mathbf{r}(t+\delta t) - \mathbf{r}(t-\delta t)}{2\delta t} + \mathcal{O}(\delta t^2). \tag{2.12}$$

Note that first, it is necessary to calculate $\mathbf{r}(t+\delta t)$ in order to obtain $\dot{\mathbf{r}}(t)$. The importance of the election of the time step is pointed out on the Eqs. 2.11 and 2.12, as the error on the predicted positions and velocities is proportional to δt^4 and δt^2 respectively. δt should be small enough so the conservation of the energy, momentum, and time-reversibility are guaranteed. But at the same time, it should be large enough to carry out the whole simulation in a modest number of steps. In this thesis, we use the Verlet algorithm when the NVE and the NVT ensemble with the Berendsen thermostat are employed. When the equations of motion are more complex, like in the case of the Nosé-Hoover thermostat and the NPT ensemble, Taylor expanded integrators produce substantial energy drifts [3], and different time-integrators are usually employed. Tuckerman *et al.* [7] showed the possibility to systematically derive a time-reversible and area preserving time-integrator using the Liouville formulation of classical mechanics.

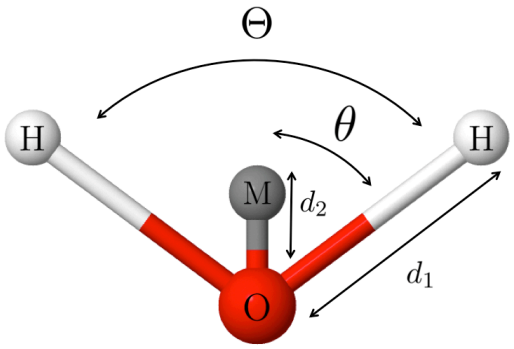

Figure 2.1: Illustration of the TIP4P/2005 water model characterized by having four sites with two distance (d_1, d_2) and two angle (θ, Θ) constraints.

The time-integrators employed for the Nosé-Hoover thermostat and NPT ensemble are derived by Tuckerman *et al.* [8] expressed by means of the Liouville operator.

Note that, in order to know the explicit form of the equations of motion, it is necessary to know the interatomic forces $\mathbf{F}_i(t)$ acting on the particles.

2.1.3 Atomic interaction

We describe the interaction among particles in water and obtain the interatomic forces $\mathbf{F}_i$ in two ways: based on classical empirical force-fields and density functional theory (DFT).

Classical Molecular Dynamics

In this thesis, we employ the **TIP4P/2005** force-field [9], which is a four-site, rigid and non-polarizable water model. Fig 2.1 shows an illustration of the TIP4P/2005 water molecule. It consists of one oxygen (O), two hydrogen (H) and a massless (M) atoms. The relative distances and angles (d_1, d_2, θ, and Θ in Fig 2.1) among the four particles are set to certain values and hence, the molecule is rigid. The force-field assigned to the oxygen atom is a Lennard-Jones potential, which only interacts with the oxygens of the other molecules:

$$U_{12\text{-}6} = 4\epsilon_{\mathrm{O}} \left[\left(\frac{\sigma_{\mathrm{O}}}{r} \right)^{12} - \left(\frac{\sigma_{\mathrm{O}}}{r} \right)^{6} \right]. \tag{2.13}$$

The cutoff of the Lennard-Jones interaction is set to 12 Å. In the case of the H and M sites, a point charge q_{H} and q_{M} is assigned respectively, so they interact via the classical Coulomb potential:

$$U_{\mathrm{C}} = \frac{q}{4\pi\epsilon_0 r}. \tag{2.14}$$

Note that the hydrogen and massless particles do not interact with the oxygens. Table 2.1 shows all the values of the parameters that determine the TIP4P/2005 model.

As the Coulomb interaction is long-ranged, the truncation of the potential at a given distance would introduce significative errors in the MD simulation. However, as the force evaluation scales as $\mathcal{O}(N^2)$, the computational cost for a long-ranged force would rapidly increase with the number of particles in the simulation. Here, to evaluate the Coulomb interaction, we employ the more efficient particle-particle-particle-mesh (PPPM) method [10], which scales as $N \log N$. It is a Fourier based Ewald summation that splits the Coulomb potential into two parts: a short-range and a long-range contribution. The latter is estimated by solving Poisson's equation via the Fast-Fourier-Transform technique. To constrain the angles and distances among the four sites of the water molecule, the lagrange multipliers are introduced in the equations of motion and computed by the SHAKE algorithm [11]. All the classical MD simulations are carried out using the LAMMPS code [12].

ab Initio Molecular Dynamics

As in the previous method, the atomic nuclei are considered as point particles, but the electrons are treated quantum mechanically. The idea is first to obtain the electronic ground state of the system and then calculate the total force acting on each nucleus $\mathbf{F}_i$. The electronic ground state of the system is obtained by Density Functional Theory (DFT), based on the Hohenberg-Kohn theorems [13]. The first theorem states that the electron density $\rho(\mathbf{r})$, which only depends on three spatial coordinates, uniquely determines the ground state properties of a many-electron system. The second theorem defines an energy functional and proofs that the minimum of this functional is obtained with the correct ground state electron density. Employing the referential non-interacting

Table 2.1: Values of the parameters defining the TIP4P/2005 water model.

m_{O} (g/mol)	ϵ_{O} (kJ/mol)	σ_{O} (Å)	m_{H} (g/mol)	q_{H} (e)	q_{M} (e)	d_1 (Å)	d_2 (Å)	θ (°)	Θ (°)
15.9994	0.7749	3.1589	1.008	0.5564	-1.1128	0.9576	0.1546	52.26	104.52

electronic system proposed by Kohn and Sham [14], the electronic density is obtained from the individual electronic wavefunctions φ_i:

$$\rho(\mathbf{r}) = 2\sum_{i=1}^{N_s} \left|\varphi_i(\mathbf{r})\right|^2 . \tag{2.15}$$

For simplicity, the possible spin dependence is ignored and each state is occupied twice. Then, the ground electronic density state is obtained by minimizing the Kohn-Sham equation [14]:

$$E_{KS}[\rho] = \int \rho(\mathbf{r}) v_{\text{ext}}(\mathbf{r}) d\mathbf{r} + T[\rho] + \frac{1}{2}\iint \frac{\rho(\mathbf{r})\rho(\mathbf{r}')}{|\mathbf{r}-\mathbf{r}'|} d\mathbf{r} d\mathbf{r}' + E_{XC}[\rho], \tag{2.16}$$

where the four terms on the right are the interaction of the electrons with the nuclei of the atoms and with a possible external field, the electronic kinetic energy, the classical electron-electron interaction or Hartree term, and the exchange-correlation energy, respectively. From this expression, only the exchange-correlation term is unknown and different approximations called *functionals* are employed.

Once the electronic density is known, the forces acting on each nucleus are calculated:

$$\mathbf{F}_i = -\int \rho(\mathbf{r}') \frac{\partial v_{\text{ext}}(\mathbf{r}'-\mathbf{r}_i)}{\partial \mathbf{r}_i} d\mathbf{r}' + e^2 \sum_{i\neq j}^{N} Z_i Z_j \frac{\mathbf{r}_i - \mathbf{r}_j}{|\mathbf{r}_i - \mathbf{r}_j|}, \tag{2.17}$$

where, Z_i is the atomic number of the atom i.

We employ the SIESTA code [15] in order to minimize the Kohn-Sham equation and to carry out the *ab initio* molecular dynamics simulation (AIMD). To simplify the Kohn-Sham equation, we employ **pseudopotentials** in Troullier-Martins form [16] substituting the core-electrons of the atoms by an artificial atomic potential acting on the valence electrons. The main goal behind this approximation is to decrease the number of nodes of the wavefunctions and reduce the number of electrons on the many-body electronic system. The wavefunctions and operators are represented by an **atomic centered** basis set, that are obtained from the pseudo-atomic problem. We use a variationally-obtained double-ζ polarized basis, optimal for liquid water and ice [17–19]. For the exchange-correlation functional, we employ the correlation part of the well-established vdW-DF functional [20], with the exchange part of the PBE functional [21]. Previous studies have shown noticeable improvements of the calculated radial distribution functions of water due to a better description of H bonds [22] with this functional.

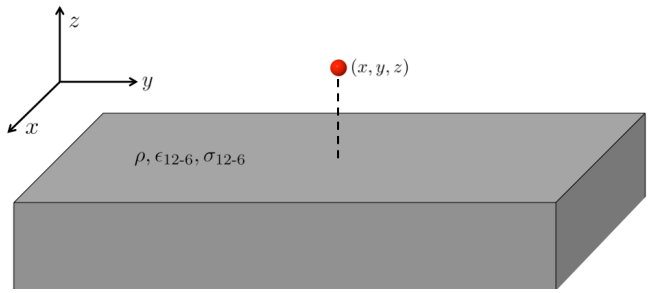

Figure 2.2: Illustration of a Lennard-Jones 9-3 solid interacting with a particle at (x,y,z).

2.2 Confining potential

In order to two-dimensionally confine water, we use two different potentials based on the Lennard-Jones 12-6 particles: a planar Lennard-Jones 9-3 potential and a rugous confining potential.

2.2.1 Planar potential

Consider a diffuse solid made of Lennard-Jones 12-6 particles with density ρ_{LJ} and parameters $\epsilon_{12\text{-}6}$ and $\sigma_{12\text{-}6}$ that fills the whole space under $z = 0$ (see Fig. 2.2). The total potential energy $U_{9\text{-}3}$ of a particle located at (x,y,z) that interacts with this solid is:

$$\begin{aligned}
U_{9\text{-}3} &= 4\epsilon_{12\text{-}6}\rho_{\text{LJ}} \int_{-\infty}^{0}\int_{0}^{\infty}\int_{0}^{2\pi}\left[\frac{\sigma_{12\text{-}6}^{12}}{[r^2+(z-z')^2]^6} - \frac{\sigma_{12\text{-}6}^{6}}{[r^2+(z-z')^2]^3}\right] r d\theta dr dz' \\
&= 8\pi\epsilon_{12\text{-}6}\rho_{\text{LJ}} \int_{-\infty}^{0}\left[\frac{-\sigma_{12\text{-}6}^{12}}{10[r^2+(z-z')^2]^5} + \frac{\sigma_{12\text{-}6}^{6}}{4[r^2+(z-z')^2]^2}\right]_{r=0}^{r=\infty} dz' \\
&= 8\pi\epsilon_{12\text{-}6}\rho_{\text{LJ}} \int_{-\infty}^{0}\left[\frac{\sigma_{12\text{-}6}^{12}}{10(z-z')^{10}} - \frac{\sigma_{12\text{-}6}^{6}}{4(z-z')^4}\right] dz' \\
&= 8\pi\epsilon_{12\text{-}6}\rho_{\text{LJ}} \left[\frac{\sigma_{12\text{-}6}^{12}}{90(z-z')^9} + \frac{\sigma_{12\text{-}6}^{6}}{12(z-z')^3}\right]_{z'=-\infty}^{z'=0} \\
&= \frac{4\pi\epsilon_{12\text{-}6}\rho_{\text{LJ}}}{3}\left[\frac{\sigma_{12\text{-}6}^{12}}{15z^9} + \frac{\sigma_{12\text{-}6}^{6}}{2z^3}\right].
\end{aligned} \tag{2.18}$$

By the next definition of new parameters $\epsilon_{9\text{-}3}$ and $\sigma_{9\text{-}3}$:

$$\epsilon_{9\text{-}3} = \frac{\pi \rho_{\mathrm{LJ}} \sigma_{12\text{-}6}^3}{3} \left(\frac{15}{8}\right)^{1/2} \epsilon_{12\text{-}6}, \tag{2.19}$$

$$\sigma_{9\text{-}3} = \left(\frac{2}{15}\right)^{1/6} \sigma_{12\text{-}6}, \tag{2.20}$$

the total potential energy can be simply rewritten as:

$$U_{9\text{-}3} = 4\epsilon_{9\text{-}3} \left[\left(\frac{\sigma_{9\text{-}3}}{z}\right)^9 - \left(\frac{\sigma_{9\text{-}3}}{z}\right)^3 \right]. \tag{2.21}$$

2.2.2 Rugous potential

We propose a linear combination of a surface made of Lennard-Jones particles and a Lennard-Jones 9-3 potential to confine water between rugous walls. The proposed confining potential is:

$$U_{\mathrm{r}}(x, y, z) = U_{9\text{-}3}(z) + \alpha\{U_{12\text{-}6}(x, y, z - l_{z_1}) - [U_{9\text{-}3}(z) - U_{9\text{-}3}(z - l_{z_2})]\}. \tag{2.22}$$

On the right side of Eq. 2.22 we add a second term of a layer made of Lennard Jones particles located at $z = l_{z_1}$, which introduces roughness into the potential, and remove the integrated piece of matter that represents this layer of Lennard-Jones particles $(U_{9\text{-}3}(z) - U_{9\text{-}3}(z - l_{z_2}))$. l_{z_2} is the distance in z between neighbor layers in the piece of matter made of Lennard-Jones particles that integrates into the Lennard-Jones 9-3 potential. The second term on the right is multiplied by a parameter α which controls the strength of the roughness in the potential. Eq. 2.22 can be rewritten simply:

$$U_{\mathrm{r}}(x, y, z) = (1 - \alpha) U_{9\text{-}3}(z) + \alpha[U_{12\text{-}6}(x, y, z - l_{z_1}) + U_{9\text{-}3}(z - l_{z_2})]. \tag{2.23}$$

In order to obtain l_{z_2}, during the integration of the solid, we consider it to be arranged into a fcc crystallographic configuration, where the surface is oriented into the (111) direction conforming a triangular lattice. Given a triangular lattice parameter a, the neighbor interlayer distance and density are:

$$l_{z_2} = a\sqrt{\frac{2}{3}}, \tag{2.24}$$

$$\rho_{\mathrm{LJ}} = \frac{\sqrt{2}}{a^3}. \tag{2.25}$$

The z position of the layer of Lennard-Jones particles $z = l_{z_1}$ is set to maintain the z position of the minimum of the mean confining potential $\langle U_{\mathrm{r}} \rangle_{xy}$ independent of

α. Taking into account that a layer made of Lennard-Jones particles located at $z = l_{z_1}$ integrates into the Lennard-Jones 10-4 potential, $\langle U_{12\text{-}6}(x, y, z - l_{z_1})\rangle_{xy} = U_{10\text{-}4}(z - l_{z_1})$, given by:

$$U_{10\text{-}4}(z) = 4\epsilon_{10\text{-}4}\left[\left(\frac{\sigma_{10\text{-}4}}{z}\right)^{10} - \left(\frac{\sigma_{10\text{-}4}}{z}\right)^{4}\right], \tag{2.26}$$

where,

$$\epsilon_{10\text{-}4} = \pi\rho_{\mathrm{LJ}}\sigma_{12\text{-}6}^2\left(\frac{25}{32}\right)^{1/3}\epsilon_{12\text{-}6}, \tag{2.27}$$

$$\sigma_{10\text{-}4} = \left(\frac{2}{5}\right)^{1/6}\sigma_{12\text{-}6}, \tag{2.28}$$

and, ρ_{LJ} in this case, is the surface density. The total mean confining potential is:

$$\langle U_{\mathrm{r}}(x, y, z)\rangle_{xy} = (1 - \alpha)U_{9\text{-}3}(z) + \alpha\left[U_{10\text{-}4}(z - l_{z_1}) + U_{9\text{-}3}(z - l_{z_2})\right]. \tag{2.29}$$

We then find the coordinate $z = z_0$ at which the first term on the right of Eq. 2.29 has its minimum,

$$\frac{dU_{9\text{-}3}(z)}{dz}\Big|_{z_0} = 0, \tag{2.30}$$

and we obtain l_{z_1} by imposing the second term on the right of Eq. 2.29 to have its minimum at the same coordinate z_0:

$$\frac{d\left[U_{10\text{-}4}(z - l_{z_1}) + U_{9\text{-}3}(z - l_{z_2})\right]}{dz}\Big|_{z_0} = 0. \tag{2.31}$$

Thereby, the minimum of the total mean potential is at z_0 and is independent from α.

In the calculations, independently of the chosen type of wall, planar or rugous, the distance between the origins of the confining potentials is set to $L_z = 8$ Å, and the parameters are chosen to mimic the interaction of water with solid paraffin [23]: $\epsilon_{9\text{-}3} = 1.25$ kJ/mole and $\sigma_{9\text{-}3} = 0.25$ nm. One of the problems of using such confining potentials is that the z dimension of the system is no longer well-defined. Many important magnitudes, such as volume, density, and pressure depend on this distance. To solve this problem, we employ an effective $L_z^{'}$ defined as in [24]:

$$L_z^{'} = L_z - \frac{\sigma_{9\text{-}3} + \sigma_{\mathrm{O}}}{2}, \tag{2.32}$$

which gives $L_z^{'} = 0.515$ nm.

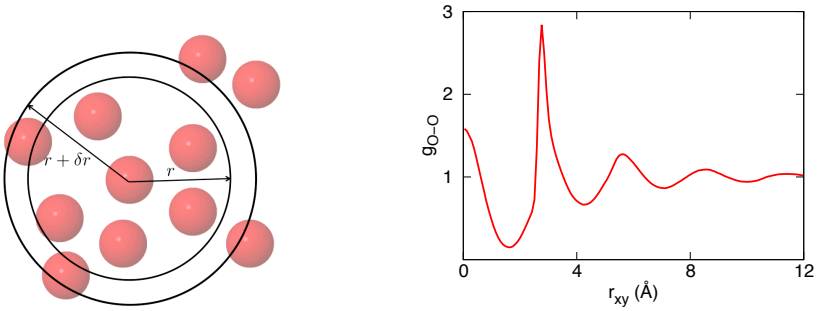

(a) (b)

Figure 2.3: (a) To calculate the RDF, the number of particles between the radii r and $r + \delta r$ are counted. (b) An oxygen-oxygen RDF of bilayer liquid water.

2.3 Data analysis

Here we describe the different functions employed in order to obtain structural and dynamical information of water from the data produced during the simulations.

2.3.1 RDF

The radial distribution function (RDF) gives the distribution of density $\rho(r)$ with respect to the distance around a referential particle normalised with the mean density ρ_m:

$$g(r) = \frac{\rho(r)}{\rho_m}. \tag{2.33}$$

In our case, we calculate the RDF in the xy plane. Considering the function $N(r)$ that gives the number of particles within a circular plate of radius r and height L_z around a referential particle (see Fig. 2.3), the density variation is given by:

$$\rho(r) = \lim_{\delta r \to 0} \frac{N(r + \delta r) - N(r)}{L_z \pi [(r + \delta r)^2 - r^2]}. \tag{2.34}$$

The mean density is simply the number of particles within the cell N_{cell} divided by the volume of the cell $V_{\text{cell}} = L_z A_{\text{cell}}$. Therefore, the RDF is:

$$g(r) = \frac{A_{\text{cell}}}{\pi N_{\text{cell}}} \lim_{\delta r \to 0} \frac{N(r + \delta r) - N(r)}{2r\delta r - \delta r^2} \tag{2.35}$$

Finally, the function is averaged over the number of particles and time steps:

$$\langle g(r)\rangle = \frac{A_{\text{cell}}}{\pi N_{\text{cell}}^2 t_{\text{steps}}} \lim_{\delta r\to 0} \sum_{t=1}^{t_{\text{steps}}} \sum_{i=1}^{N_{\text{cell}}} \frac{\left[N(r+\delta r) - N(r)\right]_{i,t}}{2r\delta r - \delta r^2} \tag{2.36}$$

Fig. 2.3 (b) shows an oxygen-oxygen RDF of bilayer liquid water. The peak at the origin gives the correlation between oxygens from different planes exclusively. The peaks at larger r_{xy} indicate the most likely distances at which the first-, second-, and so on neighbors are located.

We also calculate the **2D-RDF** $\langle g_{\text{2D}}(xy)\rangle$, which is analogous to the RDF but takes into account both the xy coordinates of the particles instead of the radial coordinate.

2.3.2 Density Profile

The density profile gives the density distribution of particles along the confining direction (in our case z). Considering the function $N(z)$, which gives the number of particles within a box of dimensions $A_{\text{cell}} \times z$, the density profile is defined as:

$$\rho(z) = \frac{1}{A_{\text{cell}}} \lim_{\delta z\to 0} \frac{N(z+\delta z) - N(z)}{\delta z}. \tag{2.37}$$

And this is averaged over the time steps:

$$\langle \rho(z)\rangle = \frac{1}{A_{\text{cell}} t_{\text{steps}}} \lim_{\delta z\to 0} \sum_{t=1}^{t_{\text{steps}}} \frac{\left[N(z+\delta z) - N(z)\right]_t}{\delta z}. \tag{2.38}$$

2.3.3 Mean Square Displacement

To obtain dynamical information of the simulations, we calculate the mean square displacement (MSD) of the oxygens, defined as:

$$\Delta_{\text{xy}}(t) = [r(t) - r(0)]^2, \tag{2.39}$$

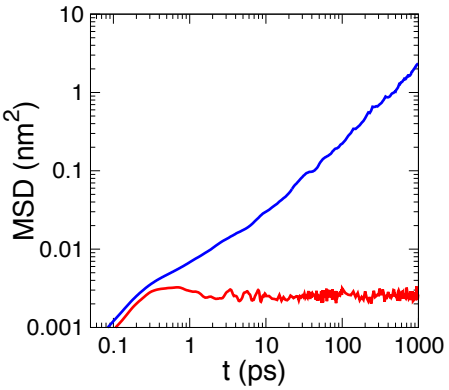

Figure 2.4: Mean square displacement of a two-dimensionally confined liquid (blue) and solid (red). Until $t \sim 0.2$ ps, the particles from both phases are in the ballistic regime and follow $\Delta_{\mathrm{xy}}(t) \propto t^2$. In the diffusive regime, the curve of the solid saturates while the one of the liquid scales linearly with time.

where, $r(t) = [x(t)^2 + y(t)^2]^{1/2}$ is the position of the particle at time t in the xy plane. We then average this function over all the oxygens and different initial time steps:

$$\left\langle \Delta_{\mathrm{xy}}(t) \right\rangle = \frac{1}{N_{\mathrm{cell}} t_{\mathrm{steps}}} \sum_{\tau=0}^{t_{\mathrm{steps}}} \sum_{i=1}^{N_{\mathrm{cell}}} [r_i(t+\tau) - r_i(\tau)]^2. \tag{2.40}$$

Fig. 2.4 shows the MSD for a solid and a liquid. The first part of the curve is the ballistic regime, where the particle is still not influenced by the surrounding particles and $\Delta_{\mathrm{xy}}(t) \propto t^2$. In the second part of the curve, the diffusive regime, the solid saturates into a value, while the liquid follows the Einstein's relation [25] for a two-dimensional system:

$$\Delta_{\mathrm{xy}}(t) = 4Dt, \tag{2.41}$$

where, D is the diffusion constant.

2.3.4 Dipole-dipole autocorrelation function

The dipole-dipole autocorrelation function is the normalized projection of the dipole vector $\mathbf{d}_i$ of a given molecule of water at time t with respect to its initial dipole vector:

$$C_{\mathrm{H_2O}}(t) = \frac{\mathbf{d}(t) \cdot \mathbf{d}(0)}{|d|^2}. \tag{2.42}$$

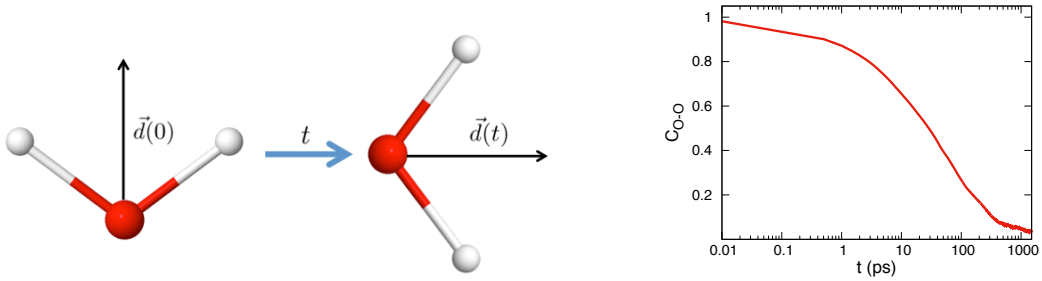

(a) (b)

Figure 2.5: (a) After time t, the orientation of a molecule changes and the projection of the dipole with the initial dipole is smaller than 1. (b) Dipole-dipole autocorrelation function in liquid water. After a characteristic time, the information of the initial molecular orientation is lost.

We average it over different initial time steps and molecules:

$$\langle C_{\mathrm{H_2O}}(t)\rangle = \frac{1}{|d|^2 N_{\mathrm{cell}} t_{\mathrm{steps}}} \sum_{\tau=0}^{t_{\mathrm{steps}}} \sum_{i=1}^{N_{\mathrm{cell}}} \mathbf{d}_i(t+\tau)\cdot\mathbf{d}_i(\tau) \tag{2.43}$$

Fig. 2.5 shows a dipole-dipole autocorrelation function of water molecules in the liquid. At short time scales, the value stays close to 1, while at large time scales, the information of the initial molecular orientations is lost and $\langle C_{\mathrm{H_2O}}(t)\rangle = 0$.

We also calculate the **dipole distribution function** (DDF), which gives the population of molecules with a given polar angle (projected in the xy plane) of the molecular dipoles $\mathbf{d}_i$.

2.3.5 First-neighbor correlation function

The first-neighbor correlation function gives the proportion of initial in-plane nearest-neighbors of any particle that remain after time t. The nearest-neighborhood is defined by a circle of radius r_0 obtained from calculating the distance at which the RDFs show a minimum between the first and second-neighbor peaks. Considering the function $n(t)$ that gives the number of nearest-neighbors that remain after time t, the averaged first-neighbor correlation function is defined as:

$$\langle C_{\mathrm{O\text{-}O}}(t)\rangle = \frac{1}{N_{\mathrm{cell}} t_{\mathrm{steps}}} \sum_{\tau=0}^{t_{\mathrm{steps}}} \sum_{i=1}^{N_{\mathrm{cell}}} \frac{n_i(t+\tau)}{n_i(\tau)} \tag{2.44}$$

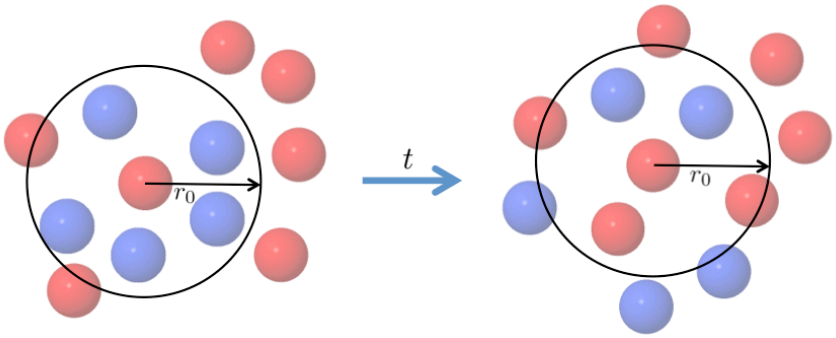

Figure 2.6: To calculate the first-neighbor correlation function, the amount of initial first neighbors (blue particles) that remain in the first-neighborhood after time t are counted.

Fig. 2.6 shows an illustration of how the first-neighbor correlation function is calculated. At t =0, the first-neighbor particles are identified (blue particles in Fig. 2.6) and counted $n(0)$. Then, those remaining in the first-neighborhood at time t are counted $n(t)$.

References

[1] H. J. Berendsen, J. V. Postma, W. F. vanGunsteren, A. Dinola, and J. Haak, (1984) *J. Chem. Phys.* **81(8)**, 3684–3690.

[2] W. G. Hoover, (1985) *Phys. Rev. A* **31(3)**, 1695.

[3] D. Frenkel and B. Smit, (2001) Understanding molecular simulation: from algorithms to applications, volume **1**, Academic press, .

[4] W. Shinoda, M. Shiga, and M. Mikami, (2004) *Phys. Rev. B* **69(13)**, 134103.

[5] G. J. Martyna, D. J. Tobias, and M. L. Klein, (1994) *J. Chem. Phys.* **101(5)**, 4177–4189.

[6] M. Parrinello and A. Rahman, (1981) *J. Appl. Phys.* **52(12)**, 7182–7190.

[7] M. Tuckerman, B. J. Berne, and G. J. Martyna, (1992) *J. Chem. Phys.* **97(3)**, 1990–2001.

[8] M. E. Tuckerman, J. Alejandre, R. López-Rendón, A. L. Jochim, and G. J. Martyna, (2006) *J. Phys. A* **39(19)**, 5629.

[9] J. L. Abascal and C. Vega, (2005) *J. Chem. Phys.* **123(23)**, 234505.

[10] R. W.Hockney and J. W. Eastwood, (1988) Computer simulation using particles, crc Press, .

[11] J.-P. Ryckaert, G. Ciccotti, and H. J. Berendsen, (1977) *J. Comput. Phys.* **23(3)**, 327–341.

[12] S. Plimpton, (1995) *J. Comput. Phys.* **117(1)**, 1–19.

[13] P. Hohenberg and W. Kohn, (1964) *Phys. Rev.* **136(3B)**, B864.

[14] W. Kohn and L. J. Sham, (1965) *Phys. Rev.* **140(4A)**, A1133.

[15] J. M. Soler, E. Artacho, J. D. Gale, A. García, J. Junquera, P. Ordejón, and D. Sánchez-Portal, (2002) *J. Phys. Condens. Matter* **14(11)**, 2745.

[16] N. Troullier and J. L. Martins, (1991) *Phys. Rev. B* **43(3)**, 1993.

[17] J. Junquera, Ó. Paz, D. Sánchez-Portal, and E. Artacho, (2001) *Phys. Rev. B* **64(23)**, 235111.

[18] E. Anglada, J. M. Soler, J. Junquera, and E. Artacho, (2002) *Phys. Rev. B* **66(20)**, 205101.

[19] F. Corsetti, M. Fernández-Serra, J. M. Soler, and E. Artacho, (2013) *J. Phys. Condens. Matter* **25(43)**, 435504.

[20] M. Dion, H. Rydberg, E. Schöder, D. C. Langreth, and B. I. Lundqvist, (2004) *Phys. Rev. Lett.* **92** 246401 .

[21] J. P. Perdew, K. Burke, and M. Ernzerhof, (1996) *Phys. Rev. Lett.* **77** 3865-3868 (1996).

[22] F. Corsetti, E. Artacho, J. M. Soler, S. S. Alexandre, and M.-V. Fernández-Serra, (2013) *J. Chem. Phys.* **139(19)**, 194502.

[23] C.-Y. Lee, J. A. McCammon, and P. Rossky, (1984) *J. Chem. Phys.* **80(9)**, 4448–4455.

[24] P. Kumar, S. V. Buldyrev, F. W. Starr, N. Giovambattista, and H. E. Stanley, (2005) *Phys. Rev. E* **72(5)**, 051503.

[25] J.-P. Hansen and I. R. McDonald, (1990) Theory of simple liquids, Elsevier, .

Chapter 3

Planar confinement: ices

Most of the computational studies agree with the existence of a stable monolayer square ice phase [1–4] observed in the experimental study by Algara *et al.* [5]. However, for the bilayer and trilayer cases, the majority obtain different types of structure as the most stable ones. Han *et al.* [6] observed by classical molecular dynamics simulations using the TIP5P force-field model [7] that nanoconfined bilayer water can freeze by two types of phase transitions depending on its density: a first-order phase transition into honeycomb ice at low densities and a continuous phase transition into rhombic ice at high densities. A recent work by Corsetti *et al.* [8] based on density-functional theory, however, distinguishes two different stable bilayer ices at high densities: a proton-ordered rhombic phase for low temperatures and a proton-disordered triangular phase for high temperatures.

In this chapter, the behavior of bilayer ice and its phase transitions under a planar confinement is analyzed. The employed Lennard-Jones 9-3 potential mimics the interaction of water with solid paraffin [9]: $\epsilon = 1.25$ kJ/mole and $\sigma = 0.25$ nm. The distance between the confining walls is set to 8 Å, ensuring a bilayer structure.

During the first 60 ns of the MD we adopt the NVT ensemble and use the Berendsen thermostat to control the temperature of the system. Then, the NVE is used for 2 ns and the data are collected. The size of the square cell is set to (34.90×34.90) Å^2 dimensions is fixed, and the number of molecules ranges from 196 to 314 such that different densities are sampled.

Figure 3.1 shows a summary of the calculations carried out, together with the

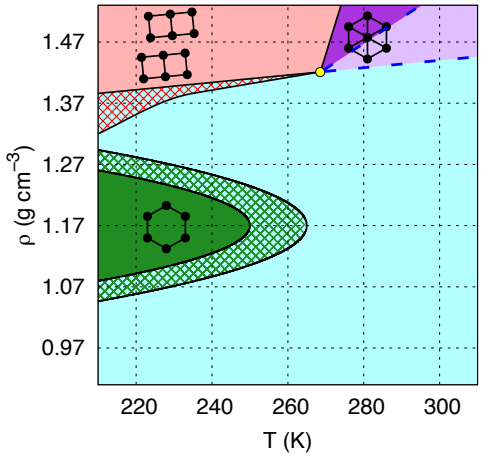

Figure 3.1: Summary of calculations and phase diagram constructed from the results. The density is defined as in Ref. [6]. The crossing points of the thin dashed grid are the points on the phase diagram sampled by MD. In the areas filled by a crosshatch we observe the coexistence of both liquid and solid phases, consistent with having a first-order phase transition in an NVT ensemble. The black lines that delimit the low temperature solid phases represent the first-order transition lines, while the blue dashed lines at high temperatures delimit the continuous phase transition lines among the liquid, hexatic and triangular ice solid phases (described in Chapter 4). These transition lines were drawn semi quantitatively from the results obtained at the sampled points. The connection point that joins the first-order and continuous phase transition lines is located at $\left(270 \pm 10 \text{ K}, 1.42 \pm 0.05 \text{ g cm}^{-3}\right)$.

phase diagram that is constructed from the results. At each point on the density-temperature phase diagram we use four different indicators to assign a phase: the oxygen-oxygen radial distribution function (RDF); the diffusion of the oxygens; and the mean positions of the oxygens that are in the xy plane, while the density profile is along the confining direction. We distinguish the liquid phase (blue), and three different crystalline phases: the hexagonal (green area), square-tubes (red area), and triangular ices (dark-purple). At high densities and temperatures, we also distinguish the hexatic phase (light purple area) from the triangular ice phase, using several indicators which we shall describe in detail in Chapter 4. In the areas filled by a crosshatch we observe the coexistence of both liquid and solid phases, consistent with having a first-order phase transition in an NVT ensemble. Our phase diagram can be directly compared with the one obtained by Han *et al.* [6] with the TIP5P model. One clear difference is that the present results are shifted towards lower temperatures (ΔT $\sim$ 40 K), which is consistent with the fact that TIP5P tends to be more structured than TIP4P/2005 [10].

3.1 Ices

Around $\rho = 1.17$ g cm^{-3}, corresponding to four atomic layers of (001) Ih ice, we observe the existence of **honeycomb ice** at low temperatures, in agreement with previous results [6]. One layer of honeycomb ice results from the squashing of two (001) atomic planes of Ih ice into one layer. Fig. 3.2 shows the structure of the honeycomb ice: the oxygens are arranged into a bilayer honeycomb lattice in a AA stacking and each of them has four hydrogen bonds, a vertical one and another three in the xy plane. The averaged positions of the oxygens and hydrogens show that the hydrogen bonds remain fixed during the simulation.

Fig. 3.2 (c) and (d) show the RDF and density profile of the oxygens in the honeycomb lattice, respectively. The large peak at the origin of the RDF is a signature of the AA stacking, and the location of second-neighbor peak characteristic of this ice is at $r_{\rm h} = \sqrt{3}a = 4.81$ Å, where $a = 2.76$ Å is the first-neighbor distance. The density profile here clearly shows the formation of two oxygen layers.

At high densities, instead of one rhombic phase, as in [6], two different solid phases are observed. The ice at lower temperatures is the **square-tubes ice**: a proton-ordered rhombic ice, that is characterized by the formation of square-shape tubes with fixed position of both the oxygens and the hydrogens, and no bonding between the tubes. Fig. 3.3 shows a snapshot of the simulation box and the averaged positions of the oxygens and hydrogens. Each oxygen shares one vertical and three in-plane hydrogen bonds with its four first-neighbors. The large peak at the origin of the oxygen-oxygen RDF (Fig. 3.3) is consistent with the AA stacking observed in the instantaneous snapshot. The location of the second-neighbor peak is at $r_{\rm s} = 3.95$ Å.

At high densities and high temperatures (dark-purple area of the phase diagram), any instantaneous snapshot of the simulation box (Fig. 3.4 (a)) together with the low value of the diffusion constant $D \sim 10^{-9}$ cm^2 s^{-1} seems to confirm the observation of the amorphous ice previously reported [11]. We observe that the H-bonding network is constantly rearranged during the simulation according to the instantaneous location of the first-neighbors. When the positions of the oxygens and hydrogens are averaged during 1 ns (Fig. 3.4 (b)), a clear oxygen triangular lattice emerges. This result confirms that the oxygens are arranged into a crystalline phase, the **triangular ice**. A remarkable difference of the triangular ice with respect to the hexagonal and square-tubes ices is that the hydrogen bonds are no-longer fixed, as shown by the averaged positions of

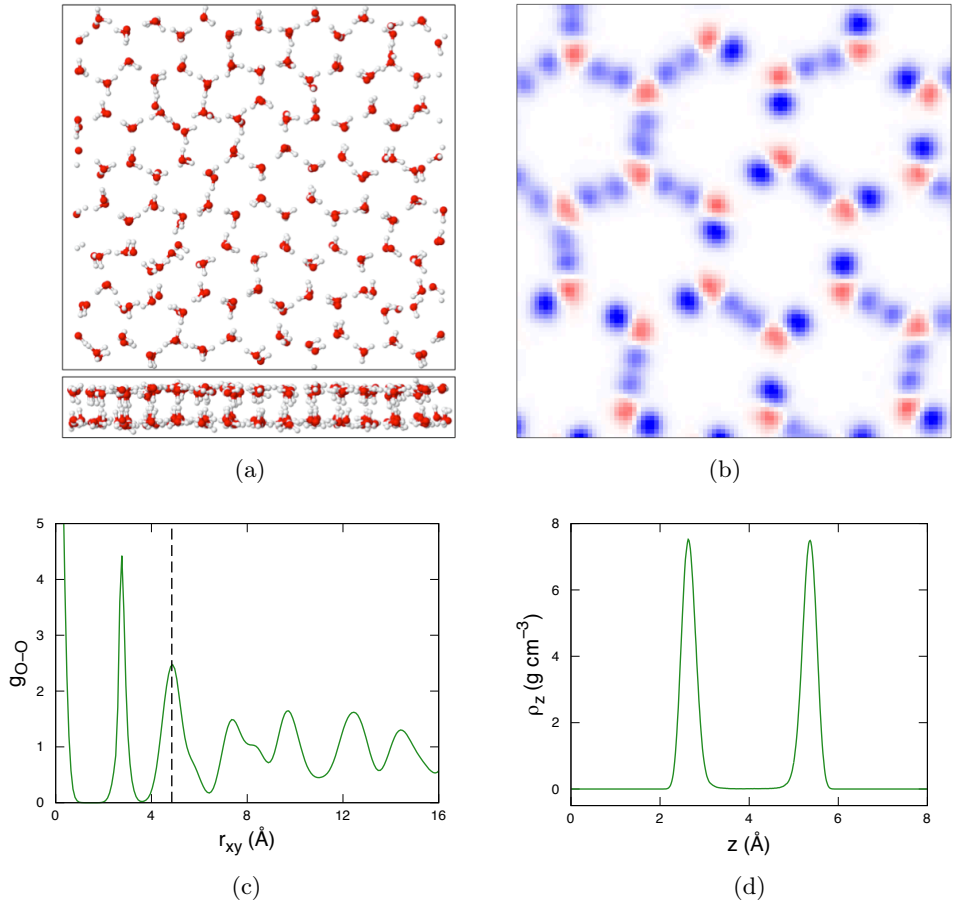

Figure 3.2: Structure of the honeycomb ice obtained at $T = 240$ K, and $\rho = 1.17$ g cm^{-3}. (a) Instantaneous snapshot of the simulation box showing the oxygens (red) and hydrogens (white). (b) Averaged positions of the oxygens (red) and hydrogens (blue) during 1 ns in a window of dimensions (15×15) Å^2 within the cell. (c) Oxygen-oxygen RDF. The vertical dashed line highlights the location of the second-neighbor peak. (d) Density profile of the oxygens.

the hydrogens. Although the vertical hydrogen bond responsible for the AA stacking remains fixed during the simulation, the other three hydrogen bonds fluctuate around the six in-plane first-neighbors during the simulation. The oxygen-oxygen RDF (Fig. 3.4) confirms the AA stacking of the oxygens and shows the location of the characteristic second-neighbor distance $r_t = 2a = 5.56$ Å. It is important to note that the peak at $r_{xy} = \sqrt{3}a$ is also present for the triangular phase. However, as a result of the oxygen lattice vibrations, this peak is broaden out and it is no longer distinguishable.

The apparent differences between the ice phases presented in this work using the TIP4P/2005 model, and by Han *et al.* [6] and Bai and Zeng [11] using the TIP5P

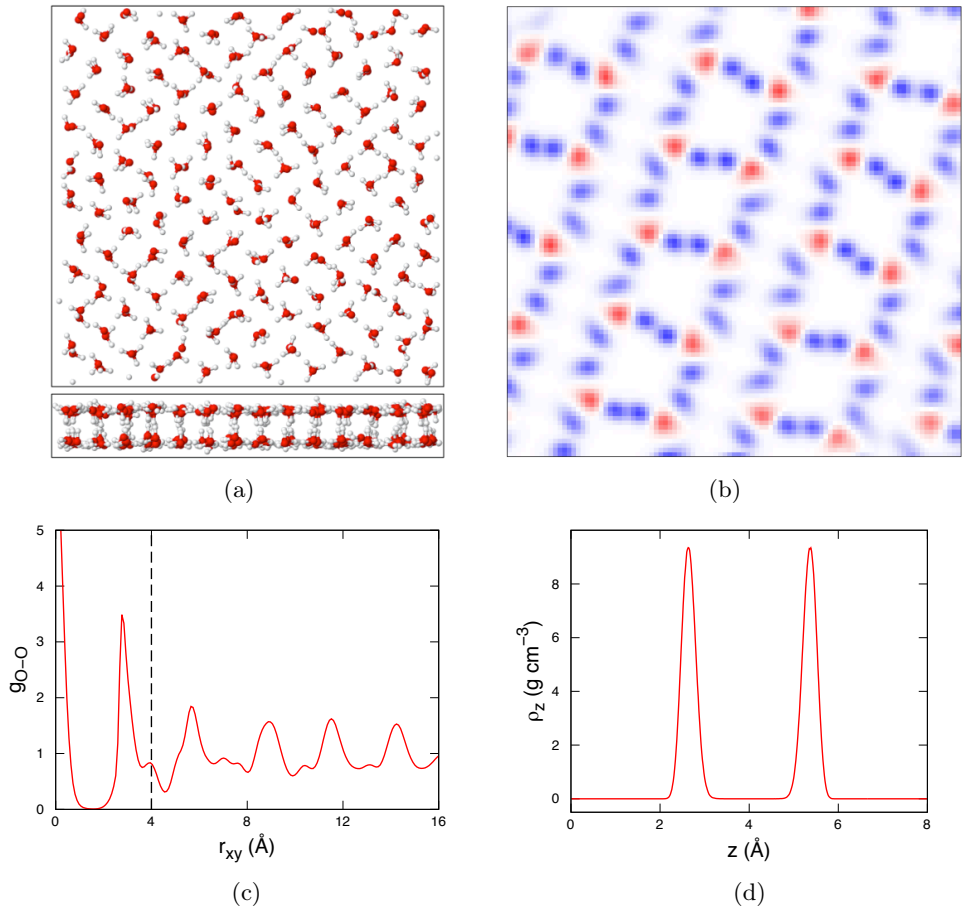

Figure 3.3: Structure of the square-tubes ice. (a) Snapshot of the simulation box showing the oxygens (red) and hydrogens (white). (b) Averaged positions of the oxygens (red) and hydrogens (blue) during 1 ns. (c) Oxygen-oxygen RDF. The vertical dashed line highlights the location of the second-neighbor peak. (d) Density profile of the oxygens.

model, could be attributed to the different force fields used. However, closer inspection reveals striking similarities between the disordered triangular phase described here, the high-density rhombic phase described by Han *et al.* [6], and the high-density amorphous phase described by Bai and Zeng [11]. The confusion stems from the fact that individual snapshots appear quasi-amorphous due to the fluctuating distortions on the lattice caused by the proton disorder [8]; it is also difficult to establish the symmetry of the lattice for the same reason. Nevertheless, the snapshots and RDFs shown in these previous studies strongly suggest that the same phase is observed in all these studies. This, together with the good agreement with density-functional theory [8], supports the findings of this work independent of the particular force-field used.

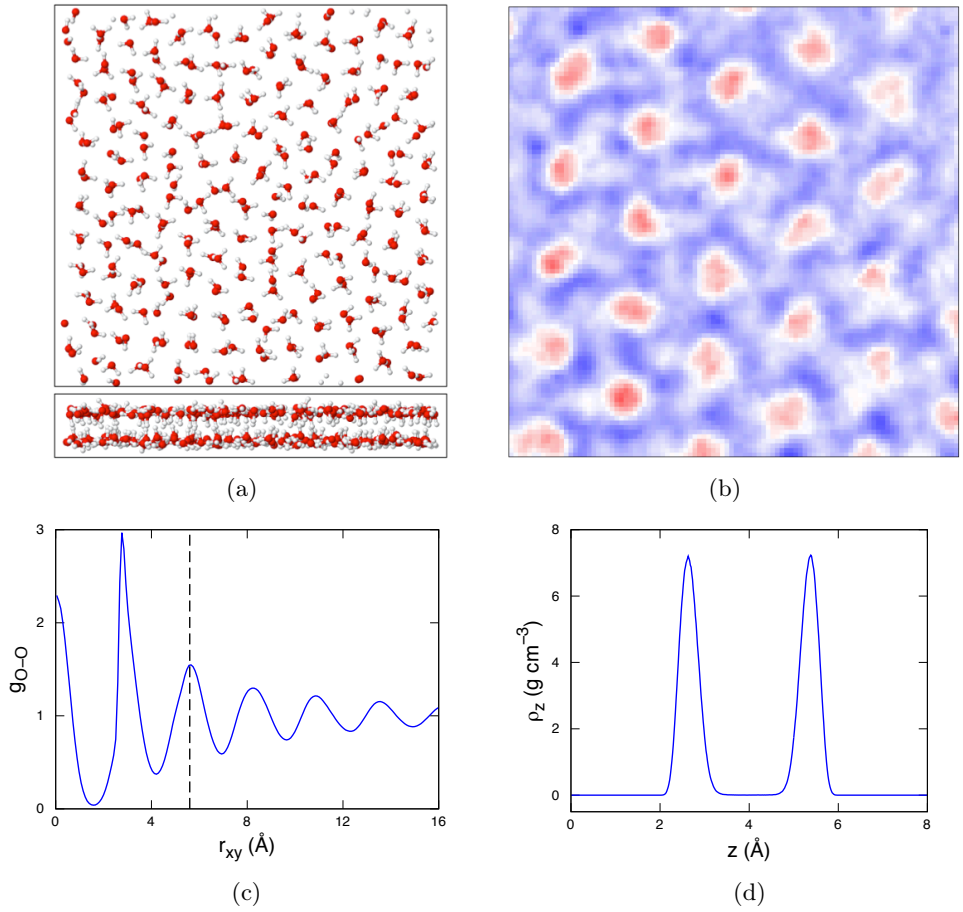

Figure 3.4: Structure of the triangular ice. (a) Instantaneous snapshot of the simulation box showing the oxygens (red) and hydrogens (white). (b) Averaged positions of the oxygens (red) and hydrogens (blue) during 1 ns. (c) Oxygen-oxygen RDF. The vertical dashed line highlights the position of the second-neighbor peak. (d) Density profile of oxygens.

3.2 Phase transition

The fluctuating hydrogen bonds suggest a large configurational entropy and the possibility of an order-disorder transition between the triangular and square-tubes ices. A previous work based on *ab initio* random structure search calculations estimated a configurational entropy of $0.8 \pm 0.1\ k_B$ for the triangular ice by Pauling estimation [8]. We analyze the phase transition between these two ices by calculating the internal energy of the system starting from a higher-temperature configuration and cooling in steps of 5 K. Each step is carried out by reequilibrating the system with the Berendsen thermostat for 5 ns, and then collecting NVE statistics for 100 ps. The reverse heating process is

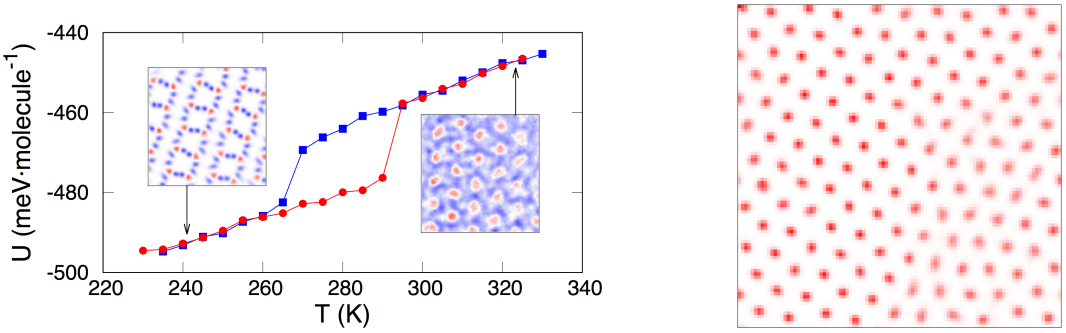

(a) (b)

Figure 3.5: (a) Potential energy per molecule in the heating (red) and cooling (blue) processes as a function of the temperature. The insets show the averaged positions of the oxygens (red) and hydrogens (blue) for the two solids involved in the phase transition: the square-tubes ice at low temperatures, and the triangular ice at high temperatures. (b) Averaged position of the oxygens (red) at $T = 265$ K and $\rho = 1.47$ g cm^{-3}. The coexistence of square-tubes ice (top left) and triangular ice (bottom right) can be clearly observed.

also performed independently. The two processes are shown in Fig. 3.5(a).

The hysteresis loop in Fig. 3.5(a), together with the phase coexistence in a constant volume ensemble (Fig. 3.5(b)) clearly indicate that the phase transition connecting the square-tubes ice and the triangular ice is first-order, and it is estimated to occur at $T_c \simeq 280 \pm 15$ K. As for the square-tubes ice the positions of the oxygens and hydrogens are fixed, we can estimate the configurational entropy of the triangular ice by equating the gain in internal energy at the transition (assuming a similar vibrational contribution for both phases). Since the NVE ensemble is employed, $\Delta S = \Delta U/T_c \simeq 0.7 \pm 0.1\ k_B$. This result is in a good agreement with the previous estimation by Fabiano *et al.* [8], and it is almost twice the value of the residual entropy for bulk ice, $S/N \simeq 0.4\ k_B$.

To verify the obtained value of the configurational entropy, we carry out additional calculations in the $NP_{xy}T$ ensemble. In this case, the difference in entropy is given by the difference of enthalpy at the transition temperature: $\Delta S = \Delta H/T_c$. We carry out several independent calculations at different temperatures around 280 K at $P_{xy} = 2.23$ GPa and calculate the enthalpy for each temperature. We observe a discontinuity $T_c = 272 \pm 2$ K related with the phase transition between both ices. The estimated configurational entropy is $\Delta S \simeq 0.72 \pm 0.05\ k_B$, which is in good agreement with the previous estimation.

The large difference in configurational entropy can be understood in terms of the

generalization of the ice rules in the triangular ice case. There are two configurational entropy contributors: the hydrogen bond disorder coming from the possibility of any oxygen to make three in plane bonds (the fourth is always vertical) with its six first-neighbors, and the one coming from the location of the hydrogen in a given bond. The square-tubes ice and hexagonal ices only have the latter contribution.

References

[1] R. Zangi, (2004) *J. Phys. Condens. Matter* **16(45)**, S5371.

[2] F. Corsetti, P. Matthews, and E. Artacho, (2016) *Sci. Rep.* **6**

[3] R. Zangi and A. E. Mark, (2003) *Phys. Rev. Lett.* **91(2)**, 025502.

[4] T. Kaneko, J. Bai, K. Yasuoka, A. Mitsutake, and X. C. Zeng, (2014) *J. Chem. Phys.* **140(18)**, 184507.

[5] G. Algara-Siller, O. Lehtinen, F. Wang, R. Nair, U. Kaiser, H. Wu, A. Geim, and I. Grigorieva, (2015) *Nature* **519(7544)**, 443–445.

[6] S. Han,, M. Choi, P. Kumar, and H. E. Stanley, (2010) *Nat. Phys.* **6(9)**, 685–689.

[7] M. W. Mahoney and W. L. Jorgensen, (2000) *J. Chem. Phys.* **112(20)**, 8910–8922.

[8] F. Corsetti, J. Zubeltzu, and E. Artacho, (2016) *Phys. Rev. Lett.* **116(8)**, 085901.

[9] C.-Y. Lee, J. A. McCammon, and P. Rossky, (1984) *J. Chem. Phys.* **80(9)**, 4448–4455.

[10] C.Vega and J. L. Abascal, (2011) *Phys. Chem. Chem. Phys.* **13(44)**, 19663–19688.

[11] J. Bai and X. C. Zeng, (2012) *P. Natl. A. Sci.* **109(52)**, 21240–21245.

Chapter 4

Planar confinement: liquid

In this chapter, we study the properties of the liquid under a planar confinement, and the phase transitions that connect it with the different solids described in the previous chapter. The methods employed in the MD simulations are the ones described in the previous chapter. For the AIMD calculations based on density functional theory, the final configuration obtained from the MD calculations is annealed for 5 ps and then the *NVE* ensemble is used for at least 10 ps by AIMD while data are collected. Due to the larger computational cost of such calculations, we reduce the size of the cell to (23.46×24.47) Å^2, and we sample three different densities with 120, 130, and 140 water molecules.

In Fig. 4.1 we show the phase diagram constructed from the obtained results (already shown in Chapter 3). The three red circles show points of the phase diagram obtained by AIMD calculations and the paths described by the numbered arrows will be useful to understand the results of the remaining part of the chapter.

4.1 Phase transitions

The different indicators used in this work show areas with solid-liquid phase coexistence and large structural and dynamical changes during the phase transitions between the liquid and the honeycomb ice. These results clearly indicate that there is a first order phase transition connecting the liquid with this solid. Fig. 4.2 shows these indicators at three points in the phase diagram that connect the liquid with the honeycomb ice phase.

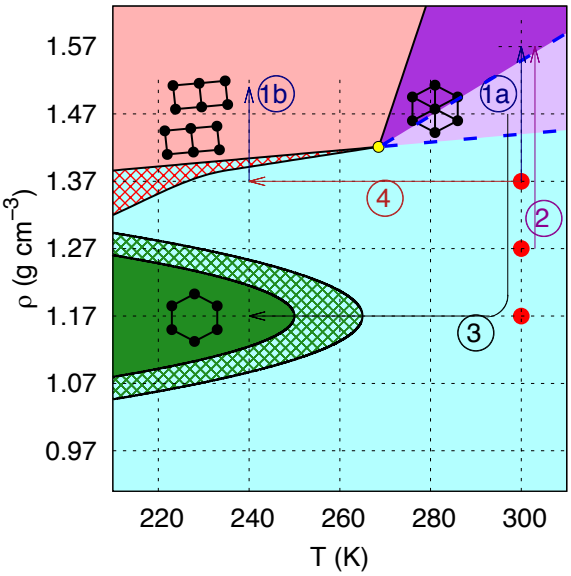

Figure 4.1: Summary of calculations and phase diagram constructed from the results (described in previous chapter). The crossing points of the thin dashed grid are the points on the phase diagram sampled by MD, while the three red circles show the points also calculated by AIMD. The numbered arrows will be useful to understand the results that are shown on the remaining part of the chapter.

The averaged positions of the oxygens at 260 K shows coexistence of both phases, ice and liquid [Fig. 4.2(b)], located between the honeycomb ice [Fig. 4.2(a)] and the liquid [Fig. 4.2(c)]. The large structural and dynamical changes occurring during the phase transition can be observed in the oxygen-oxygen RDFs [Fig. 4.2(d)], the density profiles of the oxygens [Fig 4.2(e)] and the oxygen MSD [Fig 4.2(f)].

In order to investigate the nature of the phase transitions that occur at high densities, we calculate the potential energy of the system as a function of density. For this purpose, we take as the initial state the final configuration obtained in the previous MD simulations at $\rho = 1.37$ g cm^{-3} and $T = 240, 300$ K. We then increase the density by reducing the size of the cell along the xy plane in many steps of $\Delta\rho = 0.01$ g cm^{-3} each. Between each $\Delta\rho$ step, we run 5 ns of re-equilibration with the Berendsen thermostat, followed by 100 ps of NVE statistics. The paths followed on the phase diagram are shown by the two arrows labeled 1a and 1b in Fig. 4.1. The results are shown in Fig. 4.3. At $T = 240$ K and $\rho = 1.43$ g cm^{-3} we observe a change in potential energy of 8.3 meV per molecule that, together with the coexistence area in Fig. 4.1, clearly indicate a first-order phase transition between the liquid and the square tubes ice. Instead, at

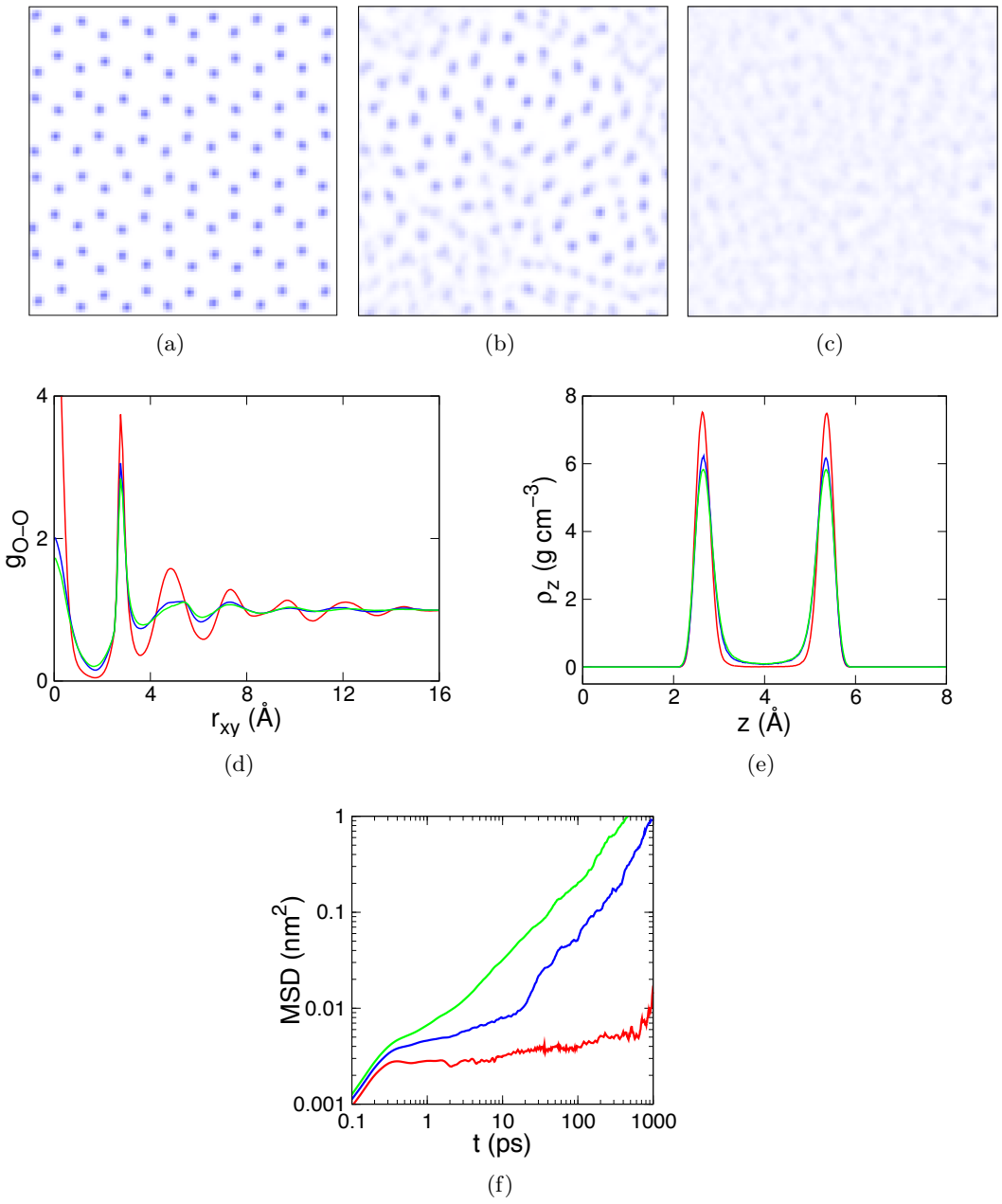

Figure 4.2: [(a)-(c)] Averaged positions of the oxygens (blue) during 100 ps at $\rho = 1.17$ g cm^{-3} and three different temperatures: (a) 240 K, (b) 260 K, and (c) 280 K. (d) In-plane oxygen-oxygen radial distribution function, (e) density profile of the oxygens along the confining direction, and (f) in-plane mean square displacement of the oxygens at $\rho = 1.17$ g cm^{-3} and three different temperatures: 240 K (red), 260 K (blue), and 280 K (green).

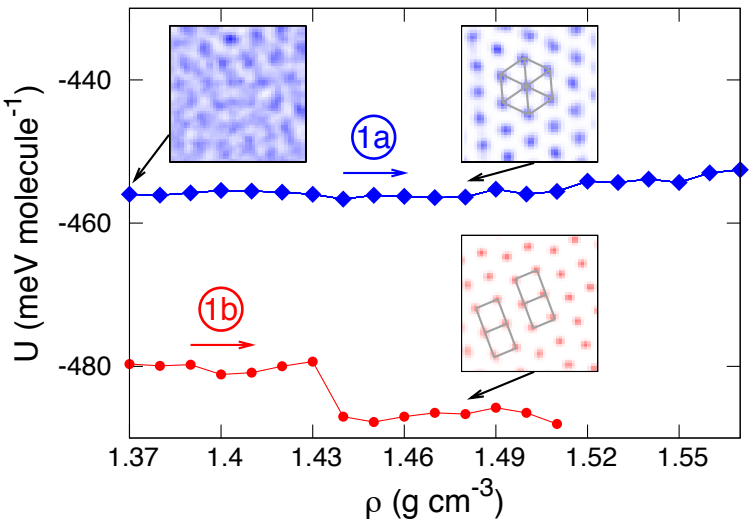

Figure 4.3: Potential energy as a function of density for $T = 240$ K (bottom, red) and $T = 300$ K (top, blue). The 1a and 1b arrows refer to the paths on the phase diagram (see Fig. 4.1). The insets show the averaged positions of the oxygens during 100 ps in a window of dimensions (15×15) Å^2 within the cell. The gray lines within the high-density insets are drawn to illustrate the different structures of each ice.

$T = 300$ K, we do not observe any distinguishable energy jump related with a phase transition, although, there is a clear change in the structure as the density is increased shown by the insets in Fig. 4.3. This is confirmed by the oxygen-oxygen RDFs obtained at $T = 300$ K and $\rho = 1.37$ and 1.47 g cm^{-3} [Fig. 4.4(a)]. The oxygen mean square displacements [Fig. 4.4(b)] also show a change in the dynamical behavior of water during the phase transition: for $\rho = 1.37$ g cm^{-3}, we obtain a diffusivity of 8.26 10^{-6} cm^2 s^{-1}, similar to the diffusivity of confined bilayer water at 300 K in similar conditions [1–3]. However, for $\rho = 1.47$ g cm^{-3}, we obtained a diffusivity of 9.5 10^{-7} cm^2 s^{-1}, which is an intermediate value between the usual diffusivities that confined bilayer water ($\sim 10^{-5}$ cm^2 s^{-1}) and bilayer ice ($\sim 10^{-9}$ cm^2 s^{-1}) show at 300 K in similar conditions [1–3]. These results combined suggest the existence of an intermediate hexatic phase at high temperatures and that the liquid-hexatic and hexatic-triangular ice phase transitions are continuous, which would correspond to the continuous transition reported by Han *et al.* [1].

One of the main characteristics of the triangular ice we observe is that the position of the oxygens are well fixed in closed-packed planes, while the hydrogens show a large disorder, which gives rise to a high configurational entropy calculated in the previous chapter. Therefore, during the phase transition from liquid to triangular ice, we can

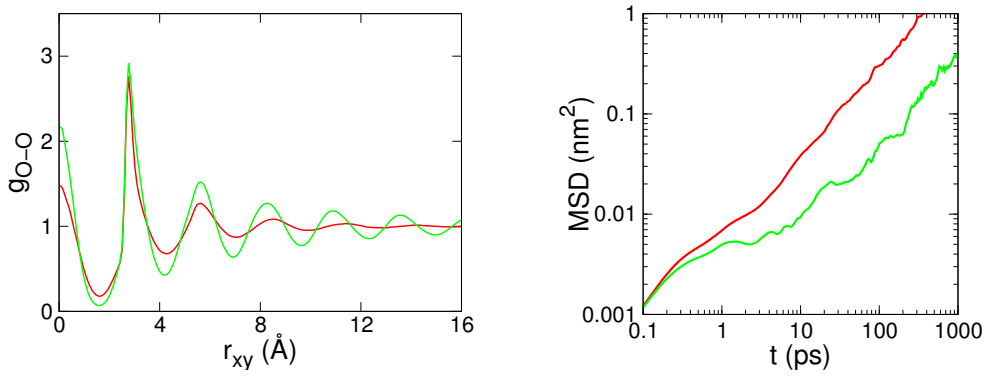

(a) (b)

Figure 4.4: (a) In-plane oxygen-oxygen radial distribution function, and (b) mean square displacement of the oxygens at $T = 300$ K and $\rho = 1.37$ (red), and 1.47 (green) g cm^{-3}

expect a transition for oxygens but no noticeable change for hydrogens. To verify this, we calculate the oxygen-oxygen first-neighbor correlation function ($C_{O\text{-}O}$) and the dipole-dipole autocorrelation function (C_{H_2O}). Within the proposed scenario, after the freezing of the oxygens, $C_{O\text{-}O}$ would remain at a value close to 1, while C_{H_2O} would decay to 0 due to the random motion of the hydrogens.

Fig. 4.5(a) shows the correlation functions obtained at five different densities at $T = 300$ K (see Fig. 4.1, arrow 2): Two of them are in the liquid phase ($\rho = 1.27$, 1.37 g cm^{-3}), another two are in the hexatic phase ($\rho = 1.47$, 1.54 g cm^{-3}), and one is in the triangular ice phase ($\rho = 1.57$ g cm^{-3}). The decay profile for C_{H_2O} decays smoothly to zero for all five densities, showing no appreciable change when crossing the phase transitions; for $C_{O\text{-}O}$, however, there is a noticeable difference between the liquid (fast decay), the hexatic (slow decay), and the triangular ice phase (no decay). This result shows that only the oxygen atoms undergo the phase transitions, while the hydrogens remain in a quasi liquid dynamically disordered state. This behavior is analogous to the one observed in the plastic crystal phases obtained in bulk water at high pressures using the TIP4P/2005 model: The water molecules show large orientational disorder [4, 5].

To prove that the phase at $\rho = 1.47$, 1.54 g cm^{-3}, and $T = 300$ K is hexatic, we analyze the positions of the oxygens during the run: We observe that although there is a clear organization shown in the averaged positions of the oxygens, there is shear motion along the main directions of the triangular lattice (Fig. 4.5(b)). These anisotropic movements of the oxygens, as well as explaining the slow decay of $C_{O\text{-}O}$, suggest that the oxygen lattice has orientational long-range order but no translational

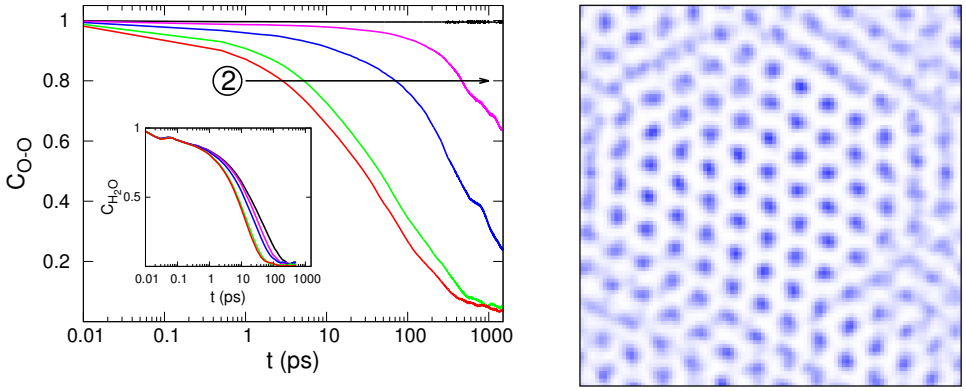

(a) (b)

Figure 4.5: (a) Oxygen-oxygen first-neighbor correlation function (main plot) and dipole-dipole autocorrelation function (inset) as a function of time at $T = 300$ K and five different densities: $\rho = 1.27$ (red), 1.37 (green), 1.47 (blue), 1.54 (pink), and 1.57 (black) g cm^{-3}. The path followed on the phase diagram is the one shown by the arrow labeled 2 in Fig. 4.1. (b) Averaged positions of the oxygens during 100 ps.

long-range order, which is precisely what characterizes the hexatic phase.

The KTHNY theory [6–9] predicts continuous phase transitions for 2D materials in which an intermediate hexatic phase is located between the isotropic liquid and the crystalline solid phases. This theory is based on the creation and disassociation of dislocations [10]. In order to support our observation of the hexatic phase, we search for the presence of dislocations in the oxygen lattice. Fig. 4.6 shows the Voronoi diagram of the oxygens located in the lower layer at three different times. We observe that although most of the diagrams are made of hexagons, there are pentagon-heptagon defect pairs that are characteristic of the presence of dislocations within a triangular lattice [10]. Moreover, these dislocations move along the triangular lattice during the run, explaining the fuzziness of some of the system due to shear shown in Fig. 4.5(b) and the slow decay of $C_{O\text{-}O}$ [Fig. 4.5 (a)] of the hexatic phase. In all the three diagrams we observe the existence of an isolated pentagon-heptagon pair (single dislocation) at different positions. This particular defect is known to be responsible for breaking the translational long-range order within a triangular lattice [10].

Although there is another theory that describes the melting in two dimensional systems via the spontaneous generation of grain boundaries [11], in this case, all the results strongly suggest the existence of an intermediate hexatic phase at high densities and temperatures on the phase diagram (light purple area in Fig. 4.1), and that the

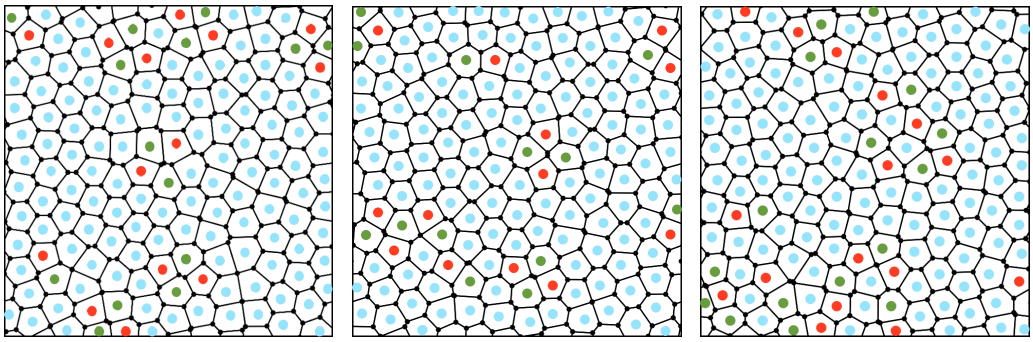

(a) (b) (c)

Figure 4.6: [(a)-(c)] Voronoi diagram of the oxygens located in the lower layer at ρ = 1.47 g cm^{-3}, T = 300 K, and three different times: (a) 0 ps, (b) 1 ps, and (c) 2 ps. Each type of polygon is marked by different colors: red (pentagon), blue (hexagon), and green (heptagon).

phase transition follows the KTHNY theory, as observed for a single layer (continuous phase transition) and double layer (weakly first-order phase transition) of Lennard-Jones particles [12]. The question of whether the observed phase transition is strictly continuous or very weakly first order cannot be answered with certainty from current results and is left for future studies.

Concerning the origin of the difference between the two melting processes (one continuous, one discontinuous), it could be inferred from the previous discussion that it is stemming from the H-disorder kept in the hexatic and triangular phases, as opposed to the square-shape tubes (and honeycomb) phase. Indeed, the thermal delocalization in the hexatic and triangular phases implies both, an effective monoatomic system, giving rise to a 2D close-packing in each layer, and an effective screening of the electrostatic interactions among water molecules.

4.2 Characterization of liquid

After analyzing the different phase transitions, we focus on the characterization of the liquid. Some of the properties of the liquid agree well with previously reported works [2]: The oxygens are organized into two main layers that are bridged by a constant flux of molecules. When the density of the liquid is increased, these two main layers become more pronounced and the flux of molecules is reduced. The diffusivity of the liquid in the xy plane is similar to the one of bulk water ($D \sim 10^{-5}$ cm^2 s^{-1} at T = 300 K).

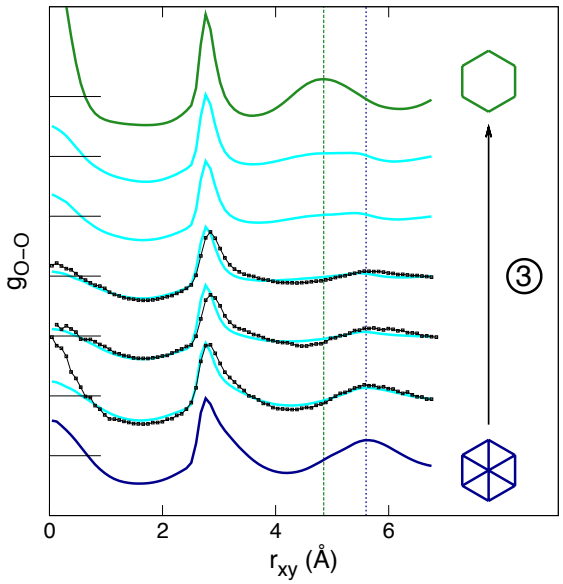

Figure 4.7: Oxygen-oxygen radial distribution functions at different densities and temperatures following the path marked by the arrow labeled 3 in Fig. 4.1. The curves are shifted on the y axis; the value of saturation of each curve is marked by a horizontal finite line. The smooth-line curves correspond to the MD calculations while the line-point curves to the AIMD calculations. The vertical dashed lines highlight the position of the second neighbor peak for the triangular ice (dark blue) and the honeycomb ice (green).

In order to characterize the structure of the liquid, we take as reference the honeycomb and triangular ices (the square tubes ice is a particular state of the triangular ice [13]) and we check if the liquid exhibits the characteristics of either of these two solids. We choose a path within the phase diagram that connects the two phases (see arrow 3 in Fig. 4.1) and we analyze the RDFs at each calculated point along this path. Fig. 4.7 shows the RDFs obtained from MD and AIMD calculations. Although the water obtained from AIMD tends to be more structured than the one obtained by MD, the two are in reasonable agreement for the purposes of this study. One clear difference between the RDF of the honeycomb and triangular phases is the position of the second neighbor peak: For the honeycomb phase it is at $r_{\mathrm{h}} = \sqrt{3}a$, where a is the first neighbor distance, while for the triangular phase it is at $r_{\mathrm{t}} = 2a$ (see Fig. 3.2, and 3.4). Although we observe a continuous shifting of the second neighbor peak from r_{t} towards r_{h} as we get closer to the honeycomb ice RDF in Fig. 4.7, it is very significant how all the RDFs coming from the liquid samples show the characteristic peak of the triangular phase at r_{t}, suggesting that the liquid maintains the local structure of triangular phase.

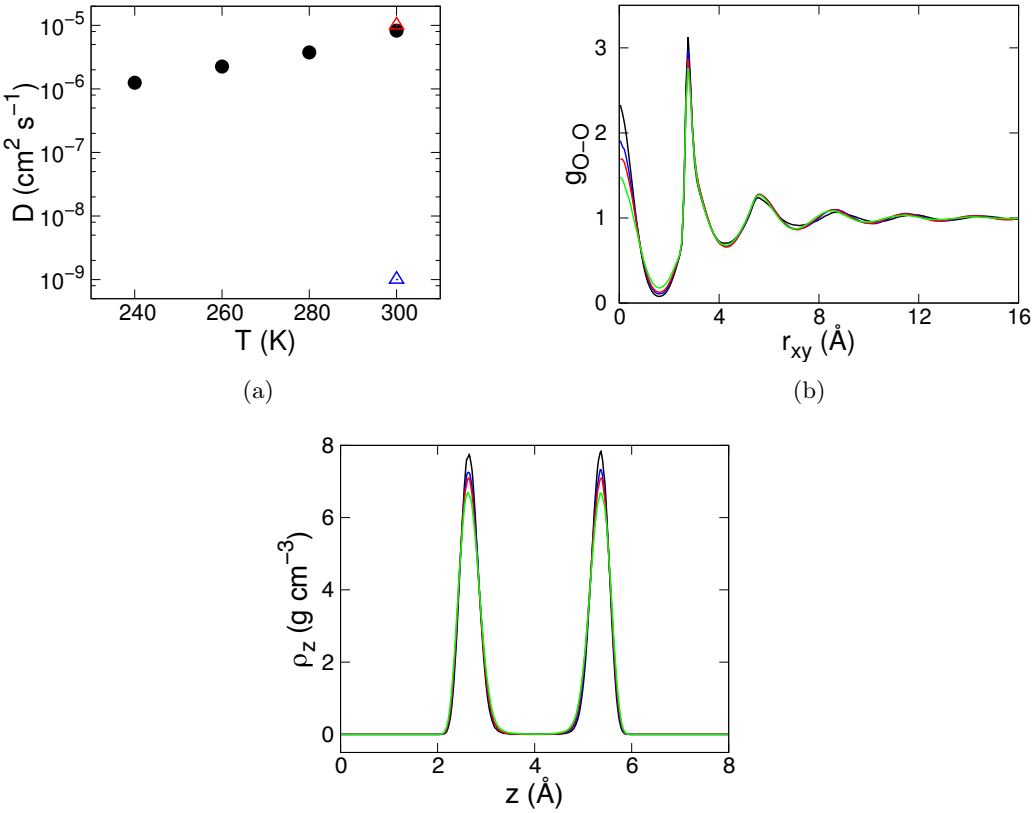

Figure 4.8: (a) In-plane diffusion constant of the oxygens at $\rho = 1.37$ g cm^{-3}. The expected value of the diffusion constant for a confined bilayer water (red triangle) and bilayer ice (blue triangle) are shown for comparison. (b) In-plane oxygen-oxygen radial distribution function, and (c) density profile of the oxygens along the confining direction, both at $\rho = 1.37$ g cm^{-3} and four different temperatures: 240 K (black), 260 K (blue), 280 K (red), and 300 K (green).

The first maximum at $r_{xy} = 0$ measures the correlation between the molecules at the same xy position but in different layers. As all the RDFs in Fig. 4.7 show a pronounced peak at this position, we conclude that there is a strong correlation between the two layers, with a strong tendency for every O in one layer to have another one just across in the other layer. This correlation is increased by increasing the density or decreasing the temperature.

The structural and dynamical analysis of the liquid at $\rho = 1.37$ g cm^{-3} shows that in the xy plane, water behaves like a normal liquid, while along the confining direction it is highly structured. The in-plane oxygen diffusion constants shown in Fig. 4.8(a)

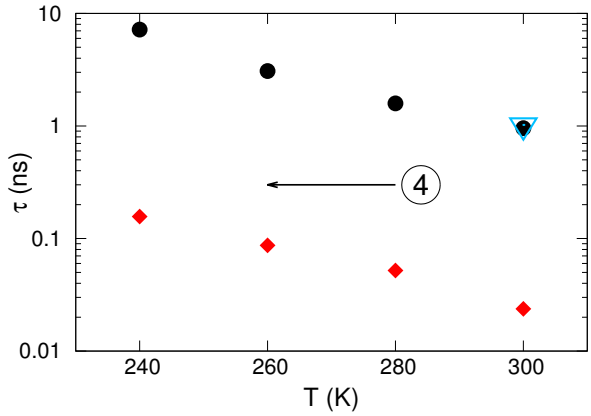

Figure 4.9: Vertical-jump lifetime (τ_z) obtained from MD (circles) and AIMD (triangle) calculations and the in plane-jump lifetime (τ_{xy}, rhonbuses) at $\rho = 1.37$ g cm^{-3} and different temperatures (arrow 4 in Fig. 4.1).

are very similar to the expected value of the diffusion constant for a confined bilayer water ($\sim 10^{-5}$ cm^2 s^{-1}) at 300 K in similar conditions [1–3] and the RDFs show a very similar liquid like structure for the four different temperatures. The oxygen density profiles along the confining direction however, show that the molecules are structured in two main layers with almost no flux between them [Fig. 4.8(c)]. These results show that the high-density liquid maintains many of the characteristics of triangular ice: high interlayer correlation and a local triangular structure of the oxygens, as shown in the RDFs, and a distinct separation between the two layers, as shown in the density profiles (see Fig. 4.8).

In order to verify the large anisotropy of the high density liquid, we estimate the average time (τ_z) that a molecule stays within a layer before jumping to the other layer. To do so, we divide the cell along the confining direction into two equal parts, and we extract the number of jumps that have occurred during the run from one side of the cell to the other. Second, we estimate from the calculated diffusivity D, the time needed by a molecule to jump a distance a within one layer (which coincides with the interlayer distance) using a random walk model: $\tau_{xy} = a^2(4D)^{-1}$. Fig. 4.9 shows these two values at $\rho = 1.37$ g cm^{-3} and different temperatures (following arrow 4 in Fig. 4.1). The values of τ_z obtained from empirical MD and AIMD calculations at T = 300 K are almost identical, supporting the reliability of our calculations. In all cases, τ_z is around 50 times larger than τ_{xy}, which shows that the velocity scale of the diffusion in xy is much larger than in z. These results, together with the high interlayer correlation shown by the RDF, confirm that a molecule remains for an average of 10 ns in one layer

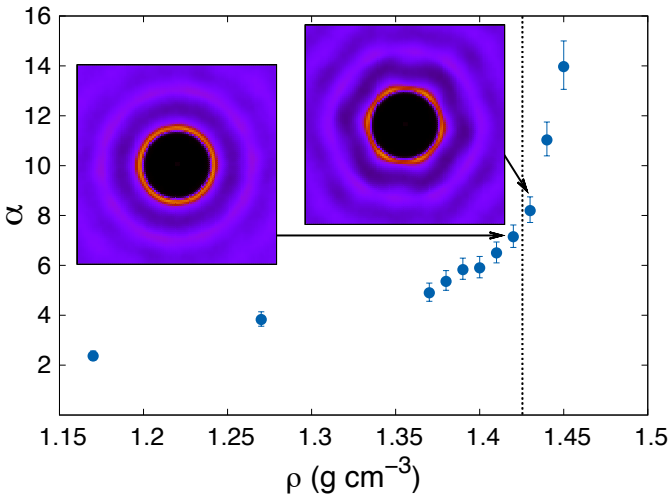

Figure 4.10: Ratio between the characteristic times of $C_{O\text{-}O}$ and C_{H_2O} at $T = 300$ K with respect to density (main plot) and 2D oxygen-oxygen correlation function (insets) at $\rho = 1.42$ (left) and 1.43 g cm^{-3} (right): the brighter the color, the larger the value of the 2D oxygen-oxygen correlation function. The vertical dashed line represents the estimated density in which the liquid-hexatic transition occurs.

before jumping to the other layer, and that its in-layer motion is closely mirrored by a partner molecule in the other layer; in other words, the AA stacking is maintained by the liquid.

Furthermore, the decoupling in the dynamics between O and H that occurs in the hexatic and triangular phases is also clearly observed in the high-density liquid. Fig. 4.10 shows the ratio (α) with respect to density at $T = 300$ K. This ratio is given by $\alpha = C_{O\text{-}O}(\tau_{O\text{-}O})\ C_{H_2O}(\tau_{H_2O})^{-1}$, where the characteristic time τ of each correlation function is obtained from $C(\tau) = 0.5$. The larger the value of α, the larger the decoupling between the dynamics of O and H. We estimate the density at which the liquid-hexatic phase transition occurs by looking at the O-O 2D-RDF (insets in Fig. 4.10), which are analogous to the RDFs but take into account both the x and y coordinates of the oxygens instead of the radial coordinate. The O-O 2D-RDF at $\rho = 1.42$ g cm^{-3} shows a spherically symmetric first-neighbor ring, characteristic of the liquid, while at $\rho = 1.43$ g cm^{-3} it transforms into a hexagon, characteristic of the hexatic phase. Therefore, the phase transition at $T = 300$ K is estimated to occur at $\rho = 1.425$ g cm^{-3}. The important point to note is the behavior of alpha: It increases not only within the hexatic phase, but also from low- to high-density liquid. This means that the decoupling between the dynamics of O and H already occurs within the liquid. This points to a regime constituted by the triangular, hexatic, and liquid phases, in which the complexity of

bilayer water seems to disappear, resulting in what resembles a simple monoatomic fluid.

References

[1] S.Han, M. Choi, P. Kumar, and H. E. Stanley, (2010) *Nat. Phys.* **6(9)**, 685–689.

[2] R. Zangi, (2004) *J. Phys.: Condens. Matter* **16(45)**, S5371.

[3] P. Kumar, S. V. Buldyrev, F. W. Starr, N. Giovambattista, and H. E. Stanley, (2005) *Phys. Rev. E* **72(5)**, 051503.

[4] J. Aragones and C. Vega, (2009) *J. Chem. Phys.* **130(24)**, 244504.

[5] J. Aragones, M. Conde, E. Noya, and C. Vega, (2009) *Phys. Chem. Chem. Phys.* **11(3)**, 543–555.

[6] J. M. Kosterlitz and D. J. Thouless, (1973) *J. Phys. C: Solid State* **6(7)**, 1181.

[7] A. Young, (1979) *Phys. Rev. B* **19(4)**, 1855.

[8] B. Halperin and D. R. Nelson, (1978) *Phys. Rev. Lett.* **41(2)**, 121.

[9] D. R. Nelson and B. Halperin, (1979) *Phys. Rev. B* **19(5)**, 2457.

[10] H. H. vonGrünberg, P. Keim, and G. Maret, (2007).

[11] S. Chui, (1983) *Phys. Rev. B* **28(1)**, 178.

[12] R. Radhakrishnan, K. E. Gubbins, and M. Sliwinska-Bartkowiak, (2002) *Phys. Rev. Lett.* **89(7)**, 076101.

[13] F. Corsetti, J. Zubeltzu, and E. Artacho, (2016) *Phys. Rev. Lett.* **116(8)**, 085901.

Chapter 5

Rugous confinement

In this chapter we smoothly introduce a modulation to the planar potential employed in previous chapters [1,2] confining water two-dimensionally. This has been done before with longer modulation periodicities [3] and to study the ice nucleation on mineral surfaces of relevance for cloud formation [4]. We study the effects produced by the topography of the confining substrate into the liquid, hexatic and solid phases described in the previous chapters [2].

For the confining walls, we propose a model based on a referential Lennard Jones 9-3 potential plus Lennard-Jones explicit particles on its surface, allowing us to smoothly add a roughness into the confining potential and control the lattice parameter and energetic amplitude of the oscillation (see Methods).

For the MD calculations, the timestep is set to 1 fs. Starting from a randomly set configuration of positions and velocities, during the first 60 ns of each MD run we adopt the constant particle number, volume, and temperature ensemble (NVT) and use the Nose-Hoover thermostat in order to control the temperature of the system. Then, 2 ns of dynamics are collected for data analysis. The dimensions of the rectangular cell ($L_x^{\mathrm{MD}} \times L_y^{\mathrm{MD}}$) are different for each lattice parameter in order to keep the periodicity of the cell (see Table 5.1).

For the AIMD calculations, the timestep is set to 0.5 fs. Due to the larger computational cost of such calculations, we reduce the size of the cell. Table 5.1 shows the dimensions of the cell ($L_x^{\mathrm{AIMD}} \times L_y^{\mathrm{AIMD}}$) for each lattice parameter.

The position of the confining potential is set so that the origin of the $U_{9\text{-}3}$ potential

Table 5.1: Values of various simulation parameters as defined in the text, that depend on the chosen lattice parameter.

a (Å)	ρ_{LJ} (Å^{-3})	$\epsilon_{12\text{-}6}$ (kcal/mol)	l_{z_1} (Å)	l_{z_2} (Å)	L_x^{MD} (Å)	L_y^{MD} (Å)	L_x^{AIMD} (Å)	L_y^{AIMD} (Å)
2.5	0.0905	0.0538	-0.446	-2.041	37.5	34.641	22.5	25.98
2.75	0.0680	0.0716	-0.456	-2.245	35.75	33.341	24.75	23.816
3	0.0524	0.0929	-0.464	-2.449	36	36.373	24	25.98
4.78	0.0129	0.3757	-0.487	-3.903	33.46	33.117	23.9	24.838

is at $z = 0$ Å, and its symmetric potential at $z = 8$ Å, as in the previous chapters. From Eq. (2.20) we obtain $\sigma_{12\text{-}6} = 3.498$ Å, which is independent of the lattice parameter. The values of $\epsilon_{12\text{-}6}$ for each lattice parameter obtained from Eq. (2.19) are shown in Table 5.1. Table 5.1 shows the values of the parameters used in the simulations for each lattice parameter.

In order to obtain the density at which $P_{\parallel} = 0$ keeping the lattice parameter constant (and hence, the dimensions of the cell), we carry out MD simulations on the NVT ensemble with all the possible number of particles within a range such that the $P_{\parallel} = 0$ point is known to be crossed. We then choose the N that gives the closest value to $P_{\parallel} = 0$.

We first discuss the results obtained with a triangular lattice parameter that is commensurated with honeycomb two-dimensional ice, and then we consider several values of a in the range of what would be found with realistic confining materials, such as (111) faces of various metals.

5.1 Ideal commensuration

Taking into account that the oxygen-oxygen radial distribution function of honeycomb ice shows an oxygen-oxygen xy first-neighbor distance $r_{\text{O-O}} = 2.76$ Å, we choose a triangular lattice with a lattice parameter $a = \sqrt{3}\ r_{\text{O-O}} = 4.78$ Å. This produces an energy surface where the minima are positioned into a honeycomb lattice with the $r_{\text{O-O}}$ distance between the nearest energy minima. Therefore, *a priori* would be ideal for the establishment of a honeycomb ice monolayer, but it would disfavour the formation of a triangular ice monolayer (one third of the oxygens would have to sit on a maximum of the modulation). We study the structural and dynamical properties of water at different densities, temperatures, and values of α.

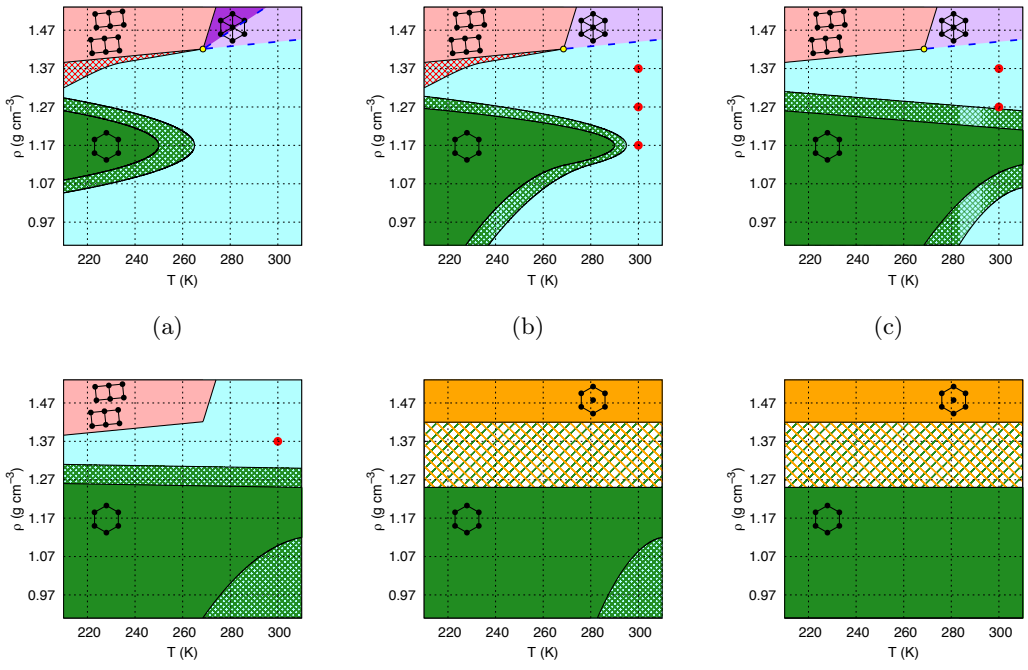

Figure 5.1: Summary of calculations and phase diagram constructed from the results for a lattice parameter $a = 4.78$ Å and $\alpha =$ (a) 0.0, (b) 0.2, (c) 0.4, (d) 0.6, (e) 0.8 y (f) 1.0. The density is defined as in Ref. [1]. The crossing points of the thin dashed grid are the points on the phase diagram sampled by MD, while the six red circles show the points also calculated by AIMD. In the areas filled by a crosshatch we observe the solid-liquid or solid-solid coexistence, consistent with having a first-order phase transition in an NVT ensemble. The black lines represent the first-order transition lines, while the blue dashed lines delimit the continuous phase transition lines among the liquid, hexatic and triangular ice solid phases. These transition lines were drawn semi quantitatively from the results obtained at the sampled points. Blue indicates the liquid phase. The other phases are described in the text.

5.1.1 Phase diagram

Fig. 5.1 shows the temperature-density phase diagrams for the system for $\alpha = 0.0$, 0.2, 0.4, 0.6, 0.8, and 1.0, obtained from the MD calculations. The phases appearing in the diagram for $\alpha = 0.0$ have been previously described in Chapter 3. In order to determine the phase at each calculated point, we have used four different indicators: radial distribution function, oxygen diffusion, and the xy averaged positions of the oxygens, the three of them in the xy plane, and the density profile of oxygen atoms along the confining direction, z. The xy averaged positions of the oxygens are obtained by averaging the xy coordinates of the oxygen atoms over time.

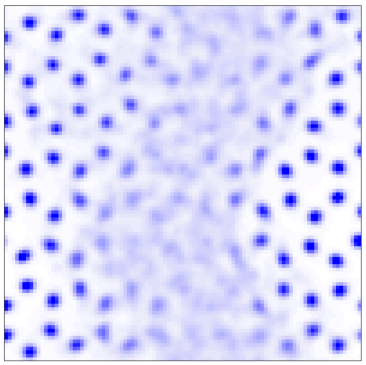

(a)

Figure 5.2: xy averaged positions of oxygen (blue) atoms averaged over 100 ps at $T = 260$ K, $\rho = 1.27$ g cm^{-3}, and $\alpha = 0.4$.

At $\rho \leq 1.27$ g cm^{-3}, the effect of increasing α is the expected one: the corrugation of the potential favours the structure of honeycomb ice and the melting point rapidly increases with α. The observation of phase coexistence of honeycomb ice and liquid at different values of α indicates that the phase transition that connects these two phases keeps being first-order independently from the amplitude of the modulation (see Fig. 5.2).

When $\alpha \leq 0.6$, at $\rho = 1.37$ g cm^{-3} water remains being liquid. At $\rho = 1.47$ g cm^{-3} and low temperatures, the square-tubes ice observed for flat confinement stays stable for $\alpha \leq 0.6$. In this solid, the molecules arrange into tubes and the hydrogen bonds tend to point towards the oxygens from the same tube (see Fig. 5.3). The hexatic phase observed for planar confinement at $\rho = 1.47$ g cm^{-3} and high temperatures demands a deeper analysis to verify whether the orientational long-range order and translational short-range order are kept under the different values of the amplitude of the modulation.

5.1.2 Hexatic phase

As previously mentioned, the triangular modulation with the lattice parameter $a = 4.78$ Å is expected to disfavour highly triangular structured phases, and therefore, the hexatic phase. In addition, one expects that a modulation inserting a lattice of energy maxima and minima along the plane should constrain the appearance and diffusion of the dislocations, responsible for the lack of long-range translational order of the hexatic phase [5–9]. These dislocation appear when the density of the ideal triangular ice (expected to be at $\rho = 1.76$ g cm^{-3}) is decreased.

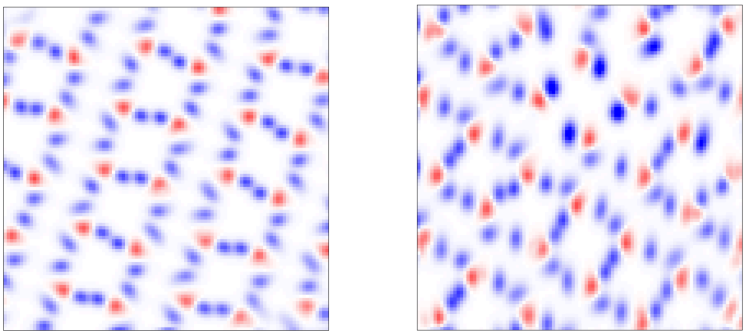

(a) (b)

Figure 5.3: xy averaged positions of oxygen (red) and hydrogen (blue) atoms averaged over 1 ns at $T = 220$ K, $\rho = 1.47$ g cm^{-3}, and $\alpha = 0$ (a), 0.6 (b). All the images were obtained within a window of dimensions (15×15) Å^2 in the simulation cell.

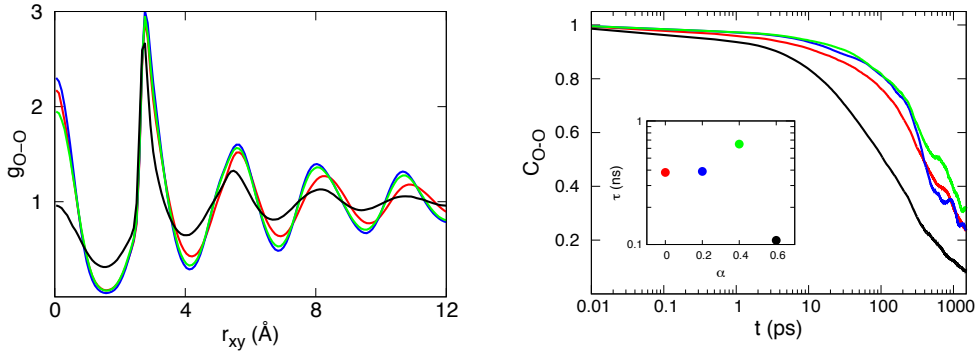

(a) (b)

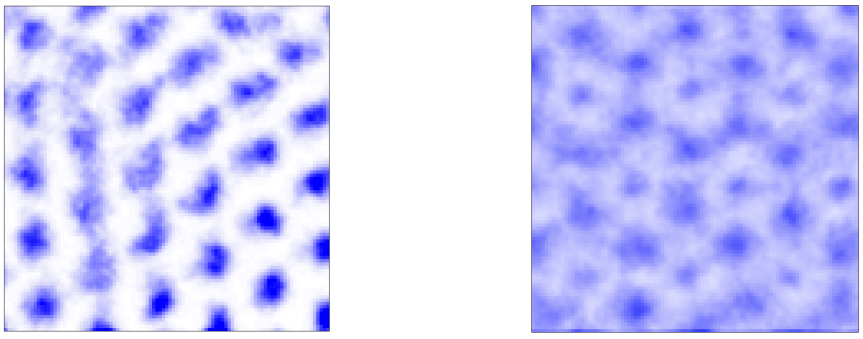

(c) (d)

Figure 5.4: (a) Oxygen-oxygen radial distribution function and (b) oxygen-oxygen first-neighbor correlation function at $T = 300$ K and $\rho = 1.47$ g cm^{-3} for $a = 4.78$ Å and $\alpha = 0$ (red), 0.2 (blue), 0.4 (green), and 0.6 (black). The inset in (a) shows the characteristic time for each curve. (c-d): averaged position of oxygens (blue) during 100 ps at $T = 300$ K, $\rho = 1.47$ g cm^{-3}, and $\alpha = 0.4$ (b), 0.6 (c). The images were obtained by averaging in time, within a window of dimensions (15×15) Å^2 in the simulation cell.

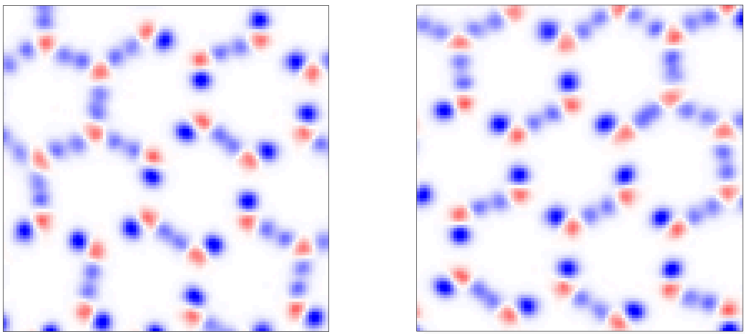

(a) (b)

Figure 5.5: xy averaged positions of oxygen (red) and hydrogen (blue) atoms averaged over 1 ns at $\rho = 1.17$ g cm^{-3}, $T = 240$ K, (a) $\alpha = 0.0$ and (b) and $\alpha = 1.0$. All the images were obtained within a window of dimensions (15×15) Å^2 in the simulation cell.

For the characterization of the hexatic phase, we also calculate the oxygen-oxygen first-neighbor correlation function (C_{OO}). From C_{OO}, we calculate the characteristic time τ of the C_{OO} curve, which is obtained from: $C_{OO}(\tau) = 0.5$. For $\alpha \leq 0.4$, the oxygens arrange themselves into a triangular lattice showing similar structural and dynamical features as the ones observed in the hexatic phase at $\alpha = 0$: similar RDFs [Fig. 5.4 (a)], diffusivities ($D = 6\ 10^{-7}$ cm^{2}s^{-1} at $T = 300$ and $\alpha = 0.4$) and oxygen-oxygen first-neighbor correlation functions [Fig. 5.4 (b)]. We also observe the existence of shear motion along the main directions of the triangular lattice in the oxygen xy averaged positions [Fig. 5.4 (c)]. All these indicators combined suggest that the hexatic phase remains stable for $\alpha \leq 0.4$. At $\alpha = 0.6$, although there is still a clear structuring of the oxygens into a triangular lattice, we do not observe shear motion of oxygens [Fig. 5.4 (d)]. The increase in the diffusivity ($D = 3\ 10^{-6}$ cm^{2}s^{-1}), decrease of the characteristic time of the C_{OO} function in Fig. 5.4 (a), and the less structured RDF [Fig. 5.4 (a)] suggest that the hexatic phase is sufficiently frustrated to be no longer stable under these conditions. Although the triangular structuring is still present in the xy averaged positions of the oxygens, water seems to behave as a dense triangular liquid. Therefore, the indicators employed in this section suggest that the continuous melting washes out for $\alpha \geq 0.6$.

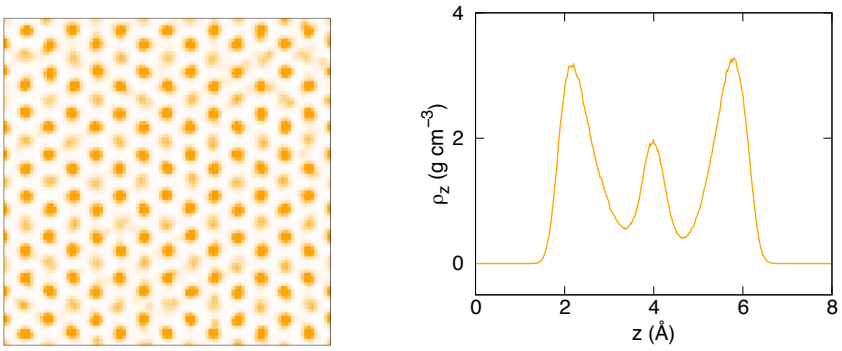

(a) (b)

Figure 5.6: (a) xy averaged positions of the oxygens averaged over 1 ns, and (b) density profile of the oxygens, both at $T = 260$ K, and ρ=1.47 g cm^{-3}. The two exterior oxygen layers are arranged into a bilayer honeycomb lattice in a AA stacking. The oxygens from the middle layer fill the centre of the honeycomb hexagons, coinciding with the xy positions of the Lennard-Jones particles of the confining potential.

5.1.3 Intercalated honeycomb ice

The structural and dynamical properties of the honeycomb ice, square tubes ice, and the triangular phases appearing in Fig. 5.1 have been already well described in previous chapters and α does not affect them significantly (see Fig. 5.3 and 5.5). However, when $\alpha = 0.8$ and 1.0 a different form of ice stabilizes at ρ=1.47 g cm^{-3}, which we call the intercalated honeycomb ice. Fig. 5.6 shows the xy averaged positions of oxygens and the density profile characteristic of this solid. The oxygen atoms arrange themselves into three layers: the two exterior layers conform a AA stacked honeycomb structure favoured by the energy landscape produced by the Lennard-Jones confining particles. The oxygens from the central layer fill the centre of the honeycomb hexagons coinciding with the xy coordinates of the confining Lennard-Jones particles. Between the optimal densities of the honeycomb ice (ρ=1.17 g cm^{-3}), and the intercalated honeycomb ice (ρ=1.47 g cm^{-3}), we observe regions of both phases independently of the temperature (see Fig. 5.7). This is a signature of having a first-order phase transition in a NVT ensemble.

5.1.4 Liquid

The effect of the corrugation on the structure of the liquid is different depending on its density. For densities ranging between $\rho = 0.97{-}1.17$ g cm^{-3}, the liquid rapidly

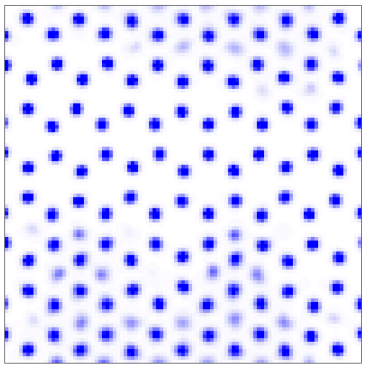

(a)

Figure 5.7: xy averaged positions of oxygen (blue) atoms averaged over 1 ns at $T = 240$ K, $\rho = 1.37$ g cm^{-3}, and $\alpha = 1.0$.

freezes at the highest temperatures considered as α increases, as shown in Fig. 5.1. Before it freezes, however, the liquid does not show appreciable changes on its structure (Fig. 5.8) . At higher densities, the liquid resists to freeze, specially at $\rho = 1.37$ g cm^{-3}, which only freezes after $\alpha = 0.8$. Fig. 5.9 shows the RDFs, and density profiles of liquid water at $T = 300$ K, and $\rho = 1.37$ g cm^{-3} for different values of α. The vertical dashed lines on Fig. 5.9(a) highlight the position of the second neighbor peak of the triangular ice $r_t = 2r_{\text{O-O}} = 5.52$ Å and the honeycomb ice $r_h = \sqrt{3}r_{\text{O-O}} = 4.78$ Å. With no corrugation, the liquid at this density shows structural features on the RDF and density profile characteristic of the triangular ice: high inter-planar correlation (high value on $g_{\text{O-O}}(0)$), a pronounced peak on the RDF at r_t, and two pronounced peaks on the density profile with little flux of molecules between them. When α is applied, the RDFs barely increase their value at r_h, which shows the clear resistance of the liquid to maintain the triangular structure despite the fact that it is disfavoured by the external modulation. The liquid, instead of becoming more honeycomb-like, shows a destructuring effect under the modulation (Fig. 5.9): as α increases, the RDFs show smaller peaks and decrease their value at the origin that measures the inter-layer correlation. The two peaks on the density profile decrease while the flux of molecules between them increases. The destructuring tendency with the external modulation is also supported by the observation of the disappearance of the solid-liquid coexistence point at $T = 220$ K, $\rho = 1.37$ g cm^{-3}, and $\alpha = 0$, and 0.2 in the phase diagram (Fig. 5.1).

We compare the effect of the corrugated wall on the liquid with MD calculations with the one obtained with AIMD calculations. The red points in Fig. 5.1 represent the density, temperature, and α values for which AIMD calculations have been done. The

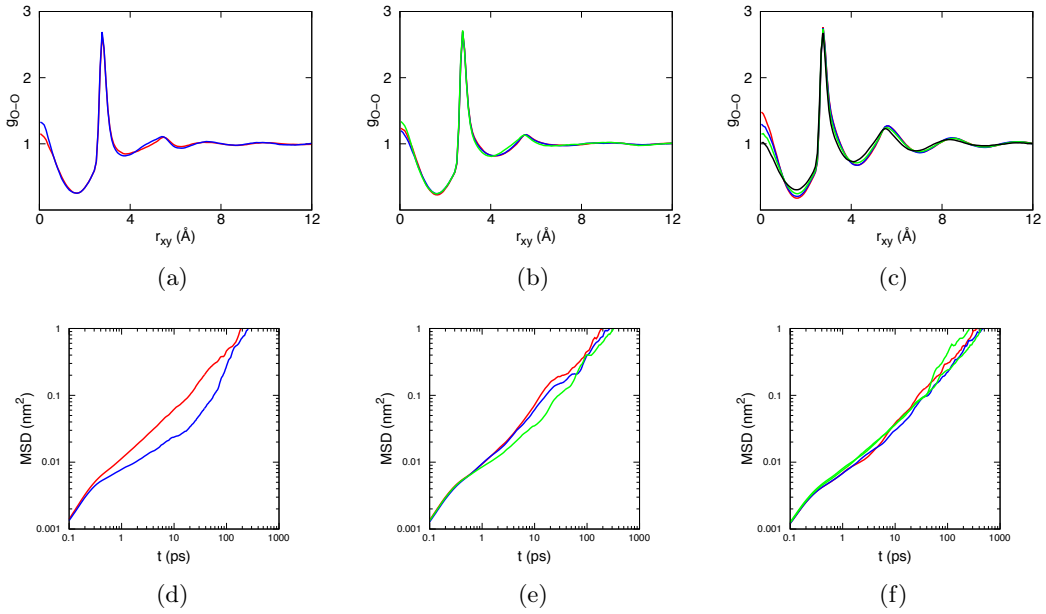

Figure 5.8: Oxygen-oxygen radial distribution function (a-c) and mean-square displacement (d-f) at $\rho = 1.17$ g cm^{-3} [(a),(d)], 1.27 g cm^{-3} [(b),(e)], and 1.37 g cm^{-3} [(c),(f)] for $\alpha = 0.0$ (red), 0.2 (blue), 0.4 (green), and 0.6 (black), and $a = 4.78$ Å.

direct comparison of the RDFs obtained at $\rho = 1.37$ g cm^{-3} and $T = 300$ K (Fig. 5.10) show the good agreement between the structural results obtained by the two different methods. The results with planar confinement, together with the ones shown here indicate that the results obtained with the TIP4P/2005 empirical force-field and the *ab inito* molecular dynamics with the vdW-DF$^{\mathrm{PBE}}$ functional agree surprisingly well.

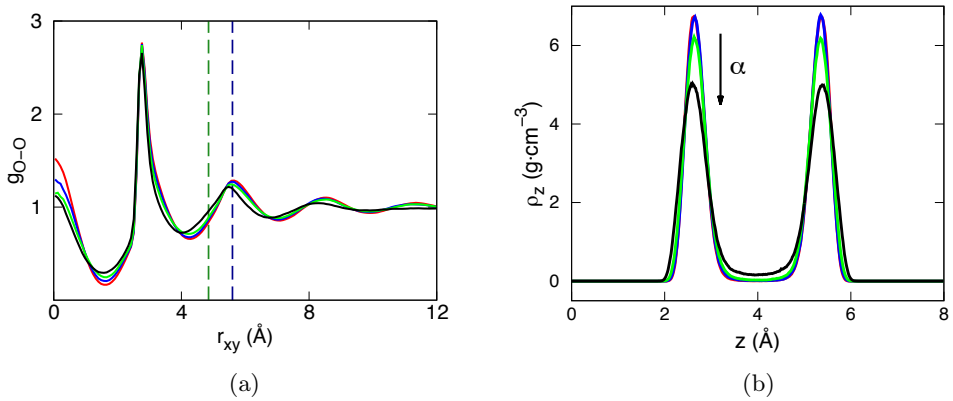

Figure 5.9: (a) Oxygen-oxygen radial distribution function, and (b) density profile both at $T = 300$ K, and $\rho = 1.37$ g cm^{-3} for $\alpha = 0$ (red), 0.2 (blue), 0.4 (green), and 0.6 (black). The vertical dashed lines in (a) highlight the second neighbor peak characteristic for the triangular ice (dark blue) and the honeycomb ice (green) RDFs.

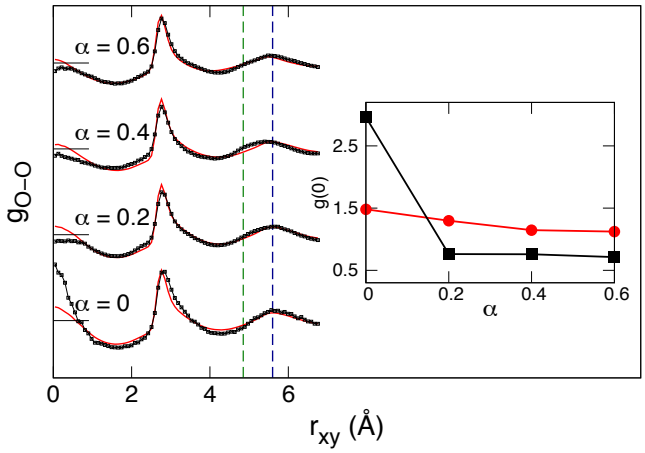

Figure 5.10: Oxygen-oxygen radial distribution functions at $T = 300$ K, and $\rho = 1.37$ g cm^{-3} for different values of α. The curves are shifted on the y axis; the value of saturation of each curve is marked by a horizontal line. The smooth-line curves correspond to the MD calculations while the line-points curves to the AIMD calculations. The vertical dashed lines highlight the position of the second neighbor peak characteristic in the triangular ice (dark blue) and the honeycomb ice (green) RDFs. The inset shows the value at the origin of the RDFs obtained by MD calculations (red circles), and AIMD calculations (black squares).

The small differences between the RDFs obtained by AIMD and MD calculations agree with what presented in previous reports: the RDFs obtained by AIMD are more structured, showing larger correlation peaks positioned on the O-O distances characteristic of the triangular ice. Both calculation methods show that the liquid is triangularly structured independently of the density. It is particular of the AIMD RDFs however, that the activation of the modulation affects significantly the maximum at $r_{xy} = 0$, which measures the interplanar on-top correlation. The peak at the origin of the RDF is characteristically pronounced for a triangular liquid where there is a tendency for the AA stacking. The peak decreases abruptly for AIMD when $\alpha = 0.2$ for all the sampled densities. In order to understand this behavior, we calculate the interlayer RDF, which takes into account the correlation of an oxygen atom with the oxygens of the other layer.

Fig. 5.11 shows the interlayer RDFs and density profiles at $T = 300$ K and $\rho = 1.37$ g cm^{-3} for different modulation amplitudes obtained by AIMD calculations. The $\rho(z)$ density profiles show that once the corrugation is activated the two water layers get significantly closer to each other and the intensity of the peaks decreases as the amplitude of the modulation increases. As the AIMD liquid is more triangularly struc-

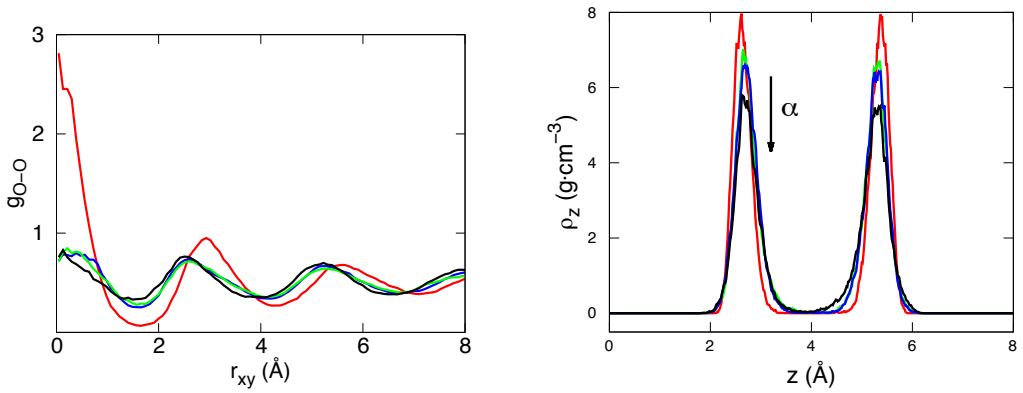

(a) (b)

Figure 5.11: (a) Oxygen-oxygen interlayer radial distribution function, and (b) density profile both at $T = 300$ K and $\rho = 1.37$ g cm^{-3} for $\alpha = 0$ (red), 0.2 (blue), 0.4 (green), and 0.6 (black).

tured than the MD one, and the external modulation frustrates triangularly structured phases, the effect of the modulation in the AIMD calculation is greater than in the MD case. Therefore, the oxygens closer to maxima of the modulation tend to locate closer to the centre of the confinement width displacing the peaks of the density profiles. This displacement explains the loss of AA stacking: the distance between the oxygen layers becomes smaller than the optimal distance for a vertical H-bond, and therefore, the vertical bonds get tilted with respect to the z axis. The effect on the stacking is also seen by the slight differences of the peak away from $r_{\mathrm{xy}} = 0$ in Fig 5.11 (a), which is accompanied by a small displacement of the other peaks towards smaller distances, reflect of the change in stacking correlations.

The obtained diffusivities for the liquid and solid phases for all the values of α agree with the ones calculated in previous chapters and observed for bulk water. At $T = 300$ K, the liquid has a diffusivity of the order of $D \sim 10^{-5}$ cm^{2}s^{-1} while the solid phases $D \sim 10^{-8} - 10^{-9}$ cm^{2}s^{-1}. The calculations of the mean-square displacement at the different points of the phase diagrams show that for a given T and ρ, the diffusivity does not significantly change with α, as long as a phase transition does not occur (Fig. 5.8).

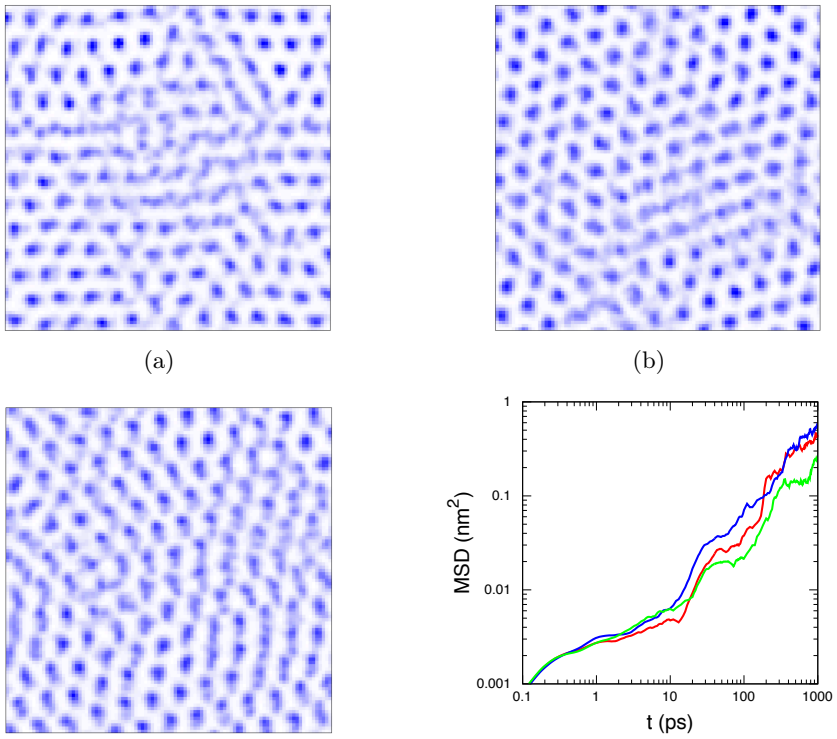

Figure 5.12: xy averaged positions of the oxygen atoms over 100 ps at $T = 300$ K and $\rho = 1.47$ g cm^{-3} for $\alpha = 1.0$ and $a = 2.5$ Å (a), 2.75 Å (b), and 3.0 Å (c). (d) Mean-square displacement of oxygens at $T = 300$ K and $\rho = 1.47$ g cm^{-3} for $a = 2.5$ Å (red), 2.75 Å (blue), and 3.0 Å (green).

5.2 Realistic lattice parameters

After analyzing a lattice parameter that is ideally commensurated with honeycomb ice, we study the effect of corrugated walls with more realistic lattice parameters. We chose three different triangular lattice parameters $a = 2.5$, 2.75, and 3 Å that cover a range of typical values for closed-packed metal surfaces, such as Ni (2.49 Å), Cu (2.56 Å), Pt (2.78 Å), Au (2.88 Å), and Ag (2.89 Å). In this section we restrict our simulation to $T = 300$ K, which corresponds to the highest T in Fig 5.1.

5.2.1 Structure

We carry out MD calculations for the same densities as in the previous section, and $\alpha = 0.2$, 0.4, 0.6, 0.8, and 1.0. We observe no significant change in the different phases under

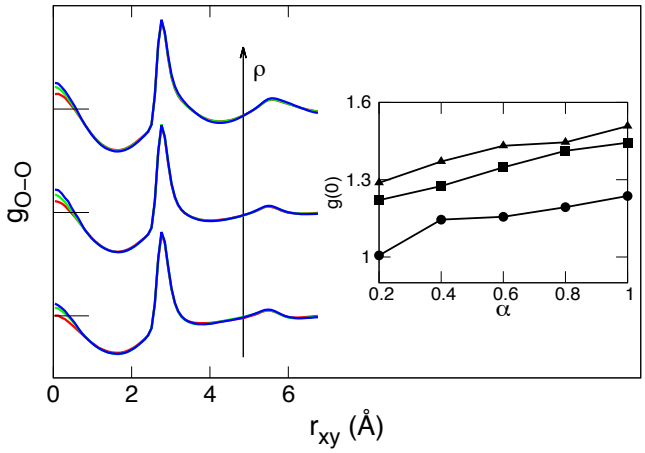

Figure 5.13: RDFs for $a = 3.0$ Å at $\rho = 1.17$ (below), 1.27 (middle), and 1.37 (above) g cm^{-3} at $\alpha = 0.2$ (red), 0.6 (green), and 1.0 (blue). The curves are shifted on the y axis; the value of saturation of each curve is marked by a horizontal finite line. The inset shows how the value $g_{\text{O-O}}(0)$ changes for each value of density with respect to the modulation amplitude α.

the effect of the corrugation, staying liquid at low densities and triangularly structured at high densities independently of α [as in Fig. 5.1(a) at $T = 300$ K]. The high-density triangular phase shows the features of the hexatic phase previously mentioned: similar RDFs, and a clear triangular lattice in the xy averaged positions of the oxygens with the usual shear motions along the main directions of the lattice (Fig. 5.12). The liquid shows almost no change in the RDFs, and density profiles when varying α. Fig. 5.13 shows the RDFs for $a = 3.0$ Å at $\rho = 1.17$, 1.27, and 1.37 g cm^{-3} (different heights for each ρ), and $\alpha = 0.2$, 0.6, and 1.0. When $r_{\text{xy}} > 1.0$ Å, the RDFs with the same density and different values of α are almost indistinguishable among them. The peak around $r_{\text{xy}} = 0$ Å, which contains information about the interlayer on-top correlation, shows a small tendency to increase with α (inset in Fig. 5.13) the opposite of the behavior for the ideal a. This means that as the corrugation increases, the liquid tends to structure into better AA stacking. From these results we deduce that for $a = 3.0$ Å, although the relative distances among oxygen atoms are almost unaffected by the corrugation, the water molecules from one layer tend to be on top of another from the other layer as the corrugation increases. The figures are very similar for $a = 2.5$, and 2.75 Å and the same conclusions can be drawn for them (Fig. 5.14).

Although the RDFs and density profiles of oxygens suggest that the structure of the liquid is barely affected by the corrugation, the xy averaged positions of the

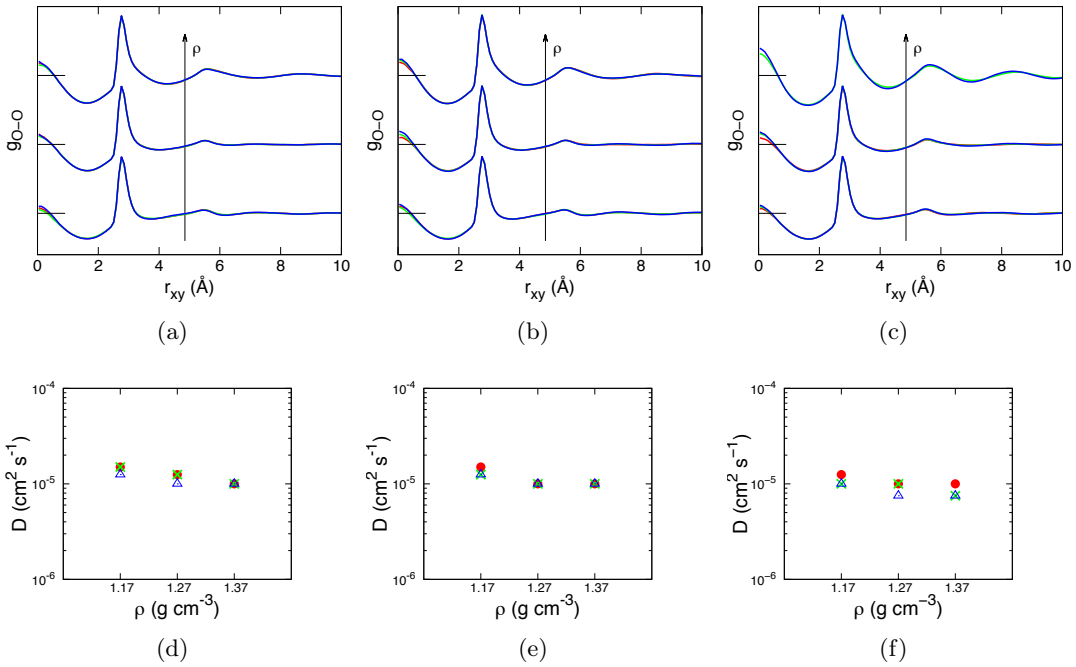

Figure 5.14: Oxygen-oxygen radial distribution function (a-c) and diffusivities (d-f) at $a = 2.5$ Å [(a),(e)], 2.75 Å [(b),(e)], and 3.0 Å [(c),(f)] for $\alpha = 0.2$ [red (a-c) and red circle (d-f)], 0.6 [green (a-c) and green cross (d-f)], 1.0 [blue (a-c) and blue triangle (d-f)]. (a-c) The RDFs are shifted on the y axis depending on the density: $\rho = 1.17$ g cm^{-3} (below), 1.27 g cm^{-3} (middle), and 1.37 g cm^{-3} (top); the value of saturation of each curve is marked by a horizontal line.

oxygens shows clear effects on the structure of the liquid. The insets in Fig. 5.15 show the oxygen xy averaged positions for $a = 3.0$ Å, at $\rho = 1.27$ g cm^{-3}, and $\alpha = 0.2, 0.6, 1.0$. When the corrugation is activated, the oxygens avoid being close to the Lennard-Jones confining particles due to the repulsive force and they are structured anisotropically, resulting in the heterogeneous images shown in the insets of Fig. 5.15. The maximum value of the density oscillations in the insets are 138%, 186%, and 237% times the mean value of the density for $\alpha = 0.2$, 0.6, and 1.0 respectively. To quantify the effect of this structuring of the liquid, we calculate the dipole distribution function (DDF): we average the distribution of the polar angle (projected in the xy plane) of the molecular dipoles. Fig. 5.15 shows the DDFs for $a = 3.0$ Å, at $\rho = 1.27$ g cm^{-3}, and $\alpha = 0.2$, 0.6, 1. We can clearly observe that as α increases, the DDFs show six pronounced peaks in the multiples of 60°. This anisotropic structuring effect is observed for all sampled points of the liquid phase, and it is greater as ρ, and a are increased. These results show that the (not surprising) anisotropy in the molecular density of the liquid has a surprisingly small effect in the liquid structure (correlation) and dynamics (diffusivity).

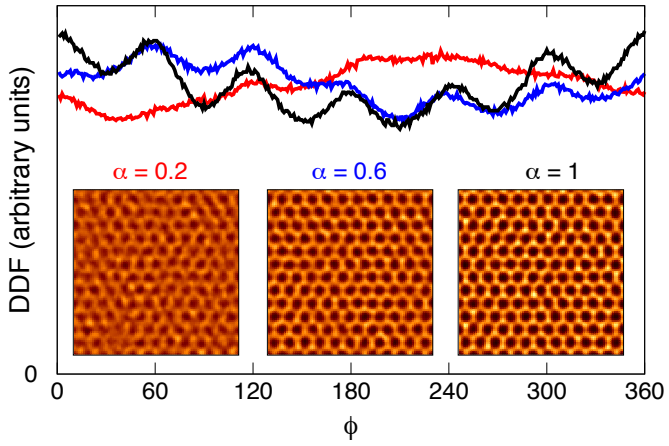

Figure 5.15: Dipolar angle distribution function of the water molecules for $a = 3.0$ Å at $T = 300$ K, $\rho = 1.27$ g cm^{-3}, and $\alpha = 0.2$ (red), 0.6 (blue), and 1.0 (black). The insets show the mxy averaged positions of the oxygens at the three values of α: the brighter the color, the larger the density.

We now compare the results obtained by MD and AIMD calculations at $T = 300$ K, and $P_{\parallel} = 0$, for different values of α and a. Fig. 5.16 shows the RDFs obtained by MD and AIMD calculations at $a = 2.5$, 2.75, and 3.0 Å, and $\alpha = 0.2$, 0.6, and 1.0. The effect of the corrugation in the RDFs is as negligible for AIMD as it was for MD. From the direct comparison of the MD and AIMD RDFs we obtain the same conclusions to the ones in the previous section: both methods give similar structural features of the liquid, but with the difference that the AIMD RDFs tend to be more triangularly structured showing a larger peak at $r_{\mathrm{t}} = 2r_{\mathrm{O\text{-}O}}$. This is also supported by the comparison of the density profiles $\rho(z)$ obtained by both calculation methods: although they are very similar, the ones obtained by AIMD show more pronounced peaks. These results agree with the results obtained for $a = 4.78$ Å and previous works where the same empirical force-field and DFT functional [2, 10] were used. The differences between both methods are minor.

5.2.2 Diffusivity

As previously mentioned, with no corrugation ($\alpha = 0$) the sampled liquid points of the phase diagram show diffusivities of the order of $D \sim 10^{-5}$ cm^{2}s^{-1}, while for the hexatic phase $D \sim 10^{-7}$ cm^{2}s^{-1}. When the corrugation is applied with these three lattice parameters, and different values of α, the diffusivities barely change in the liquid

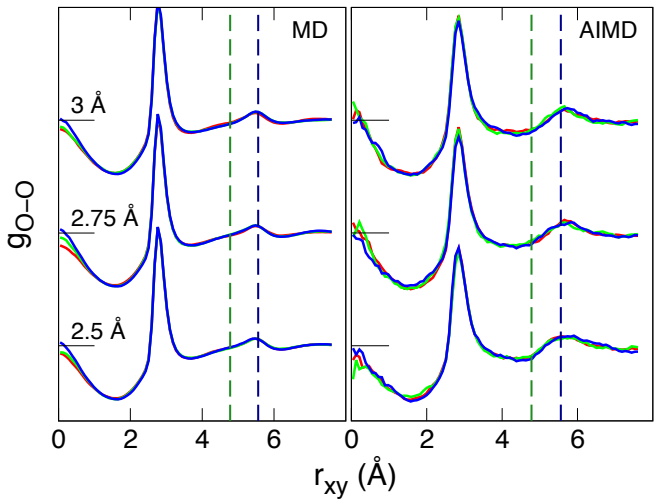

Figure 5.16: RDFs obtained by MD (left), and AIMD (right) calculations at T = 300 K, and $P_{\|} = 0$. A different height is given to the curves for each lattice parameter: a = 2.5 (bottom), 2.75 (middle), and 3.0 Å (top). For each lattice parameter, there are three curves, each one corresponding to a different value of α = 0.2 (red), 0.6 (green), and 1.0 (blue). The value of saturation of each curve is marked by a horizontal line. The vertical dashed lines highlight the position of the second neighbor peak for the triangular ice (dark blue) $r_{\mathrm{t}} = 2r_{\mathrm{O\text{-}O}}$ and the honeycomb ice (green) $r_{\mathrm{h}} = \sqrt{3}r_{\mathrm{O\text{-}O}}$.

and in the triangular phase (Fig. 5.14). The small changes with α in the mean square displacements curves are within the noise of the signal and do not display any clear trend; therefore, we conclude that within our accuracy, the diffusivities are barely affected by the corrugation formed with these three lattice parameters.

References

[1] S. Han,, M. Choi, P. Kumar, and H. E. Stanley, (2010) *Nat. Phys.* **6(9)**, 685–689.

[2] J. Zubeltzu, F. Corsetti, M.-V. Fernández-Serra, and E. Artacho, (2011) *Phys. Rev. E* **93**, 062137.

[3] J. Mittal and G. Hummer, (2010) *Farad. Discuss.* **146,**, 341.

[4] M. Fitzner, G. C. Sosso, S. J. Cox, and A. Michaelides, (2016) *arXiv* 1611.08605.

[5] J. M. Kosterlitz, and D. J. Thouless, (1973) *J. Phys. C: Solid State* **6(7)**, 1181.

[6] A. Young, (1979) *Phys. Rev. B* **19(4)**, 1855.

[7] B. Halperin, and D. R. Nelson, (1978) *Phys. Rev. Lett.* **41(2)**, 121.

[8] D. R. Nelson, and B. Halperin, (1979) *Phys. Rev. B* **19(5)**, 2457.

[9] H. H. vonGrünberg, P. Keim, and G. Maret, (2007).

[10] F. Corsetti, J. Zubeltzu, and E. Artacho, (2016) *Phys. Rev. Lett.* **116(8)**, 085901.

Chapter 6

Graphene

As previously mentioned in Chapter 1, 2D materials are promising substrates to carry out the water confinement. Graphene, in particular, is one of the main candidates due to its unique properties and the great advance made on its manipulation during the last years. Algara *et al.* [1] recently claimed that they were able to observe the structure of water confined between two graphene sheets by the high resolution transmission electron microscope (HRTEM). In this chapter, we analyze the structural response of a dry bilayer graphene sample exposed to an electron radiation similar to the one received in a HRTEM, as the previous step of studying confined water between graphene layers in the HRTEM. As the study carried out in this chapter is a branch coming from the main script of this thesis (we do not study water in this chapter), it has its own introduction and methods section.

6.1 Introduction

Nowadays, graphene is one of the most promising and studied materials in the world. The high electronic conductivity and mechanical strength are examples of many singular and desirable properties that this material is characterized by [2–4]. However, previous studies have shown [5–8] that these singular properties are strongly altered by the presence of defects. Thus, the study of energetics and mechanisms of defect formation, diffusion, and transformation has become an important task in order to control the behavior of graphitic materials: either to maintain their original properties or to change them in a desired way.

In this respect, HRTEM is an ideal tool to carry out this kind of studies, since it provides a controllable impact to the sample by high energy electron flux and, at the same time, the observation of the structural response of the system at the atomic level. Variation of primary electron energy gives a control over the energy transferred to the sample (typically below 20 eV per electronic collision), while variation of the electron flux regulates the rate of transformations [9, 10]. In recent years, many types of graphene defects have been analyzed and their energetic and electronic properties have been characterized experimentally and by theoretical simulations [11–15]. There is a growing number of experimental studies in which the formation and transformation processes of graphene defects have been observed [16–19], and the interest in this topic has even increased since the introduction of Cs-corrected microscopes. [20, 21] Although there has been a substantial theoretical and experimental effort to reveal the mechanisms and key parameters which are responsible for structural transformations in graphene, [22–25] there are still many unanswered questions.

When radiation energy in a transmission electron microscope is around 100 keV, the formation of vacancies can be observed in a graphene sample [5, 10, 13, 22, 23, 26]. In order to study the formation mechanism of vacancies by *ab initio* molecular dynamics simulations, usually the classical static lattice approximation is made [22, 23, 27] where the expulsion threshold energy is defined. Below this energy limit, the likeliness to expel an atom is zero, and thus the creation of vacancies is not possible. McKinley and Feshbach [28] obtained an analytical expression that relates the displacement cross section with the incoming electronic energy within this assumption and predicts a displacement threshold energy of 110 keV for graphene. Recently however, Meyer *et al.* [26] have shown the importance of the phonon contribution to the displacement cross section: if the zero-point motion is considered, the experimental results are almost perfectly fitted. Figure 6.1 shows the calculated displacement cross section as a function of the radiation energy for both models. When considering the zero-point motion, the tail of the curve descends asymptotically to zero; therefore, the displacement threshold energy is no longer well defined.

As shall be described in subsequent sections, for radiation energies of 80 keV, bilayer graphene shows a substantial increase on the displacement cross section with respect to the monolayer graphene sample. For an electronic dose of the order of 10^{10} e^-/nm^2 the formation of several vacancies is observed in bilayer graphene, while in monolayer graphene the formation of one vacancy is unlikely [26].

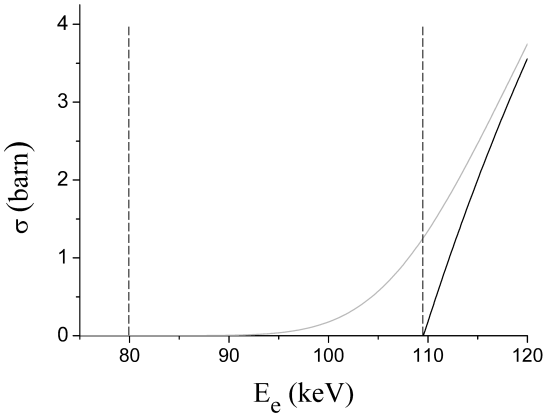

Figure 6.1: Two different displacement cross sections as a function of the incoming electronic energy. The function obtained by McKinley and Feshbach (dark) predicts a displacement threshold energy of $E_{thr}^{MF} \approx 110$ keV. If the zero-point motion of the carbon atoms in graphene is taken into account (light), the displacement threshold energy is not well defined and the experimental results are much better reproduced.

In this chapter, we analyze the possible mechanisms of defect formation under electron radiation in bilayer graphene. We explore and rule out a number of possible explanations for the very high sputtering cross section observed experimentally. We finally propose a new concept of multistep sputtering process and prove its feasibility.

6.2 Methods

6.2.1 Experimental methods

The HRTEM image series are acquired on a Titan 60-300 electron microscope (FEI, Netherlands) equipped with a high brightness electron gun (xFEG), monochromator, imaging Cs corrector, Ultrascan1000 2Kx2K CCD camera, and a GIF Quantum electron energy loss spectrometer (EELS) (Gatan, USA). The microscope is operated at 80 kV acceleration voltage, the beam is monochromated to about 100 meV energy spread (as measured by full width at half maximum of the zero loss EELS peak), and the image corrector is tuned so that the third-order spherical aberration coefficient is equal to -20 μm. Images are recorded on the pre-GIF camera with an exposition time equal to 1 s.

A post-specimen blanker is used in the experiment, so that the sample is continuously illuminated even between expositions. The dose rate at exposition time is

determined from the image intensity, and the dose rate between expositions is linearly interpolated. The total dose is calculated as an integral over time assuming the dose rate as described above.

The image simulations are performed by means of the MUSLI package [29] which is based on the implementation of the fast-fourier-transforms multislice algorithm and assuming neutral atoms. Electron statistics is accounted for in accordance to the experimentally measured dose; the modulation transfer function of the CCD camera is applied on thus simulated images.

The monolayer graphene samples are grown by chemical vapor deposition (CVD) using 25 μm copper foil as the catalyst. The monolayer samples are transferred onto Quantifoil Au TEM grids (hole size 2 μm) using polymethyl methacrylate (PMMA) as the sacrificial polymer layer and ferric chloride as the copper etching agent. In order to prepare the bilayer samples, the transfer process is repeated twice.

6.2.2 Theoretical methods

To carry out the theoretical calculations, we employ the SIESTA method [30] based on density-functional theory (DFT). It is characterized by the use of norm-conserving pseudopotentials [31] and finite-support atomic-like basis-sets. We use the van der Waals density functional (vdW-DF) [32] as the exchange-correlation functional in order to take into account van der Waals forces between graphene sheets. Computational parameters have been optimized as follows, in order to achieve a convergence of 1 meV per atom. We use a double-ζ polarized (DZP) basis, available in SIESTA's main web page [33] and a real-space grid with a 100 Ry mesh cutoff.

To calculate the energy of the pristine and defective systems, we relax the system by the conjugate gradient method [34], to within a force tolerance of 0.01 eV/Å. All the relaxation calculations are carried out with no symmetry constraints. We use a large enough supercell to contain our defect and sufficiently reduce the finite-size effects of the calculations. The employed rectangular supercell contains 384 atoms and the edges are defined as:

$$\begin{pmatrix} \mathbf{L}_x \\ \mathbf{L}_y \end{pmatrix} = \begin{pmatrix} 8 & 0 \\ -6 & 12 \end{pmatrix} \begin{pmatrix} \mathbf{a}_1 \\ \mathbf{a}_2 \end{pmatrix}, \tag{6.1}$$

where $\mathbf{a}_1$ and $\mathbf{a}_2$ are the primitive lattice vectors of graphene defined as in Shallcross *et al.* [35] The y edge of the supercell is larger because the extension of the defect in

that direction is larger. For the **k**-point sampling of the Brillouin zone a $(3 \times 2 \times 1)$ Monkhorst-Pack matrix [36] is chosen.

Although one layer is rotated respect to the other in the bilayer graphene sample, we will assume that both sheets are always in a parallel orientation. The rotation of one of the layers in our simulation box would break the periodicity in our supercell and a much bigger cell would be needed to carry out the calculations. To reproduce the different local stackings that are formed in the sample, we translate one of the layers.

In Table 6.1 we show the values obtained for the inter planar distance between two graphene layers c and the energy difference per atom between a bilayer graphene system with an AA and AB stacking $\Delta E_{AA/AB}$. In order to check the reliability of the calculations, we add the same magnitudes obtained by Birowska *et al.* [37] with the same exchange-correlation functional (vdW-DF) and the experimental value for the interlayer distance for graphite [38]. If we compare the data shown in Table 6.1 we conclude that the obtained interlayer distance is close to its experimental value, and that the difference in $\Delta E_{AA/AB}$ is within the error of 1 meV per atom.

In the kinetic analysis, we make two justified assumptions for simplicity: firstly, as the rate for a thermally activated process is proportional to $e^{-\frac{\Delta E}{kT}}$, and in our case, the activation barriers ΔE are of the order of 1 eV, we may neglect thermally activated processes and consider activation by electron collision only. Secondly, the time interval between a scattering event involving a given atom and a second scattering event in its neighborhood is greater than the relaxation time of the system, thus the processes activated by electronic radiation will be treated as being caused by singular scattering events and the system always remains relaxed between these scattering events.

For simulating the kinetic process after the collision, we suppose that the electrons are coming from $z = -\infty$ having a velocity parallel and positive in the z axis. The graphene layers remain perpendicularly oriented to the electron beam.

For describing the evolution of the system after an electron scattering event, we use *ab initio* molecular dynamics (AIMD): we divide the time in 1 fs timesteps and for each one the forces are calculated on each atom using the DFT method discussed above. The equations of motion are then solved by Verlet integration [39]. At time $t = 0$ the system remains relaxed and all the atoms are at rest, thus neither temperature nor zero-point motion contributions are taken into account. Therefore, within this model, we can define the expulsion threshold energy, which is the minimum energy needed to

Table 6.1: Interlayer distance and energy difference per atom between AA and AB stackings in bilayer graphene and graphite.

	System	c (Å)	$\Delta E_{AA/AB}$ ($\frac{\text{meV}}{\text{atom}}$)
This study	Bilayer	3.343	8.5
Birowska *et al.* [37]	Bilayer	3.349	7.5
Expt. [38]	Graphite	3.356	

expel an atom from the system.

To simulate the collision of the electron with the atom, a certain velocity is given to one atom from the sample. In this case, as the initial states from which the AIMD simulations are initiated do not contain large defects, we use a smaller supercell to reduce the computational cost. The dimensions of the supercell are:

$$\begin{pmatrix} \mathbf{L}_x \\ \mathbf{L}_y \end{pmatrix} = \begin{pmatrix} 7 & 0 \\ -5 & 10 \end{pmatrix} \begin{pmatrix} \mathbf{a}_1 \\ \mathbf{a}_2 \end{pmatrix}, \tag{6.2}$$

and it contains 280 atoms. For the **k**-point sampling a $(3 \times 3 \times 1)$ Monkhorst-Pack matrix is employed.

Considering the electron as a relativistic particle and the atom as a classical one which remains at rest, we can obtain an analytical expression for the maximum kinetic energy that is transferred to the latter in a pure elastic head-on collision [27]:

$$T_{max} = \frac{2ME(E + 2mc^2)}{(M+m)^2c^2 + 2ME}\,, \tag{6.3}$$

where T_{max} is the maximum kinetic energy of the atom along the same direction of the incident electron, M and m are the masses of the atom and electron respectively, c is the speed of light, and E is the energy of the electron. If the atom is emitted in another direction, the maximum obtainable kinetic energy becomes

$$T_{max}(\theta) = T_{max}\cos^2\theta, \tag{6.4}$$

where θ is the emission angle and is defined by the angle between the direction of the incident electron and emitted atom. Therefore, by using Eqs. 6.3 and 6.4 we obtain the maximum kinetic energy that an atom from the sample can achieve for a certain emission angle $T_{max}(\theta)$ from the energy E of the electrons in the HRTEM. The kinetic energy given to the atom at the initial state of the AIMD simulations will be equal

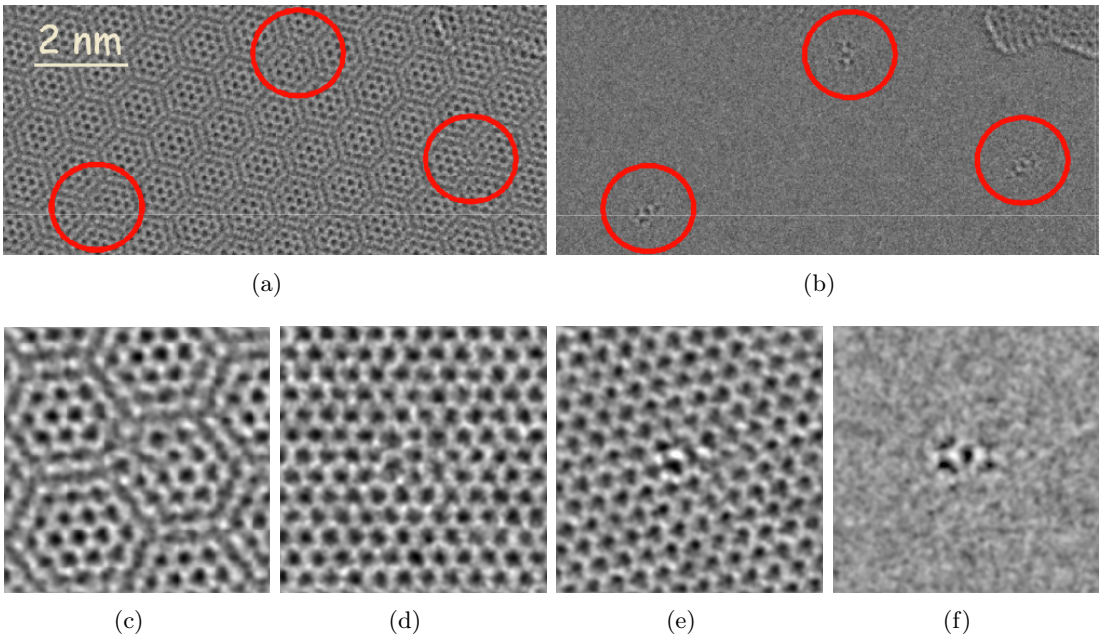

Figure 6.2: HRTEM images of bilayer graphene obtained by Andrey Chuvilin [40]. (a) Overview image showing the obtained Moiré pattern. In the regions marked by the circles the distortions of the pattern are visible. (b) The same area, but the honeycomb lattices of both layers are removed by Fourier filtering. Characteristic patterns in the shape of double dumbbells appear inside the circles indicating the same type of lattice distortion in all three places. (c) Enlarged image of one of the distorted Moiré pattern areas. (d)−(f) Fourier filtered images of the enlarged area with the second (d), first (e) and both graphene layers filtered out (f). The image of the first layer only (d) can be directly interpreted in terms of atom positions and reveals a V_2(5555-6-7777) butterfly defect formation in this layer. Image of the second layer (e) cannot be interpreted directly and needs simulations in order to find its origin.

to or smaller than the maximum kinetic energy achievable by the atom because of the collision with the electron.

To estimate the defect population in the sample, we will assume that the rate of a given reversible reaction activated by electron-atom collisions,

$$\mathrm{A} \longleftrightarrow \mathrm{B}, \tag{6.5}$$

follows a first order rate law:

$$-\frac{d[\mathrm{A}]}{dt} = k_f[\mathrm{A}] - k_b[\mathrm{B}], \tag{6.6}$$

where [A] and [B] are the time-dependent concentrations of A and B species respectively, and k_f and k_b are the rate constants for the forward and backward reactions. If the

reactions are activated only by electron collisions, the rate constant is given by [9]

$$k = \sigma j, \tag{6.7}$$

where, σ is the cross section related with the process, and j is the electronic dose rate. Assuming that the initial concentration of B is zero, $[\mathrm{B}]_0 = 0$, the following condition must be fulfilled:

$$[\mathrm{A}] + [\mathrm{B}] = [\mathrm{A}]_0. \tag{6.8}$$

The solutions of Eqs. 6.6 and 6.8 are

$$[\mathrm{A}] = ([\mathrm{A}]_0 - [\mathrm{A}]_e)e^{-(k_f+k_b)t} + [\mathrm{A}]_e, \tag{6.9}$$

$$[\mathrm{B}] = (1 - e^{-(k_f+k_b)t})[\mathrm{B}]_e, \tag{6.10}$$

where $[\mathrm{A}]_e$ and $[\mathrm{B}]_e$ are the equilibrium concentrations for each species. In equilibrium, the reaction rate must be zero, $d[\mathrm{A}]/dt = 0$, and thus from Eq. 6.6 we can calculate the equilibrium relative concentration between A and B:

$$\frac{[\mathrm{A}]_e}{[\mathrm{B}]_e} = \frac{\sigma_b}{\sigma_f}, \tag{6.11}$$

where σ_b and σ_f are the cross sections related with the backward and forward reactions respectively. The possibility of using Eq. 6.11 to analyze our results is determined by the reaction velocity with which the system is approximated to the equilibrium state, given by the exponent in Eqs. 6.9 and 6.10: $k_f + k_b$. In our case, the radiation exposure time of the sample is longer than $1/(k_f + k_b)$, thus the use of Eq. 6.11 is well justified.

In order to estimate the cross section related with a given scattering event, we will use the expression of the impact parameter in a Coulomb scattering for a semiclassical relativistic electron [41]:

$$b = \frac{Ze^2 \tan\theta}{4\pi\varepsilon_0 m\gamma v^2}, \tag{6.12}$$

where Z is the atomic number of the target atom, e is the electron charge, ε_0 is the vacuum permittivity, γ is the Lorentz factor and v is the velocity of the electron. This last expression is obtained by assuming that the target atom is much heavier than the electron ($M \gg m$) and large bombarding energies. The angle θ is obtained from Eq. 6.4, where $T_{max}(\theta)$ in this case, is taken as the activation energy for a given process. Once the impact parameter is known, the cross section is given by:

$$\sigma = \pi b^2. \tag{6.13}$$

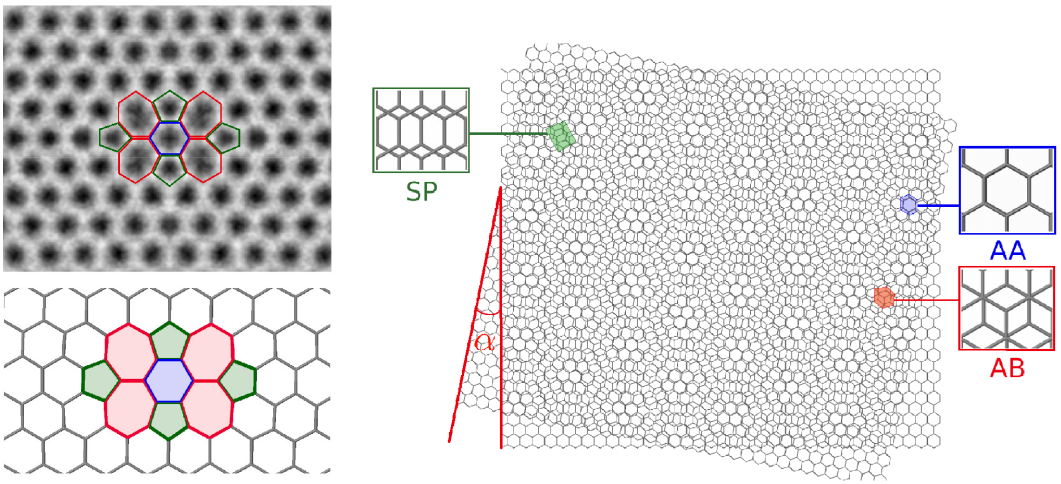

(a) (b)

Figure 6.3: (a) Experimental image averaged over all observed butterfly defects obtained by Andrey Chuvilin [40] clearly showing its structure and a corresponding drawing of the defect. Four heptagonal (red), four pentagonal (green) and one rotated central hexagonal (blue) rings are formed instead of the original hexagonal lattice. (b) Atomic model of the graphene layers used for image simulations. One of the layers is rotated an angle $\alpha = 11.2°$. Different local stackings are formed in different small areas within the large hexagons.

In some case, the activation energies that we use are thermal barriers, i.e., the minimum energy required by the system in order to activate a process. However, we are assuming that these barriers are isotropic in the xy plane, and once the activation energy is obtained by the scattered atom, the process is always be initiated. In addition, as the atoms remain frozen and the energy is given only to the scattered atom, the barrier that this atom will have to overcome is always greater than the thermal one, which is not taken into account in the previous equations. Therefore, the cross sections and consequently defect concentration that we will estimate in the results will always be overestimated.

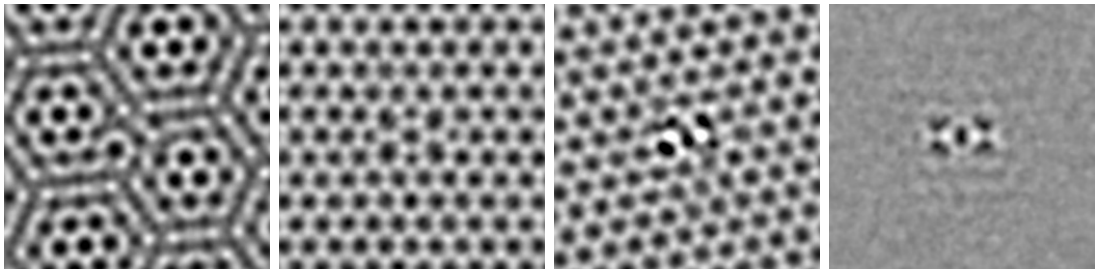

(a) (b) (c) (d)

Figure 6.4: Simulated image by Andrey Chuvilin [40] of the central part shown at the same scale and with the same processing as experimental images in Figs. 6.2(c)−6.2(f). The butterfly defect is located in the first layer and the second one is kept pristine. The feature similar to Fig. 6.2(e) is observed on the simulated second layer (c) comprising pristine graphene. It can be thus concluded that this feature in the second layer is an artifact of Fourier filtering.

6.3 Results

6.3.1 Experimental results

In Fig. 6.2 we observe a bilayer graphene sample with a rotation angle between layers of 11.2°. A characteristic hexagonal Moiré pattern is observed in HRTEM images due to this rotational misfit. After extended observation time we start to observe distortions on the Moiré figures, which are attributed to radiation generated defects. Fourier filtering of lattice patterns of one and the other layer clearly reveals that we observe V_2(5555-6-7777) type divacancies, in one and the same layer always. From HRTEM images only it is impossible to determine whether the layer containing the defects is an upper or lower one with respect to electron beam propagation direction (from theory we can, as shown later). The filtered image of the second layer represents an irregular pattern at the position of the defect, which is not possible to interpret directly. Removal of both lattices from the image produces a characteristic signature of a V_2(5555-6-7777) defect in the shape of dumbbell. Figure 6.2 shows all the observations described above.

The simulation of the observed defect confirms that the formed defects are V_2(5555-6-7777) divacancies, or for simplicity, butterfly defects (Fig. 6.3). They are characterized by the formation of four heptagonal, four pentagonal, and one rotated central hexagonal carbon rings. The simulation of the formed Moiré pattern is shown in Fig. 6.3, where we can clearly distinguish three characteristic zones depending on the different local

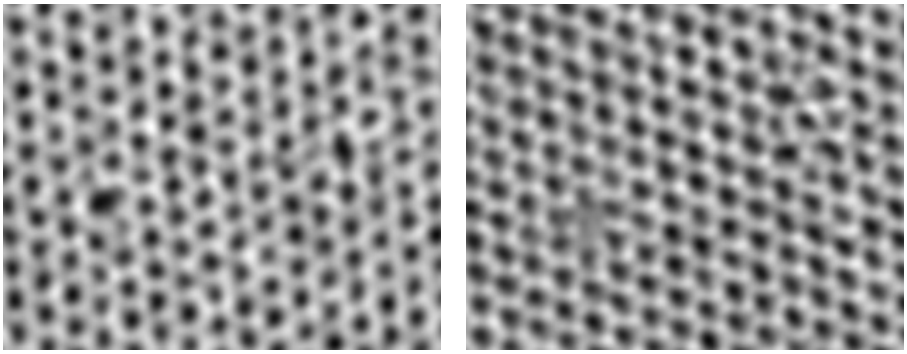

(a) (b)

Figure 6.5: Enlarged experimental HRTEM images obtained during experiment by Andrey Chuvilin [40]. The second honeycomb lattice is filtered out. (a) Two V_2(5-8-5) divacancies are distinguished in the first. (b) After 7.5 e/nm^2 of electronic dose, one of the divacancies (left) is in the process of transformation while the other (right) is converted into a butterfly defect.

stackings: an AA stacking at the center of the hexagons, a local AB stacking at the corners, and a saddle point (SP) stacking at the edges. This last one can be obtained if one layer is translated a half-bond distance through a bond direction from the AB stacking. If we pay attention to the location of the defects in Fig. 6.2, we observe that they are stabilized close to the edges (SP) and corners (AB) of the large hexagons of the Moiré pattern in all cases. This last observation suggests that the stacking influences the stabilization of the defects.

The HRTEM image simulation of the bilayer rotated by 11.2° with V_2(5555-6-7777) defect presented in one of the layers reproduces exactly all experimentally observed features (Fig. 6.4): the Moiré distortion, the V_2(5555-6-7777) image in one of the layers while applying the same Fourier filter, the disordered structure in the second layer, and the dumbbell signature when both lattices are filtered out. On the basis of this analysis we can conclude that we do really see divacancy generation in one of the layers, and the disordered structure observed in the second layer is an artifact of Fourier filtration.

During image series acquisition, it is observed that V_2(5-8-5) (Fig. 6.5) and V_2(555-777) [42] divacancies are formed before they are converted into butterfly defects. The evolution V_2(5-8-5)$\longrightarrow V_2$(5555-6-7777) can be understood by two Stone-Wales transformations [22, 23]: if one of the bonds from V_2(5-8-5) is rotated 90°, a V_2(555-777) divacancy is formed and, if once again a second bond is rotated, the butterfly defect is obtained.

We monitor the total deposited dose from the pristine bilayer until three butterfly defects are observed in the field of view within the area of 52 nm^2. The total dose accumulated during this observation is $1.3\times10^{10}e^-/nm^2$. The cross section of C atom sputtering calculated from this data is σ=1.2 mb, which is by at least two orders of magnitude higher than the estimation of the low limit of sputtering cross section for a single layer [26]. In combination with the fact that the vacancies were only created in one layer, our observation points to a strong synergetic influence of the second layer on the sputtering process. Hereafter we evaluate possible mechanisms which may contribute to this synergy.

6.3.2 Theoretical results

We consider two possible causes that could be behind this phenomenon: an increase of the stability of the defect from monolayer to bilayer graphene, or a catalytic effect of the second layer during the creation process of the divacancy.

Stability

In order to measure the stability of the butterfly defect in monolayer and bilayer graphene we calculate its formation energy, defined as

$$E_f = E_{def} - E_{bulk} - \Delta n \mu_c, \tag{6.14}$$

where E_{def} is the total energy of the N-atom supercell with a single defect, E_{bulk} is the total energy of the same supercell containing perfect crystal, Δn is the required change in atom number to create the defect, and μ_c is the chemical potential of carbon in the pristine configuration:

$$\mu_c = \frac{E_{bulk}}{N}. \tag{6.15}$$

The lower the value is of the formation energy of the defect, the higher is its stability. For the butterfly defect in monolayer graphene we obtain

$$E_f^{mono} = 7.08\,\text{eV}, \tag{6.16}$$

while in the bilayer case

$$E_f^{bi} = 6.94\,\text{eV}. \tag{6.17}$$

The stability of the butterfly defect increases from monolayer to bilayer graphene, but the energetic change is very small:

$$\Delta E_f = E_f^{bi} - E_f^{mono} = -0.14\,\text{eV}. \tag{6.18}$$

Indeed, there is only a 2% decrease of the formation energy, not sufficient to explain the big change of the displacement cross section that is observed experimentally. We conclude that the difference in energetics is not the cause of the observed phenomenon and the mechanism for the formation of the butterfly defect is different in monolayer and bilayer graphene.

The analysis of the atomic displacements that occur in both systems supports the previous conclusion: Fig. 6.6 shows the deformations that take place in monolayer and bilayer systems in the perpendicular direction multiplied by a factor of 200. For monolayer graphene, there are no appreciable displacements, while in the bilayer case we can observe that in the upper layer (the one closer to the beam source as is shown below) the central hexagon of the butterfly defect ascends and another hexagon from the lower layer (farer from the beam source) descends. However, the maximum displacements are of the order of 10^{-3} Å, consistent with the very small energetic changes.

We calculate the formation energies of the V_2(5-8-5) and V_2(555-777) divacancies in monolayer and bilayer graphene. Table 6.2 summarizes the obtained results. The

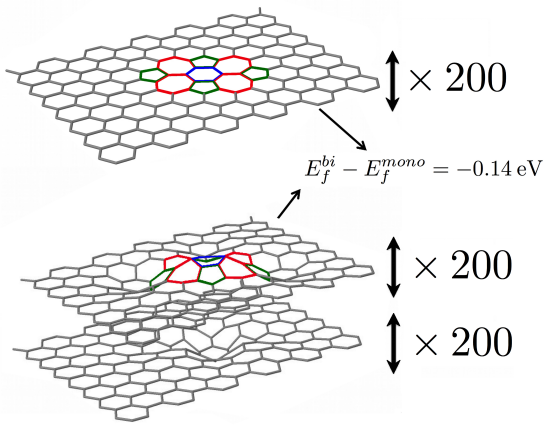

Figure 6.6: Calculated atomic displacements multiplied by a factor of 200 in the perpendicular direction of the graphene sheets made by the presence of the butterfly defect in monolayer and bilayer graphene. The formation energy difference of the defect between both systems is negligible in this context.

Table 6.2: The formation energies of three types of divacancy in monolayer and bilayer graphene

	E_f^{mono}(eV)	E_f^{bi}(eV)
V_2(5-8-5)	7.28	7.32
V_2(555-777)	6.74	6.64
V_2(5555-6-7777)	7.08	6.94

formation energies of each kind of divacancy change very little from the monolyaer system to the bilayer one. Therefore, the previous conclusion is confirmed: the energetic analysis does not explain the observed phenomenon. Looking at the results in Table 6.2, one would expect that the most stable divacancy is the V_2(555-777). However, this is in clear contrast with the experimental observation: during the electronic radiation the created divacancies form the different structures V_2(5-8-5) (as seen in Fig. 6.5) and V_2(555-777) [42], but they all finally evolve into the butterfly structure, which then remains stable. The reason for the discrepancy with the results in Table 6.2 remains unknown, being possibly related to dynamical or entropic effects.

Kinetics: one-step sputtering process

We calculate the amount of energy needed to remove an atom in the monolayer system using AIMD and verify if for lower energetic values it is possible to expel an atom in bilayer graphene. We find that the expulsion threshold energy for monolayer graphene is 22 eV, in good agreement with previous studies [27,43]. In the case of the bilayer system, we employ a sample in AB stacking. Remembering that the electron beam comes from above, we can distinguish three types of atoms depending on their configuration: An atom located in the lower layer (A), one that is situated in the upper layer and centered with respect to a lower carbon hexagon (B), and one that is located in the upper layer but is directly on top of a lower atom (C). Table 6.3 shows the expulsion threshold energy for each type and the corresponding electronic energy obtained by Eq. (6.3). Our results show that the energy needed to remove an atom from the bilayer system is equal or greater than that needed for the monolayer.

Since in the case of monolayer graphene it has been shown that the phonon contribution plays an important role in the theoretical explanation of the observed experimental displacement cross section [26], we analyze possible effects generated by lattice vibrations in bilayer graphene. By using the equations in Meyer *et al.* [26]

Table 6.3: The expulsion threshold energy in terms of the energy acquired by the atom and the corresponding incoming electronic energy for each type of atom. A, B and C refer to different configurations of carbon atoms in bilayer graphene (see text).

	Type of atom	E_{thr}(eV)	E_{thr}^{el}(keV)
Monolayer		22	110
Bilayer	A	22	110
	B	27	132
	C	32-35	153-166

we obtain that the original graphene's Debye temperature perpendicular to the plane ($\theta_D = 1287$ K [44]) at least would have to double its value for double layer in order to explain our observed experimental results ($\theta_D = 2110$ K). The perpendicular vibration modes do not change in such a substantial way because of the presence of a second graphene layer, and thus they do not cause the high increase on the displacement cross section.

Based on the previous results, we conclude that the creation process of vacancies is not caused by the direct expulsion of atoms. In addition, we observe that the lower layer has a similar kinetic behavior as the monolayer graphene system, which suggests that the origin of a different kinetic behavior comes from the collision of the electrons with the upper layer atoms.

Once the possibility of defect formation due to direct ejection of atoms is discarded, we study the possibility of creation of intermediate states allowed by the presence of the second layer that would facilitate the formation of vacancies in the sample, i.e., a catalytic process. The most intuitive candidate that would play such a role is the Frenkel pair (Fig. 6.7), where the "kicked" atom does not escape from the system but remains trapped as an interstitial between both graphene layers, leaving behind a vacancy in its original position [45]. Telling *et al.* [46] have analyzed the energetics of the intimate Frenkel pair, conformed by an interstital atom neighboring a vacancy, and they have concluded that the stacking where this defect is more stable is the SP stacking, for which the formation energy and excess energy barrier are 10.6 eV and 1.4 eV, respectively. From these data, we can deduce the thermal activation barrier for the Pristine $\rightarrow$ intimate Frenkel process: $\Delta E_{p\rightarrow if} = 12$ eV, and for the intimate Frenkel $\rightarrow$ Pristine process: $\Delta E_{if\rightarrow p} = 1.4$ eV. We calculate the cross section related with each process by using Eqs. 6.3, 6.4, 6.12, and 6.13, and from Eq. 6.11 we obtain an approximate value of the relative concentration between carbon atoms and intimate Frenkel

pairs in equilibrium:

$$\frac{[\mathrm{C}]_e}{[\mathrm{F}]_e} = \frac{\sigma_{if\to p}}{\sigma_{p\to if}} \approx \frac{34}{1}. \tag{6.19}$$

This last result indicates that approximately for each 34 carbon atoms, one intimate Frenkel pair should be in the sample. Consequently, this indicates that the population of this defect could be substantial enough to make it a good candidate for being the intermediate state for the vacancy formation process. It is rather counter-intuitive that such a difference in energy barriers (1.4 eV vs 12.0 eV) should give rise to that very large ratio of defects. It should be remembered though that these are not thermal processes but are related to the collision events, which transmit energies of several eV.

Our next step is to try to obtain a stable intimate Frenkel pair from an electron scattering event by AIMD below the expulsion threshold energy. Following the results obtained by Telling, *et al.* [46] we start our simulations from the SP stacking. We carry out the simulation for 17 different emission angles, and for each one we give seven different energies to the emitted atom within the range 16-22 eV. In all cases, the atom comes back to its original position and we never observe the stabilization of the intimate Frenkel pair.

The reason for the apparent contradiction between the kinetic estimation in Eq. 6.19 and the explicit calculation of expulsion lies in the fact that we are distributing an excitation energy in a single atom, while the necessary energy for the most optimum pathway is estimated using thermal barriers and is produced when this energy is distributed in a particular way to several atoms. The AIMD results indicate that the direct Frenkel pair formation caused by single electron-atom collision is unlikely from a pristine graphene sample.

Kinetics: multistep sputtering process

Inasmuch as we have not been able to stabilize the intimate Frenkel pair below the expulsion threshold energy from a pristine sample, we study other possible intermediate states that could facilitate the formation of the intimate Frenkel pair. A previous study [45] has shown that this defect has two possible pathways for annihilation: it can be converted into the pristine configuration or into a Stone-Wales defect. This suggests that the Stone-Wales defect could be an intermediate step during the creation of the

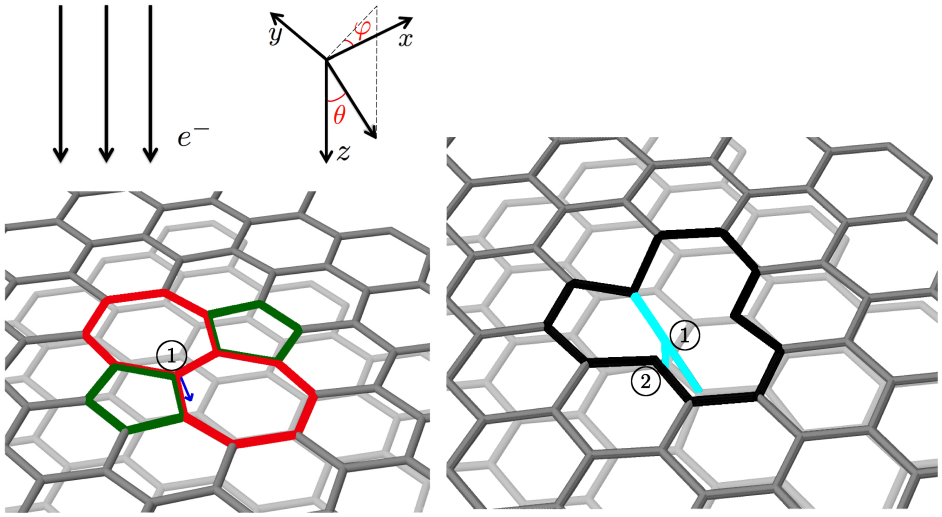

(a) (b)

Figure 6.7: (a) Initial state of the AIMD simulation with a Stone-Wales defect. It is made by two heptagonal (red) and two pentagonal (green) carbon rings. The blue arrow points in the direction ($\theta = 12°$, $\varphi = 1°$) of the initial velocity ($T = 17$ eV) which is given to the scattered atom (atom 1). (b) Final state of the same simulation in which the intimate Frenkel pair is stabilized. In the upper layer a vacancy is formed (black) and the scattered atom remains trapped between both layers (blue, atom 1) bridging the upper layer (dark) with the lower layer (light). The atom 2 is 'kicked' in the next simulation to obtain the intimate bi-Frenkel pair.

intimate Frenkel pair. The Stone-Wales defect is formed when a carbon-carbon bond is rotated 90° creating two pentagonal and two heptagonal carbon rings (Fig. 6.7). This defect has lower formation energy than the vacancy and it has been already obtained by AIMD simulations from a pristine graphene sample below the expulsion threshold energy [23]. It is expected to form (and annihilate) under the irradiation in our experiment.

We first obtain via AIMD expulsion simulations the expulsion threshold energy for a monolayer graphene sample that contains the Stone-Wales defect, in order to establish the energetic limit: $E_{thr}^{SW} = 18$ eV. Then, starting from a sample that contains one Stone-Wales defect we try to obtain the intimate Frenkel defect by AIMD simulations for lower energy values than this limit: after carrying out several simulations with different angles for the initial velocity and energies, we succeed in stabilizing the intimate Frenkel pair. Figure 6.7 shows the initial state of the simulation where the scattered atom is labeled (atom 1) and the final state in which the intimate Frenkel pair is stabilized. In this

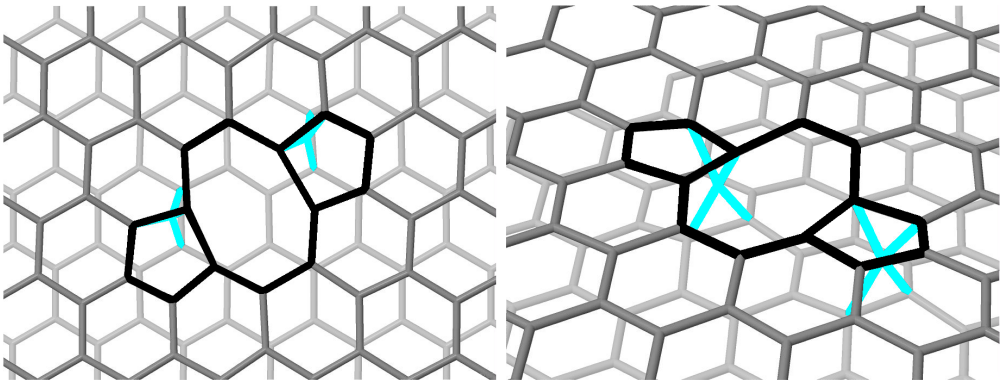

(a) (b)

Figure 6.8: Final relaxed configuration of an intimate bi-Frenkel pair. The initial state contains a unique intimate Frenkel pair (Fig. 6.6) and a certain velocity ($T = 15$ eV, $\theta = 20°$, $\varphi = 153°$) is given to the scattered atom. The V_2(5-8-5) divacancy (black) is formed in the upper layer while the two scattered atoms (blue) are bridging the upper layer (dark) with the lower layer (light). (a) and (b) correspond to different perspectives.

case, we use an energy of $T = 17$ eV and an azimuthal angle $\theta = 12°$ and a polar angle $\varphi = 1°$ for the initial velocity of the scattered atom.

Since vacancies or Frenkel pairs barely diffuse in the conditions of the experiment, and since the butterfly defect has two vacancies. we check the possibility of creating a second intimate Frenkel pair in the neighborhood of the previously formed one for lower energetic values than the expulsion threshold energy (E_{thr}^{SW}). For this purpose, we relax a bilayer graphene sample already containing an intimate Frenkel pair and we simulate a second collision event by giving a certain velocity to one of the atoms. We choose the atom labeled as 2 in Fig. 6.7(b) because it has a dangling bond, and therefore should be easier to expel from its original position. When this atom is 'kicked' with an energy of $T = 15$ eV, an azimuthal angle $\theta = 20°$ and a polar angle $\varphi = 153°$ for the initial velocity, two neighboring intimate Frenkel pairs are stabilized in the system and a V_2(5-8-5) divacancy is created in the upper layer. This defect, which we refer as the intimate bi-Frenkel defect, is formed by two spiro-interstitials (four-fold coordinated interstitial) neighboring a V_2(5-8-5) divacancy. Fig. 6.8 shows two different perspectives of the obtained intimate bi-Frenkel defect, where the V_2(5-8-5) divacancy is located in the upper layer formed by two pentagonal and one octagonal carbon rings. This divacancy is the one experimentally observed before the butterfly defect stabilizes (see Fig. 6.5). We obtain a formation energy of 15.54 eV for the obtained intimate bi-Frenkel pair.

By AIMD simulations we have demonstrated the possibility of creating divacan-

Table 6.4: Activation energies corresponding to each process: The first four values are thermal activation barriers while the last one has been obtained by our AIMD simulations.

Process	Activation energy (eV)
Pristine $\longrightarrow$ Stone-Wales (Ref. 7)	9
Stone-Wales $\longrightarrow$ Pristine (Ref. 7)	5.5
Stone-Wales $\longrightarrow$ I. Frenkel (Refs. 7 and 44)	8.5
I. Frenkel $\longrightarrow$ Pristine (Refs. 7 and 44)	1.4
I. Frenkel $\longrightarrow$ I. Bi-Frenkel	15

cies in bilayer graphene below the expulsion threshold energy by means of catalyzed intermediate states. To measure the frequency in which the formation of divacancies occurs following the suggested pathway, we propose the following chain of reactions:

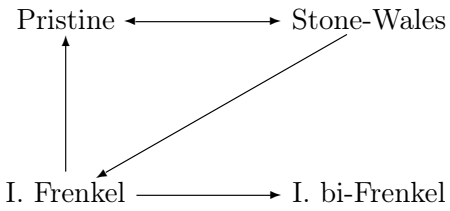

The intimate bi-Frenkel defect does not easily annihilate back into single vacancies because all the atoms have fully satisfied bonds. This is corroborated by the experiment, where, once a divacancy is created, it is completely stable. By using the activation energies shown in Table 6.4 for each possible reaction and the Eqs. 6.3, 6.4, 6.12, and 6.13 we calculate the cross section of each possible reaction. To do so, we solve the first order rate equations of this chain of reactions:

$$\frac{d[\mathrm{P}]}{dt} = -k_{\text{P-SW}}[\mathrm{P}] + k_{\text{SW-P}}[\mathrm{SW}] + k_{\text{IF-P}}[\mathrm{IF}], \tag{6.20}$$

$$\frac{d[\mathrm{SW}]}{dt} = -(k_{\text{SW-P}} + k_{\text{SW-IF}})[\mathrm{SW}] + k_{\text{P-SW}}[\mathrm{P}], \tag{6.21}$$

$$\frac{d[\mathrm{IF}]}{dt} = -(k_{\text{IF-P}} + k_{\text{IF-IBF}})[\mathrm{IF}] + k_{\text{SW-IF}}[\mathrm{SW}], \tag{6.22}$$

$$\frac{d[\mathrm{IBF}]}{dt} = k_{\text{IF-IBF}}[\mathrm{IF}], \tag{6.23}$$

where the concentration of each species (Pristine graphene, Stone-Wales, intimate Frenkel and intimate bi-Frenkel) is represented by its initials and each reaction is characterized by a rate constant k. The boundary condition for the initial concentration of each

species is: $[P]_0 = 38.46$ nm^{-2}, $[SW]_0 = [IF]_0 = [IBF]_0 = 0$. We obtain a theoretical estimation of 195 intimate bi-Frenkel defects that should have been formed in our sample or a corresponding value for the cross section of $\sigma = 75.2$ mb. This last value is overestimated comparing it with the obtained experimental one. The overestimation of the cross section was already expected by the use of thermal activation barriers and isotropic cross sections. The order of magnitude is, however, correct, showing that the proposed process is consistent with the experiments.

6.4 Conclusions

We have observed that the cross section for the formation of butterfly defects in bilayer graphene under electron radiation is substantially higher than in the case of monolayer graphene. Another difference with respect to the monolayer case is that there are no different types of defect in the sample, but only one type of divacancy: the butterfly defect, which stabilizes within the SP and AB stackings of the Moiré pattern becoming a very stable defect. Although its creation is facilitated by the presence of a second graphene layer, the filtering of the image shows that it is located in only one of the layers.

We find that the stability of the butterfly defect does not change significantly between monolayer and bilayer graphene, and the atomic displacements are small. These results are consistent with the weak interaction between two graphene layers and confirms that the mechanism for the formation process of the butterfly defect is different in the monolayer and bilayer graphene cases.

The results of the expulsion threshold energies for different atoms in bilayer graphene shows that the ones located in the lower layer (farther away from the beam source) have a similar kinetic behavior to the ones from monolayer graphene, hence the layer closer to the beam is the one that contains the divacancies.

We have demonstrated the possibility of creating divacancies in a bilayer graphene sample by AIMD simulations for electronic energies that are below the expulsion threshold energy. This is possible because new intermediate catalyzed states are created due to the presence of the second graphene layer. Although the estimated concentration of divacancies formed following the suggested chain of reaction is overestimated, the order of magnitude is correct with experimental results. Therefore, we demonstrate the

principal possibility of creating vacancies in a multilayer graphitic sample with lower electronic energies than the expulsion threshold, and accordingly, an increase of the displacement cross section of such systems with respect to the monolayer graphene case.

The reason why the divacancies stabilize within the SP and AB stackings of the Moiré pattern still remains unclear. However, as an initial proposal, we think that the fact that the interstitial atoms are stabilized in the SP stacking, [8, 45, 46] catalyze the formation of Stone-Wales defects, [47] and thus facilitate the proposed chain of reactions, could be related with the unresolved part of the observed phenomenon.

References

[1] Algara-Siller, G., Lehtinen, O., Wang, F., Nair, R., Kaiser, U., Wu, H., Geim, A., and Grigorieva, I. (2015) *Nature* **519(7544)**, 443–445.

[2] K.S. Novoselov, A. K. Geim, S. V. Morozov, D. Jiang, Y. Zhang, S. V. Dubonos, I. V. Grigorieva, and A. A. Firsov, *Science* **306**, 666 (2004).

[3] K.S. Novoselov, A. K. Geim, S. V. Morozov, D. Jiang, M. I. Katsnelson, I. V. Grigorieva, S. V. Dubonos, and A. A. Firsov, *Nature* (London) **438**, 197 (2005).

[4] C. Lee, X. Wei, J. W. Kysar, and J. Hone, *Science* **321**, 385 (2008).

[5] F. Banhart, J. Kotakoski, and A. Krasheninnikov, *ACS Nano* **5**, 26 (2011).

[6] A. H. Castro Neto, F. Guinea, N. M. R. Peres, K. S. Novoselov, and A. K. Geim, *Rev. Mod. Phys.* **81**, 109 (2009).

[7] A. Lherbier, Simon M.-M. Dubois, X. Declerck, S. Roche, Y. M. Niquet, and J. C. Charlier, *Phys. Rev. Lett* **106**, 046803 (2011).

[8] R. H. Telling and M. I. Heggie, *Philos. Mag.* **87**, 4797 (2007).

[9] A. Santana, A. Zobelli, J. Kotakoski, A. Chuvilin, and E. Bichoutkaia, *Phys. Rev. B* **87**, 094110 (2013).

[10] A. W. Robertson, C. S. Allen, Y. A. Wu, K. He, J. Olivier, J. Neethling, A. I. Kirkland, and J. H. Warner, *Nat. Commun.* **3**, 1144 (2012).

[11] J. J. Palacios, and F. Ynduráin, *Phys. Rev. B* **85**, 245443 (2012).

[12] A. A. El-Barbary, R. H. Telling, C. P. Ewels, M. I. Heggie, and P. R. Briddon, *Phys. Rev. B* **68**, 144107 (2003).

[13] M. M. Ugeda, I. Brihuega, F. Hiebel, P. Mallet, J. Y. Veuillen, J. M. Gomez-Rodriguez, and F. Yndurain, *Phys. Rev. B* **85**, 121402 (2012).

[14] C. D. Latham, M. I. Heggie, J. A. Gámez, I. Suárez-Martínez, C. P. Ewels, and P. R. Briddon, *J. Phys.: Condens. Matter* **20**, 395220 (2008).

[15] A. Gulans, A. V. Krasheninnikov, M. J. Puska, and R. M. Nieminen, *Phys. Rev. B* **84**, 024114 (2011).

[16] A. Hashimoto, K. Suenaga, A. Gloter, K. Urita, and S Iijima, *Nature* (London) **430**, 870 (2004).

[17] M. H. Gass, U. Bangert, A. L. Bleloch, P. Wang, R. R. Nair, and A. K. Geim, *Nature Nanotechnol.* **3**, 676 (2008).

[18] J. C. Meyer, C. Kisielowski, R. Erni, M. D. Rossell, M. F. Crommie, and A. Zettl, *Nano Lett.* **8**, 3582 (2008).

[19] K. Urita, K. Suenaga, T. Sugai, H. Shinohara, and S. Iijima, *Phys. Rev. Lett.* **94**, 155502 (2005).

[20] A. Chuvilin, J. C. Meyer, G. Algara-Siller, and U. Kaiser, *New J. Phys.* **11**, 083019 (2009).

[21] C. Gomez-Navarro, J. C. Meyer, R. S. Sundaram, A. Chuvilin, S. Kurasch, M. Burghard, K. Kern, and U. Kaiser, *Nano Lett.* **10**, 1144 (2010).

[22] Z. G. Wang, Y. G. Zhou, J. Bang, M. P. Prange, S. B. Zhang, and F. Gao, *J. Phys. Chem. C* **116**, 16070 (2012).

[23] J. Kotakoski, J. C. Meyer, S. Kurasch, D. Santos-Cottin, U. Kaiser, and A. V. Krasheninnikov, *Phys. Rev. B* **83**, 245420 (2011).

[24] O. V. Yazyev, I. Tavernelli, U. Rothlisberger, and L. Helm, *Phys. Rev. B* **75**, 115418 (2007).

[25] Y. Kim, J. Ihm, E. Yoon, and G. D. Lee, *Phys. Rev. B* **84**, 075445 (2011).

[26] J. C. Meyer, F. Eder, S. Kurasch, V. Skakalova, J. Ko- takoski, H. J. Park, S. Roth, A. Chuvilin, S. Eyhusen, G. Benner, A. V. Krasheninnikov, and U. Kaiser, *Phys. Rev. Lett.* **108**, 196102 (2012).

[27] A. Zobelli, A. Gloter, C. P. Ewels, G. Seifert, and C. Colliex, *Phys. Rev. B* **75**, 245402 (2007).

[28] W. A. McKinley and H. Feshbach, *Phys. Rev.* **74**, 1759 (1948).

[29] A. Chuvilin and U. Kaiser, *Ultramicroscopy* **104**, 73 (2005).

[30] J. M. Soler, E. Artacho, J. D. Gale, A. García, J. Junquera, P. Ordejón, and D. Sánchez-Portal, *J. Phys.: Condens. Matter* **14**, 2745 (2002).

[31] D.R. Hamann, M. Schluter, and C. Chiang, *Phys. Rev. Lett.* **43**, 1494 (1979).

[32] M. Dion, H. Rydberg, E. Schröder, D. C. Langreth, and B. I. Lundqvist, *Phys. Rev. Lett.* **92**, 246401 (2004).

[33] http://icmab.cat/leem/siesta/

[34] M. R. Hestenes and E. Stiefel, *J. Res. Nat. Bur. Stand.* **49**, 409 (1952).

[35] S. Shallcross, S. Sharma, E. Kandelaki, and O. A. Pankratov, *Phys. Rev. B* **81**, 165105 (2010).

[36] H. J. Monkhorst and J. D. Pack, *Phys. Rev. B* **13**, 5188 (1976).

[37] M. Birowska, K. Milowska, and J. A. Majewski, *Acta Phys. Pol. A* **120**, 845 (2011).

[38] Y. X. Zhao and I. L. Spain, *Phys. Rev. B* **40**, 993 (1989).

[39] L. Verlet, *Phys. Rev.* **159**, 98 (1967).

[40] J. Zubeltzu, A. Chuvilin, F. Corsetti, A. Zurutuza, and E. Artacho, *Phys. Rev. B* **88**, 245407 (2013).

[41] R. Matzdorf, G. Soff, and G. Mehler, *Z. Phys. D* **6**, 5 (1987).

[42] S. T. Skowron, V. O. Koroteev, M. Baldoni, S. Lopatin, A. Zurutuza, A. Chuvilin, and E. Besley, *Carbon* **105**, 176-182 (2016).

[43] J. Kotakoski, C. H. Jin, O. Lehtinen, K. Suenaga, and A. V. Krasheninnikov, *Phys. Rev. B* **82**, 113404 (2010).

[44] V.K. Tewary and B. Yang, *Phys. Rev. B* **79**, 125416 (2009).

[45] C. P. Ewels, R. H. Telling, A. A. El-Barbary, M. I. Heggie, and P. R. Briddon, *Phys. Rev. Lett.* **91**, 025505 (2003).

[46] R. H. Telling, C. P. Ewels, A. A. El-Barbary, and M. I. Heggie, *Nature Mater.* **2**, 333 (2003).

[47] C. P. Ewels, M. I. Heggie, and P. R. Briddon, *Chem. Phys. Lett.* **351**, 178 (2002).

Chapter 7

Conclusions and further work

In this thesis we study the properties of two-dimensionally confined water by means of computational simulations based on both, *ab initio* and classical molecular dynamics calculations. We first study the intrinsic properties exhibited by bilayer water under the confinement of a Lennard-Jones 9-3 planar potential at different temperatures and densities. We then study the extrinsic effects produced by a controlled periodic modulation of the confining potential on bilayer water.

Under a planar confinement, a bilayer liquid and three crystalline regions are found to be stable in the density-temperature phase diagram. The characterization of the crystalline phases shows that two of them, the honeycomb ice and square-tubes ices have the oxygen and hydrogen atoms fixed. However, at high densities and temperatures, we observe the stabilization of a crystalline ice with the oxygens arranged into a triangular lattice, but the hydrogens remaining delocalized. The estimation of the configurational entropy coming from the hydrogen disorder gives twice the residual entropy of common ice, in agreement with a previous study based on the random structure search method. We observe two types of melting at high densities: a first order phase transition into the square-tubes ice at low temperatures, and a continuous phase transition into the triangular ice at higher T. For the latter the observed phenomenology strongly suggests Kosterlitz-Thouless-Halperin-Nelson-Young two dimensional melting, including the observation of an intermediate hexatic phase between the solid and the liquid. During this continuous melting only the oxygens are affected, while the hydrogens keep behaving liquid-like, resulting in a unusual decoupling in the dynamics of each species.

The characterization of the liquid shows that the triangular local structure is maintained, and the two layers are strongly correlated with very infrequent exchange of matter. We observe that the decoupling between the dynamics of O and H already starts in the liquid phase, showing the existence of a regime in the phase diagram constituted by the triangular, hexatic, and liquid phases, in which water resembles a simple monoatomic fluid.

The unusual characteristics of the system in this regime allows us to expect that the dielectric properties of bilayer water differ markedly from the ones observed for its bulk counterpart. A preliminary estimation of the relative dielectric constant ϵ_r along the planar direction of the triangular ice shows that its value is slightly larger than 200, substantially higher than the 53 obtained at room pressure and $T = 273$ K for Ih ice using the TIP4P/2005 model. Due to the large constraints along the confining direction, the out-of-plane component of ϵ_r is expected to be very low: for the liquid at $\rho = 1.17$ g cm^{-3} and $T = 300$ K, we have obtained a value of $\epsilon_r = 3.1$. Moreover, we estimate the Debye relaxation time of triangular ice to be clearly below the nanosecond scale, close to the relaxation time observed for bulk water (17 ps) and far from the one observed for Ih ice (2.2 μs) at room conditions. A more detailed dielectric characterization of bilayer water and ice seems to be a promising topic for further work.

We then simulate two-dimensionally confined water between two corrugated walls. We propose a periodic confining potential based on the Lennard-Jones particles that plays the role of a confining substrate and allows to control the lattice type, lattice parameter and amplitude of the corrugation at the interface. We analyze the structural and dynamical properties of water under different modulation amplitudes α and lattice parameters a.

We choose a triangular lattice parameter $a = 4.78$ Å ideal for the stabilization of a layer of honeycomb ice. As expected, at low-mid densities, the honeycomb ice rapidly stabilizes within the phase diagram as the modulation amplitude increases. However, before the liquid freezes its triangular structure disfavoured by the external modulation does not almost change independently of its density. At high densities and low temperatures, the square tubes ice keeps being stable for $\alpha \leq 0.6$. The analysis of the stability of the hexatic phase under different amplitudes of the modulation indicates that at $\alpha = 0.6$ the frustration is large enough for it to be no longer stable. We therefore conclude that the KTHNY continuous melting occurs for $\alpha \leq 0.4$. When $\alpha \geq 0.8$, a new solid phase appears: the intercalated honeycomb ice. This solid is made of two

external honeycomb layers and a third middle layer where the molecules are located into the centre of the honeycomb hexagons. The comparison between the AIMD and the MD liquid shows that both methods have a large agreement. The AIMD liquid tends to be more triangular-like structured, as previously reported. The imposed modulation disfavours triangular-like structures, and therefore, affects more substantially the AIMD liquid, which losses the AA stacking and well-defined layering shown in the planar confinement.

For more realistic lattice parameters (a = 2.5, 2.75, and 3.0 Å) we do not observe significant changes on the phase behavior staying liquid at low-mid densities, and triangular with similar features to the hexatic phase at high densities. Although the xy averaged positions of the oxygens and DDFs show that the molecules from the liquid displays a significant anisotropy, there is hardly noticeably change in the structural (RDF) and dynamical (diffusivity) behavior.

Although all the indicators employed in this thesis indicate the existence of an intermediate hexatic phase where the continuous phase transition has been observed, it would be interesting to calculate the $g_6(r)$ orientational correlation function (see *Phase transitions in two-dimensional colloidal systems* by H. H. von Grünberg, P. Keim, and G. Maret) to prove that it is hexatic. $g_6(r)$ is constant, shows an algebraic decay, or decays exponentially depending if the phase is solid, hexatic or liquid respectively. The size of the simulation cells employed in this thesis were too small to check the type of decay that $g_6(r)$ shows.

It would be very interesting to estimate the free-energy of confinement in the systems studied, in order to study the stability of water under such a strong confinement and how the free-energy changes with the introduction of the modulation. By calculating the internal energy of the system, and with the estimation of the free-energy, it would be possible to estimate the entropic contribution. We started with simple estimations based on the calculations of the parallel and perpendicular pressures, but it showed to be flawed here. Instead, thermodynamic integration techniques could be used, which would introduce the confinement in a gradual manner for instance.

With the proposed modulated confining potential, it would be interesting to study confined water under different values of the hydrophilicity (ϵ) and lattice types, such as different periodic lattices or amorphous interfaces. Thereby, a larger range of possible interface types would be covered. It would be possible to estimate how the free-energy

of the liquid changes with these parameters, and therefore, check how the stability of the liquid and vapour phases changes under these conditions.

The majority of the calculations are carried out by MD calculations employing the TIP4P/2005 force-field. Some points of the phase diagram where liquid water was found are also calculated by AIMD calculations with the vdW-DF$^{\mathrm{PBE}}$ functional. The comparison between the results obtained in this thesis shows the surprisingly large agreement between these two calculations methods, and supports their validity to describe water.

List of publications

This thesis is based on the following list of publications:

1. *Knock-on damage in bilayer graphene: indications for a catalytic pathway*
   Jon Zubeltzu, Andrey Chuvilin, Fabiano Corsetti, Amaia Zurutuza, and Emilio Artacho, *Phys. Rev. B* **88**, 245407 (2013).
   (Chapter 6)

2. *Enchanced configurational entropy in high-density nanoconfined bilayer ice*
   Fabiano Corsetti, **Jon Zubeltzu**, and Emilio Artacho, *Phys. Rev. Lett.* **116**, 085901 (2016).
   (Chapter 3)

3. *Continuous melting throw a hexatic phase in confined bilayer water*
   Jon Zubeltzu, Fabiano Corsetti, and Emilio Artacho, *Phys. Rev. E,* **93**, 062137 (2016).
   (Chapter 3 and 4)

4. *Simulations of water nano-confined between corrugated planes*
   Jon Zubeltzu, and Emilio Artacho, submitted to *J. Chem. Phys.*, *arXiv:1705.05270.*
   (Chapter 5)

Acknowledgements

First of all, I would like to start acknowledging the people from Nanogune, it has been a great pleasure to spend 5 years in such a nice working atmosphere.

A José y Marivi, gracias por el tiempo dedicado y estar siempre dispuestos a ayudar, vuestras ideas han sido muy buenas y me han sido muy útiles durante la tesis. I want to thank Andrey, not only for the collaboration we carried out, but also for being a great motivator in my scientific activity.

To the past and present members of the Theory group for always having a helpful attitude, I believe our group has always had a great atmosphere. Special mention deserves my PhD paki-partner Rafi, source of gossips, philosophical discussions and laughs. Pablo Aguado por siempre estar dispuesto ayudar y ser un gran compañero de trabajo y de risas.

Oihanari eskerrak, tesi honen zati handi bat bere laguntzarekin egin da.

Eskerrik asko kuadrillari, txorradak esatetik eta ondo pasatzetik aparte, momentu guztitan euskarri izateagatik, grandes.

To the new incorporations, not only for correcting the english of this thesis, but specially for being great friends in this last year: Eva, Jakob, Elham, Ali, Josu y Juanma. Se merece una mención especial mi hermano francés Etienne, clave en la última etapa de esta tesis. Siempre un placer jugar al ping-pong.

A las viejas glorias de Nanogune: Pablu, Cesar, Paulinho, Iban y Santi, compañeros en malos momentos pero sobre todo de risas, muchas risas. Habeis hecho que estos años en Nanogune hayan sido increibles.

Nire eserleku parean agertutako neska politari, tesi hau beranduago bukatzearen eta nire goizeroko irrifarraren erruduna, emandako bizipozagatik.

Hurbileko familiari, baina batez ere, Haritz, Beñat, Mikel eta Martini, behar izan dudanean hor egoteagatik. Aita eta amari, nigan konfiantza itsua eukitzeagatik eta beti nere alde egiteagatik.

I have left the last acknowledgments for the two most important persons. Fabiano Corsetti, partner, technician and my second non-official supervisor, who had the patience for teaching me all the basics (for years). Thanks for being such a great teacher and motivator, but specially for the laughs, philosophical discussions and friendship.

Por ultimo, la persona más clave en esta tesis, Emilio, no sé como he tenido tanta suerte. Un modelo como científico y como persona. Gracias por todo lo aprendido, la confianza dada y el apoyo. Algo inolvidable de estos años es haber trabajado contigo, no podría haber tenido un mejor supervisor.